



**Taking Nanotechnological Remediation Processes  
from Lab Scale to End User Applications  
for the Restoration of a Clean Environment**

Project Nr.: 309517

EU, 7th FP, NMP.2012.1.2

**WP4: Mobility and Fate of Nanoparticles**

**DL 4.2: Stability, Mobility, Delivery and Fate of  
optimized NPs under Field Relevant Conditions**

Vesna Micić Batka, Thilo Hofmann (UNIVIE)

31 October 2016




[Downloaded from www.nanorem.eu/toolbox](http://www.nanorem.eu/toolbox)

The research leading to these results has received funding from the European Union Seventh Framework Programme (FP7/2007-2013) under Grant Agreement n° 309517

**List of co-authors:**

Name, First Name	Partner Organisation	
Micić Batka, Vesna Schmid, Doris Velimirović, Milica Hofmann, Thilo	University of Vienna	
Mackenzie, Katrin Georgi, Anett Bleyl, Steffen	Helmholtz Centre for Environmental Research -UFZ	
Auffan, Mélanie	Centre National de la Recherche Scientifique - CNRS - CEREGE	
Braun, Jürgen Klaas, Norbert Herrmann, Christine Wiener, Anke Miyajima, Kumiko	University of Stuttgart, VEGAS	
Lloyd, Jonathan Joshi, Nimisha	University of Manchester	
Crampon, Marc Hellal, Jennifer Ollivier, Patrick Mouvet, Christophe	The French Geological Survey	
Meckenstock, Rainer Krok, Beate-Agnes	Universität Duisburg-Essen	
Filip, Jan Zboril, Radek	Palacky University Olomouc	
Oughton, Deborah Lebed, Pablo	Norwegian University of Life Sciences	

**Reviewed by PAG member:**

Name, First Name	Organisation	
Elliott, Daniel W.	Geosyntec Consultants	

**Reviewed and agreed by PMG**

## Table of Contents

<b>List of Figures</b> .....	<b>iv</b>
<b>List of Tables</b> .....	<b>viii</b>
<b>Glossary</b> .....	<b>1</b>
<b>1 Introduction to DL 4.2</b> .....	<b>3</b>
1.1 <i>Stability of NP suspensions</i> .....	3
1.2 <i>Delivery and Mobility of NPs</i> .....	3
1.3 <i>Fate of NPs</i> .....	4
1.4 <i>Optimization of NPs</i> .....	4
<b>2 Optimized Nanoparticles</b> .....	<b>5</b>
<b>3 Objectives of DL 4.2</b> .....	<b>5</b>
<b>4 Results on stability, mobility, delivery and fate of optimized NPs under field relevant conditions</b> .....	<b>6</b>
4.1 <i>NANOFER 25S (NANO IRON s.r.o.)</i> .....	6
4.1.1 <i>Stability of NANOFER 25S</i> .....	6
4.1.2 <i>Mobility and Delivery of NANOFER 25S</i> .....	7
4.1.3 <i>Fate of Nanofer NANOFER 25S under field relevant conditions</i> .....	11
4.2 <i>NANOFER STAR (NANO IRON s.r.o.)</i> .....	15
4.2.1 <i>Stability of NANOFER STAR</i> .....	15
4.2.2 <i>Mobility and Delivery of NANOFER STAR</i> .....	18
4.2.3 <i>Fate of NANOFER STAR under field relevant conditions</i> .....	22
4.3 <i>Radiolabelled NANOFER STAR</i> .....	25
4.3.1 <i>Mobility of radiolabelled NANOFER STAR</i> .....	25
4.4 <i>Milled ZVI (FerMEG12, UVR-FIA GmbH)</i> .....	27
4.4.1 <i>Stability of milled ZVI (FerMEG12) suspension</i> .....	27
4.4.2 <i>Mobility of milled ZVI (FerMEG12)</i> .....	28
4.4.3 <i>Fate of milled ZVI (FerMEG12) under field relevant conditions</i> .....	31
4.5 <i>Carbo-Iron® (SciDre GmbH, UFZ Leipzig)</i> .....	36
4.5.1 <i>Stability of Carbo-Iron® suspension</i> .....	36
4.5.2 <i>Mobility and Delivery of Carbo-Iron</i> .....	38
4.5.3 <i>Fate of Carbo-Iron® under field relevant conditions</i> .....	43
4.6 <i>Trap-Ox Fe-zeolites</i> .....	48
4.6.1 <i>Stability of Trap-Ox Fe-zeolites</i> .....	49
4.6.2 <i>Mobility and Delivery of Trap-Ox Fe-zeolites</i> .....	50
4.6.3 <i>Fate of Trap-Ox Fe-BEA35 under field relevant conditions</i> .....	52
4.7 <i>Bionanomagnetite (University of Manchester)</i> .....	55
4.7.1 <i>Stability of bionanomagnetite</i> .....	55
4.7.2 <i>Mobility and delivery of bionanomagnetite</i> .....	57
4.7.3 <i>Fate of bionanomagnetite and palladized bionanomagnetite under field relevant conditions</i> .....	60
4.8 <i>Nano-Goethite (University of Duisburg-Essen)</i> .....	64
4.8.1 <i>Stability of Nano-Goethite</i> .....	64
4.8.2 <i>Mobility and Delivery of Nano-Goethite</i> .....	64
4.8.3 <i>Fate of Nano-Goethite under field relevant conditions</i> .....	67
4.9 <i>Mg/Al particles (VEGAS, University of Stuttgart)</i> .....	73
4.9.1 <i>Fate of Mg/Al particles under field relevant conditions</i> .....	73
<b>5 List of References</b> .....	<b>75</b>
<b>6 Appendix</b> .....	<b>77</b>

## List of Figures

<b>Figure 1:</b>	An example of agar agar-stabilized milled ZVI suspension at the beginning of the stability test (left), after 24 h (middle) and after 48 h (right). $c_{\text{agar agar}} = 1 \text{ g/L}$ ; $c_{\text{particle}} = 1 \text{ g/L}$ . Sedimentation rate ca. 0.1 m/d. Photo: Doris Schmid, UNIVIE. ....	3
<b>Figure 2:</b>	Factors influencing fate of NPs. ....	4
<b>Figure 3:</b>	Transport distance ( $\Delta x$ ) of optimized NANOFER 25S particles in suspensions with 10 g/L Fe(0) as a function of the CMC concentration. ....	8
<b>Figure 4:</b>	Mean breakthrough curves for NANOFER 25S (measured as $\text{Fe}_{\text{tot}}$ ) and the corresponding standard deviation before and after the injection of 10 mg/L solution of Na humate in M.I (A), M.II (B), PM from Spolchemie I field site, CZ (C) and PM from Solvay field site, CH (D); n is number of replicates; Injection velocity: 100 m/d; initial particle concentration: 1 g/L. ....	9
<b>Figure 5:</b>	PCE concentration profile over reaction time in effluents of a column reactor (with NANOFER 25S particles, green line) and of a blank column (black line). ....	12
<b>Figure 6:</b>	Cumulative curves showing $\text{Cl}^-$ formation (left) and magnetic susceptibility measurements used to trace changes in Fe(0) concentration along the column (right). ....	12
<b>Figure 7:</b>	An example of Mössbauer spectra of NANOFER 25S aged in groundwater from Spolchemie I, CZ field site. Gray: Fe(0); red: $\text{Fe}^{3+}$ , blue: $\text{Fe}^{2+}$ , orange: superparamagnetic ferric oxides/oxyhydroxides. Aging time: 8 days. ....	14
<b>Figure 8:</b>	Evolution of the size (number and intensity mean) for PAA-stabilized NANOFER STAR suspension ( $c_{\text{particle}} = 10 \text{ mg/L}$ ) as a function of pH. Grey areas correspond to the pH range where the particles are neutrally charged. ....	17
<b>Figure 9:</b>	Average hydrodynamic diameter (left) and zeta potential (right) of PAA- NANOFER STAR suspensions prepared in different standardized water F.I.s., F.I.m, and F.I.h, measured in a 10 mg/L particle suspension at 25 °C. For comparison, data for ultrapure water (MILIQ) are also plotted. ....	17
<b>Figure 10:</b>	Duplicate experimental breakthrough curves (depicted as hollow and full cycles) for PAA-stabilized NANOFER STAR suspension (measured as $\text{Fe}_{\text{tot}}$ ) in porous media M.I (a) and M.II (b). $C_{0, \text{particle}} = 1 \text{ g/L}$ ; $v_{\text{eff}} = 100 \text{ m/d}$ . Solid curves are mean values of the model generated by CXTFIT, STANMOD software, version 2.08.1130 by fitting the convection-dispersion equation to the experimental breakthrough curve. $n_e$ is effective porosity. ....	19
<b>Figure 11:</b>	Breakthrough curves of modified NANOFER STAR. For comparison, the data for NanoRem standard NP, NANOFER 25S (N25S) are also plotted. ( $C_{0, \text{particle}} = 10 \text{ g/L}$ as Fe(0); $v_{\text{eff}} = 100 \text{ m/d}$ ). ....	20
<b>Figure 12:</b>	Delta frequency along the column length for activated NANOFER STAR and CMC-modified NANOFER STAR ca. 2 h from the beginning of the injection into a commercial quartz sand. $v_{\text{eff}} = 100 \text{ m/d}$ . For comparison, data frequency for inactivated NANOFER STAR is also included. ....	21
<b>Figure 13:</b>	Delta frequency as a proxy for particle content along the column length during the course of the activated NANOFER STAR injection into M.II porous medium at low (10 m/d) flow velocity (left) and high (300 m/d) flow velocity (right). ....	21
<b>Figure 14:</b>	Formation of ethene, ethane and ethyne in the course of PCE degradation (left) and proportion of degraded PCE with inactivated NANOFER STAR (blue line), activated NANOFER STAR at room temperature (red line) and activated NANOFER STAR in a refrigerator (green line) (right). ....	23
<b>Figure 15:</b>	Mössbauer spectra of inactivated (left) and (for 48 h) activated NANOFER STAR. ....	23

<b>Figure 16:</b> XRD pattern of activated NANOFER STAR after being in contact with anoxic groundwater from Spolchemie I, CZ field site for one month. GR = green rust. ....	24
<b>Figure 17:</b> Changes over time in content of $\alpha$ -Fe, $\text{Fe}_3\text{O}_4$ and green rust (GR) (as determined by XRD) in a groundwater sample from Spolchemie I, CZ field site (well PV130), where activated NANOFER STAR was injected. ....	25
<b>Figure 18:</b> Gamma activity distribution in counts per minute (cpm) along the column length. Insert: Segment of the exanimated column. ....	26
<b>Figure 19:</b> SEM image of milled ZVI particles. Source: UVR-FIA GmbH. ....	27
<b>Figure 20:</b> Viscosity as a function of shear rate for water and 1 g/L of agar agar solution. ....	28
<b>Figure 21:</b> Duplicate breakthrough curves (hollow and full cycles) for agar agar-stabilized milled ZVI ( $c_{0, \text{particles}}$ : ca. 1 g/L in 1 g/L agar agar; $v_{\text{eff}} = a$ . 100 m/d). Solid line depicts the breakthrough of a $\text{Br}^-$ tracer. ....	30
<b>Figure 22:</b> XRD patterns of the milled ZVI at the beginning of experiment (red), as well as after 7 and 105 days of contact with PM from the Solvay, CH and Balassagyarmat, HU field site. ....	34
<b>Figure 23:</b> Changes in Fe(0) concentration (measured by means of magnetic susceptibility) along the column during the experiment. ....	35
<b>Figure 24:</b> Bright field TEM image of Carbo-Iron <sup>®</sup> . ....	36
<b>Figure 25:</b> Sedimentation profile of Carbo-Iron <sup>®</sup> suspensions measured at 1 and 4 cm below the water table. A: $c_{\text{CMC}} = c_{\text{particle}} \times 0.2$ , B: $c_{\text{CMC}} = c_{\text{particle}} \times 0.05$ . ....	37
<b>Figure 26:</b> Sedimentation profile of Carbo-Iron <sup>®</sup> suspensions containing A: 30 g/L of particles and varying CMC content and B: varying particle and CMC content with $c_{\text{CMC}} = c_{\text{particle}} \times 0.2$ . Aliquots sampled 1 cm below the water table. ....	37
<b>Figure 27:</b> Breakthrough curves for CMC-stabilized Carbo-Iron <sup>®</sup> prepared in different types of standard water (D.I column filled with M.I, $c_{0, \text{particle}} = 5.7 \text{ g/L}$ , $c_{\text{Fe(0) in particles}} = 1.1 \text{ g/L}$ , $c_{\text{CMC}} = 1.1 \text{ g/L}$ , $v_{\text{eff}} = 10 \text{ m/d}$ , $n_{e \text{ (M.I)}} = 0.33$ ). ....	39
<b>Figure 28:</b> Breakthrough curves for CMC-stabilized Carbo-Iron <sup>®</sup> suspension in F.I.m with various particle-to-CMC ratio (D.I column filled with M.I, $v_{\text{eff}} = 10 \text{ m/d}$ , $n_{e \text{ (M.I)}} = 0.33$ ); $c_{\text{Fe(0) in particles}} = 19.9 \text{ wt\%}$ ). Note that "CIC" in this figure legend refers to Carbo-Iron <sup>®</sup> particles. ....	39
<b>Figure 29:</b> Glass columns filled with porous medium from the Balassagyarmat field site, HU, showing an inhomogeneous distribution of Carbo-Iron <sup>®</sup> during and after the injection of the particle suspension. ....	41
<b>Figure 30:</b> Breakthrough of Carbo-Iron <sup>®</sup> in porous medium and groundwater from the Balassagyarmat field site, HU ( $c_{\text{particle}} = 15 \text{ g/L}$ , $c_{\text{CMC}} = 1.5 \text{ g/L}$ , D.II column, $n_e = 0.26$ , $v_{\text{eff}} = 10 \text{ m/d}$ ). ....	41
<b>Figure 31:</b> Spatial distribution of Carbo-Iron <sup>®</sup> in the sediment as function of the distance from the injection port. $c_{\text{particle}} = 20 \text{ g/L}$ ; $c_{\text{CMC}} = 1 \text{ g/L}$ ; porous media: M.II; 3 intermittent injection cycles; $v_{\text{eff}} = 52 \text{ m/d}$ , subsequent resting time ca. 24 h at groundwater flow at $v_{\text{eff}} = 0.25 \text{ m/d}$ . ....	43
<b>Figure 32:</b> Powder XRD spectrum of fresh Carbo-Iron <sup>®</sup> (a) and Carbo-Iron <sup>®</sup> aged in F.I.m for 27 days at 25 °C (b). ....	44
<b>Figure 33:</b> Concentrations of $\text{Cl}^-$ at the outlet of the column reactor (M.II, $n_e = 0.26$ , $v_{\text{eff}} = 4.5 \text{ m/d}$ , length of reactive zone: 14 cm, $m_{\text{PCE}} = 162 \text{ mg}$ ). PV = pore volume. ....	46
<b>Figure 34:</b> Concentrations of chlorinated hydrocarbons (PCE, TCE and <i>cis</i> -1,2-DCE) in the column effluents (M.II, $n_e = 0.26$ , $v_{\text{eff}} = 4.5 \text{ m/d}$ , length of reactive zone: 14 cm, $c_{\text{PCE}} = 162 \text{ mg}$ ); PV = pore volume. ....	47
<b>Figure 35:</b> Cumulative amount of PCE in column effluents in column reactor containing the reactive zone with Carbo-Iron <sup>®</sup> (red line) and in control column reactor (without Carbo-Iron <sup>®</sup> , blue line). Note that CIC refers to Carbo-Iron <sup>®</sup> particles. ....	47

- Figure 36:** Scanning electron microscope (SEM) images of Trap-Ox Fe-BEA35 (left) and Trap-Ox Fe-MFI120 (right).....48
- Figure 37:** Stability of particle suspensions for Trap-Ox Fe-BEA35 (A) and Trap-Ox Fe-MFI120 (B) at pH 5.5 (dashed line) and 8.3 (solid line) and for Trap-Ox Fe-BEA35 in F.I.h (C) (dashed line in C indicates interpolation). .....49
- Figure 38:** Breakthrough curves for MTBE over exchanged pore volume (PV) during individual adsorption cycles (left) and retardation factors for MTBE within the 4 adsorption cycles over total exchanged PV (right). Initial particle loading onto M.I: 1.1 wt%.  $c_{\text{MTBE}} = 10 \text{ mg/L}$ ,  $v_{\text{eff}} = 1 \text{ m/d}$  (in adsorption steps),  $c_{\text{H}_2\text{O}_2} = 10 \text{ g/L}$ ,  $v_{\text{eff}} = 1 \text{ m/d}$ ). .....54
- Figure 39:** Normalized concentration of bionanomagnetite in the upper 1 cm of the modified suspension over time.  $c_0$  is the initial particle concentration.  $c$  is the particle concentration after a defined time. Control stands for pure aqueous Bnm. Agar stands for agar agar-modified suspension, humic salt (sodium) stands for Na-humate-stabilized suspensions. ....56
- Figure 40:** Mean breakthrough curves of stabilized bionanomagnetite suspensions with agar agar, guar gum and starch (left) and Na humate (right) in D.I columns. Injection velocity: 100 m/d;  $c_0$ ,  $\text{Fe}_{\text{tot}} = 1 \text{ g/L}$ . Solid line is the breakthrough of KBr tracer. Control stands for Bnm in unmodified aqueous suspension. Note that guar stands for guar gum, agar stands for agar agar and humic stands for Na humate. ....58
- Figure 41:** Sample of M.II collected from the column inlet (left) and column outlet (right), indicating bionanomagnetite accumulation (dark colour, left) around the column inlet and its absence at the column outlet (original colour of M.II, right). .....60
- Figure 42:** Reduction of Cr (VI) by bionanomagnetite in differently stabilized suspensions and in control (A). Changes in Cr (VI) concentrations normalized to initial  $\text{Cr}_{\text{tot}}$  in the course of the reaction (B). “Guar” stands for guar gum-, “starch” for starch- and “humic” for Na humate-stabilized suspensions. Control refers to the aqueous particle suspension without modifiers. ....61
- Figure 43:** Cr(VI) removal by pristine palladized bionanomagnetite, i.e. control and palladized bionanomagnetite stabilized with guar gum (3 g/L) or starch (2 g/L); Initial  $\text{Fe}_{\text{tot}} = 0.5 \text{ g/L}$ . ....62
- Figure 44:** Decrease of PCE concentration in the synthetic groundwater treated with 1 g/L Fe bionanomagnetite (BnM, blue circles) and the 0.025 g/L palladized bionanomagnetite (Pd-BnM, red squares) the latter supplied with an excess of  $\text{H}_2$ (A) and linear regression of  $\ln[\text{PCE}]$  used to calculate dechlorination kinetics ( $k_{\text{obs}}$ ) (B). .....63
- Figure 45:** Mobility of Nano-Goethite (estimated from  $\text{Fe}_{\text{tot}}$  content) as a function of theoretical distance from the injection well ( $r$ ). .....66
- Figure 46:** Fe(II) formation during the bioremediation of toluene and benzoate in sets of batch reactors. Detailed information on experimental sets denoted in the legend is given in Table 25. ....69
- Figure 47:** Increase of Fe(II) content (left) and degradation of benzoate (right) in the column reactor after the first bioremediation step. NP1 and NP2 refer to columns with Nano-Goethite, while BL1 and BL2 refer to blanks (without Nano-Goethite).....70
- Figure 48:** Increase of Fe(II) content (left) and slow degradation of benzoate (right) in the column reactor after the second bioremediation step. NP1 and NP2 refer to columns with Nano-Goethite, while BL1 and BL2 refer to blanks (without Nano-Goethite). ....70
- Figure 49:** SEM images of fresh Nano-Goethite (upper image) and 360 days aged Nano-Goethite from the column effluent (lower image), also in higher magnification (lower image right).....71
- Figure 50:** EDX spectra and SEM images (indicating the positions selected for EDX analysis) for fresh Nano-Goethite (upper images) and 360 days aged Nano-Goethite. SEM images at the left-hand side

were recorded at 20 kV, while those at the right-hand side at 2 kV (providing better visualization of the topographic features). Black, dark grey and light grey arrows indicate the positions selected for the EDX analysis (associated EDX spectra with corresponding colour). Pink spectra depict blank measurements of the silicon wafer. ....72

**Figure 51:** Cl<sup>-</sup> formation during the 60-days reaction of dissolved PCE with Mg/Al particles in a column reactor. ....74



## List of Tables

<b>Table 1:</b>	Mobility parameters for NANOFEAR 25S particles in different porous media before and after porous media were coated with 10 g/L Na humate.....	10
<b>Table 2:</b>	Percentage of PCE degradation into different reaction products during ca. 2 months reaction between a PCE NAPL and NANOFEAR 25S particles in a column reactor. The ratio of the corroded over consumed Fe(0) is also indicated. ....	13
<b>Table 3:</b>	Properties of NANOFEAR STAR particles in modified suspensions. PSD: particle size distribution.....	16
<b>Table 4:</b>	Mobility parameters for NANOFEAR STAR particles in suspension stabilized with 3% PAA. ....	20
<b>Table 5:</b>	Stability parameters for milled ZVI in pure aqueous and agar agar-stabilized suspension.....	28
<b>Table 6:</b>	Selected characteristics of PM used in column experiments.....	29
<b>Table 7:</b>	Mobility parameters for agar agar-stabilized milled ZVI. ....	31
<b>Table 8:</b>	Summary of kinetic data for TCE dehalogenation under different conditions with calculated apparent corrosion rates for bare and agar agar-stabilized milled ZVI particles. ....	33
<b>Table 9:</b>	Mineralogical composition of milled ZVI at the beginning of experiment and after 7 and 105 days of contact with aquifer material from the Solvay, CH and the Balassagyarmat, HU field sites determined by XANES. Fit range: -12 eV–36 eV above the edge. ....	34
<b>Table 10:</b>	Degradation pathway of PCE via milled ZVI and percent of anaerobic corrosion as determined in column reactor. ....	35
<b>Table 11:</b>	Mobility parameters and estimated transport distances for CMC-stabilized Carbo-Iron® in M.I under the injection conditions. ....	40
<b>Table 12:</b>	Mobility parameters and estimated transport distances for CMC-stabilized Carbo-Iron® in porous medium and groundwater from the Balassagyarmat field site, HU under the injection conditions. ....	41
<b>Table 13:</b>	Calculated equilibrium concentrations for freely dissolved ( $C_{CMC, free}$ ) and CMC loaded on particles ( $\rho_{CMC on particles}$ ) from sorption isotherm measurements ( $C_{particles} = 20$ g/L). ....	42
<b>Table 14:</b>	Freundlich parameters calculated for Carbo-Iron®, activated carbon colloids and Carbo-Iron® for the sorption of two contaminants. Note that there are no parameters for Carbo-Iron® and PCE due to significant PCE degradation during the sorption experiment. ....	45
<b>Table 15:</b>	Physical-chemical properties of Trap-Ox Fe-zeolites. ....	48
<b>Table 16:</b>	Particle size and zeta potential for Trap-Ox Fe-zeolites in suspensions with various pH. ....	50
<b>Table 17:</b>	Mobility parameters for optimized Trap-Ox Fe-zeolites ( $C_{0 (particle)} = 10$ g/L) in various porous media and fluids. ....	51
<b>Table 18:</b>	Changes in elemental composition (related to dry mineral phase), BET specific surface area, catalytic activity (MTBE, TCE) and MTBE adsorption of Trap-Ox Fe-BEA35 before and after being aged for 38 days. ....	53
<b>Table 19:</b>	Size distribution and zeta potential of bionanomagnetite in modified- and pure aqueous suspensions. ....	57
<b>Table 20:</b>	Mobility parameters for bionanomagnetite particles in various stabilized suspensions. ....	59
<b>Table 21:</b>	Summary of kinetic data for TCE dehalogenation by palladized bionanomagnetite. $K_{obs}$ is pseudo first order reaction rate constant, $K_{pd}$ is reaction rate constant normalized to concentration of Pd, and $A_{pd}$ is specific catalyst activity.....	63
<b>Table 22:</b>	Experimental conditions for cascading column experiment with Nano-Goethite. ....	65
<b>Table 23:</b>	Mobility parameters for optimized Nano-Goethite particles.....	65



**Table 24:** Transport parameters for Nano-Goethite as delivered by the MNMs model.  $q_c$ : flow rate;  $r_c$ : theoretical distance from the injection well;  $n_{modelled}$ : modelled porosity;  $a_x$ : longitudinal dispersivity;  $k_a$ : attachment rate;  $k_d$ : detachment rate. Note that  $q_c$  and  $r_c$  are measured, while the remaining parameters are calculated. ....66

**Table 25:** Detailed experimental condition in batch reactors for studying toluene and benzoate biodegradation and corresponding Fe(III) reduction within Nano-Goethite. ....68

**Table 26:** Degradation rates and Fe reduction rates during the Nano-Goethite-assisted biodegradation of toluene and benzoate. ....69

## Glossary

<b>Attachment efficiency (<math>\alpha</math>)</b>	Ratio between the number of the contacts of suspended particles and the grain surface which result in attachment divided by the total number of collisions/contacts which occur between suspended particles and the grains of the porous media (surface of porous media)
<b>BET specific surface area</b>	Specific surface area determined by the BET (Brunauer, Emmett and Teller) method
<b>Cascading column experiments</b>	Experiment that simulate the injection in aquifers of NP suspension and allows the prediction of NP distribution around the well
<b>Colloid filtration theory (CFT)</b>	Describes the deposition of particles in a porous medium involving two sequential steps: transport from the fluid to the grains of the filter/porous media, and attachment to the grains
<b>CMC</b>	Carboxymethyl cellulose
<b>Delivery</b>	Refers to bringing of NPs to the desired distance from the particle injection point. Here studied by means of cascading column experiments
<b>DCE</b>	Dichloroethylene
<b>D.I</b>	Refer to small columns ( $L < 20\text{--}30$ cm) without spatial information
<b>D.II</b>	Refer to columns ( $L > 20\text{--}30$ cm) with spatial information including cascading columns
<b>DLS</b>	Dynamic light scattering
<b>DOC</b>	Dissolved organic carbon
<b>EDX</b>	Energy-dispersive X-ray spectroscopy
<b>Effective porosity (<math>n_e</math>)</b>	The ratio of the part of the pore volume where the water can circulate to the total volume of a representative sample of the medium
<b>F.I.s</b>	Soft standard water (US EPA, 2002)
<b>F.I.m</b>	Moderately hard standard water (US EPA, 2002)
<b>F.I.h</b>	Very hard standard water (US EPA, 2002)
<b>F.II</b>	Groundwater from Balassagyarmat, HU field site
<b>F.II.a</b>	Artificial groundwater in accordance with the drinking water composition provided by the Drinking Water Supply Association "Lake Constance" ZVBWV (alkalinity and water hardness similar to that of F.I.m)
<b>GC</b>	Gas chromatography
<b>HAADF-STEM</b>	High angle annular dark field scanning transmission electron microscopy
<b><math>k_{obs}</math></b>	Observed pseudo-first order reacton rate constant
<b>LSF experiment</b>	Large scale flume experiment

<b>L<sub>T50</sub></b>	Predicted travel distance acc. CFT, 50% of particles removed
<b>L<sub>T63</sub></b>	Predicted travel distance acc. CFT, 63% of particles removed
<b>L<sub>T99,9</sub></b>	Predicted travel distance acc. CFT, 99.9% of particles removed
<b>M.I</b>	Dorsilit® 8 sand
<b>Mobility</b>	Refers to ability of NPs to move through a porous medium after the injection or along with groundwater flow. Here studied by means of D.I and D.II column experiments
<b>M.II</b>	VEGAS sand
<b>NOM</b>	Natural organic matter
<b>NP(s)</b>	Nanoparticle(s)
<b>PAA</b>	Polyacrylic acid
<b>PCE</b>	Tetrachloroethene or perchloroethylene
<b>PM</b>	Porous media, porous medium
<b>Radius of Influence (ROI)</b>	The radius to which an injected suspension fluid is being transported (independently of the NP), in other words, the distance an injected conservative tracer would migrate.
<b>SEM</b>	Scanning electron microscopy
<b>Stability</b>	Stability of a nanoparticle suspension is ensured if the change in particle concentration (mass or number) in the suspension and their particle size distribution as a function of time does not exceed pre-defined criteria. Stability criteria, i.e., change in particle concentration and size distribution with time, are to be defined depending on the intended use of the suspension.
<b>TEM</b>	Transmission electron microscopy
<b>TCE</b>	Trichloroethylene
<b>VC</b>	Vinyl chloride
<b>XAS</b>	X-ray absorption spectroscopy
<b>XRD</b>	X-ray diffraction
<b>XRF</b>	X-ray fluorescence

## 1 Introduction to DL 4.2

### 1.1 Stability of NP suspensions

Stability of NPs is the ability of a particle suspension to resist aggregation and sedimentation for a specified time.

In order to be effective, NPs used in remediation need to form stable suspensions, which can be delivered in water-saturated porous media to the contaminated zone.

Stability of NP suspension was evaluated either in a graduated cylinder test according to the Standardized experimental protocols or by means of sedimentation rate. Sedimentation rate was determined by monitoring the transmittance of monochromatic light from the suspension (Turbiscan LAB, Quantachrome, Germany). In a stable NP suspension (an example shown in Figure 1), NPs sedimentation rate was  $< 0.5$  m/d.

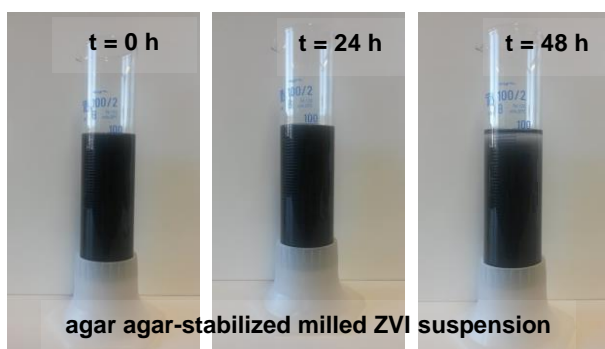


**Figure 1:** An example of agar agar-stabilized milled ZVI suspension at the beginning of the stability test (left), after 24 h (middle) and after 48 h (right).  $c_{\text{agar agar}} = 1$  g/L;  $c_{\text{particle}} = 1$  g/L. Sedimentation rate ca. 0.1 m/d. Photo: Doris Schmid, UNIVIE.

### 1.2 Delivery and Mobility of NPs

Delivery and mobility of NPs are interrelated concepts of NP movement through saturated porous media.

More specifically, **delivery** of NPs refers to bringing of NPs in an amount required for aquifer restoration to the desired distance (contaminated zone) from the particle injection point. At NanoRem test field sites, NPs were delivered into the subsurface via direct push or well injection technique.

Besides being controlled by the injection method (including the injection rate and pressure), delivery of NPs into the subsurface can be enhanced by improving surface properties of NPs or properties of NP suspension (e.g. suspension viscosity). Depending on the composition of NP suspension, delivery can also be “tailored” to a desired distance (radius of influence). In WP4 delivery of NPs was studied by means of cascading column experiments according to Standardized experimental protocols.

**Mobility** of NPs refers to ability of NPs to move through a porous medium after the injection or along with groundwater flow. Mobility of NPs in water-saturated porous media was here predicted on the basis of particle breakthrough curves resulting from the D. I or D.II column experiments carried out either at the injection- or groundwater flow conditions according to Standardized experimental protocols.

### 1.3 Fate of NPs

Fate of NPs upon their release into the environment depends on their physicochemical properties (e.g., size, chemical composition, surface charge and coating), environmental conditions (such as O<sub>2</sub> content, redox conditions, pH, ionic strength, and organic matter content (Jang et al., 2014)) and exposure duration, as illustrated in Figure 2.

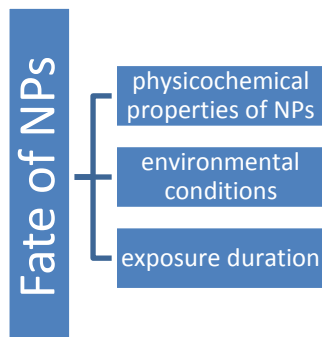


**Figure 2:** Factors influencing fate of NPs.

Fate of NPs implies various aspects of NP transformation, including chemical transformation, dissolution, surface charge transformation and can lead to various transformation products. The degree of transformation is expected to affect overall reactivity and potential toxicity of NPs (the latter not addressed by this report, but included in DL 5.1 (Dose response relationships, Matrix effects on Ecotox) and DL 5.2 (Influence of Transformation and Transport on Ecotox)). Understanding the transformation of NPs upon release to the environment is critical to evaluating the potential efficiency as well as risk of NPs used for environmental remediation.

In this report, various aspects of particle fate are included: particle reactivity with respect to contaminants, particle efficiency, lifetime, anaerobic corrosion, contaminant sorption by particles, as well as morphological, chemical and mineralogical changes of NPs. Fate of NPs was observed over a prolonged period, from a few days to one year under the experimental conditions created to resemble those at field sites.

### 1.4 Optimization of NPs

Optimization of NPs was carried out in different ways:

1. Adding selected stabilizers (polymers) in different concentrations into suspension of particle with a defined particle concentration. These stabilizers are supposed to prevent particle aggregation over prolonged timeframes by:
  - (i) Altering surface properties of particles (such as zeta potential)
  - (i) Lowering size and sedimentation rate of particle aggregates
  - (iii) Altering properties of suspension itself (such as viscosity)
2. Varying concentration of both particles and stabilizers in particle suspension
3. Particle activation (for optimized reactivity)
4. Altering chemical composition of particle (e.g. Fe<sub>tot</sub> content, addition of Pd, or Mg/Al content)

## 2 Optimized Nanoparticles

Performance of following optimized nanoparticles is included in this report:

1. Carboxymethyl cellulose (CMC)-stabilized **NANOFER 25S (NANO IRON s.r.o.)**. Also the report on long term fate of NANOFER 25S is included, since these particles were injected at Spolchemie I field site, CZ. Mobility of NANOFER 25S in (with polymer) modified porous medium is as well part of this report
2. **NANOFER STAR (NANO IRON s.r.o.)** stabilized with polyacrylic acid (PAA), ester derived from glycerol (EMG), terpenes (TER), Na salt of polyacrylic acid (Ax), CMC and a non-odorized detergent (mixture of hydrated alkaline-metals salts and aliphatic carboxylic acids). Reports on activated NANOFER STAR (according to the protocols provided by NANO IRON s.r.o.) and Radiolabelled NANOFER STAR are also included
3. Agar agar-stabilized **milled ZVI particles, FerMEG12 (UVR-FIA GmbH)**. Also the report of reactivity of pure FerMEG12 particles is reported, since these particles were injected in Solvay field site, CH
4. CMC-stabilized and pure **Carbo-Iron® (SciDre GmbH, UFZ Leipzig)** particles
5. **Trap-Ox Fe-zeolites (UFZ Leipzig)** with optimized chemical composition
6. **Bionanomagnetite and Palladized bionanomagnetite (University of Manchester)** and pure and stabilized with agar agar, guar gum, starch and humic acid sodium salt
7. **Nano-Goethite (University of Duisburg-Essen)** stabilized with humic acid and
8. **Mg/Al particles (VEGAS, University of Stuttgart)** with optimized Mg/Al ratio

## 3 Objectives of DL 4.2

Objective of DL 4.2 is to summarize the outcomes of numerous experiments carried out with optimized NPs under field relevant conditions and to conclude on:

- (i) Stability of optimized nanoparticles, emphasizing important stability parameters (such as zeta potential, particle size or chemical composition)
- (ii) Mobility and delivery of optimized nanoparticles (also in heterogeneous porous media from NanoRem field sites) and on transport parameters, which can be used for upscaling and computational modelling of large-scale applications and
- (iii) Long term fate of NPs under field relevant conditions.

Field relevant experimental conditions imply to field relevant particle concentration, contaminant type and concentration, porous medium, water composition and flow velocities.

## 4 Results on stability, mobility, delivery and fate of optimized NPs under field relevant conditions

### 4.1 NANOFER 25S (NANO IRON s.r.o.)

Responsible partner: USTUTT

Contributors: UNIVIE, BRGM, CEREGE, UFZ, UPOL

NANOFER 25S particles are commercially available in an aqueous suspension, which is composed of 16% Fe(0), 4% magnetite (Fe<sub>3</sub>O<sub>4</sub>), 1% C, 77% H<sub>2</sub>O and 3% polyacrylic acid (PAA). The particles have spherical shape with a mean diameter of primary particles  $d_{\text{mean}} < 50$  nm and a BET specific surface area  $> 25$  m<sup>2</sup>/g (data from the producer).

Optimization of NANOFER 25S particles was carried out in terms of providing better stability of particle suspension (and thus their mobility), which was achieved by addition of carboxymethyl cellulose (CMC).

#### 4.1.1 Stability of NANOFER 25S

*CMC successfully stabilizes NANOFER 25S suspension ( $c_{\text{particle}} \sim 10$  g/L Fe(0),  $c_{\text{CMC}}$  up to 10 g/L). Suspension viscosity is a function of CMC concentration; up to  $c_{\text{CMC}} \leq 10$  g/L the suspension exhibits Newtonian fluid behaviour, while for higher CMC concentrations rheological behavior of the fluid was observed.*

**Experimental protocol** Optimized suspension of NANOFER 25S particles was obtained by addition of CMC (type Walocel CRT 30 GA, Dow Industrial Cellulosics GmbH, Germany) solution in different concentrations (0.1, 2.5, 10 and 20 g/L). CMC powder was dispersed (for 15 min) with degassed tap water using an Ultra Turax T 25 and allowed to swell for ca. 24 h. Various CMC solutions, and CMC-stabilized NANOFER 25S suspensions were characterized in terms of viscosity and shear rates.

**Results** Contrary to literature (Adel Benchabane, 2008), all CMC solutions with up to 10 g/L CMC, behaved as a Newtonian fluid. Addition of 10 g/L NANOFER 25S particles to these solutions did not influence the fluid properties. In contrast to that, particle suspensions with  $\geq 20$  g/L CMC showed shear thinning behaviour. Given that their viscosities were above the practical range for field application the latter suspensions were not investigated further.



#### 4.1.2 Mobility and Delivery of NANOFER 25S

*NANOFER 25S in an optimized particle suspension with  $c_{particle} = 10$  g/L and  $c_{CMC} = 10$  g/L can be delivered into porous medium M.II to ca. 0.6 m from the injection point.*

*Possibility of enhancing the mobility of NANOFER 25S in porous media by modifying the surfaces of mineral grains (with 10 mg/L Na humate) is limited to only homogenous, well sorted, highly porous and permeable aquifers, rarely found at brownfield sites. This benefit is insufficient and therefore not recommended for field applications.*

**Experimental protocol** Radial migration of optimized NANOFER 25S suspensions and thus delivery of the particles into porous medium was studied in cascading column experiments filled with M.II porous medium. The concept of cascading columns is described by Comba and Braun (2012). Particle suspensions, containing particles in the range of 0.5 to 10 g/L and CMC in the range of 0 to 12 g/L, were injected under the flow velocity of  $15.91 \text{ m/d} < v_{\text{eff}} < 72.77 \text{ m/d}$ . Pressure difference between inflow and outflow was recorded during the injection, using a differential pressure transducer. Fluid samples were taken from both inflow and outflow of the columns and their Fe(0) content was used to calculate a mass balance. A specially designed scanner for magnetic susceptibility measurement (Hua, 2015) was used to monitor (both in time and space) the transport and distribution of CMC-stabilized NANOFER 25S particles. Detailed information on the set of cascading column experiments, including the column dimensions, flow rates and pressure changes is included in Table A1 in Appendix.

Moreover, a possibility to enhance mobility of NANOFER 25S (in pure aqueous suspensions, as delivered from the producer, without addition of CMC) was tested in a set of column experiments (2.5 cm i.d., 15 cm saturated packed bed length) in which different porous media were coated with Na humate (HUMIN-S 775, Humintech®, Düsseldorf, Germany). *The rationale for the coating of porous media was to decrease the attachment of NANOFER 25S to the mineral grains, via electrostatic repulsion between the PAA coating of NANOFER 25S particles and Na humate coating onto mineral grains.* Na humate at concentration of 10 mg/L was selected for porous media coating, after the set of experiments with different concentrations of both Na humate and lignosulfonate were tested (and reported in IDL 4.3 (Report on the stability, mobility, and enhanced delivery of NP for optimized NPs as well as on the data on aquifer modifications for controlled NP delivery)). Solution of Na humate and the NANOFER 25S particle suspension were prepared in near-natural water with moderate hardness (F.I.m). For comparison, the set of pre-experiments with ultrapure water were also carried out and the results reported in IDL 4.3. The effect of Na humate coating on NANOFER 25S mobility was studied in columns packed with four different porous media: (i) Dorsilit® PM (M.I), (ii) VEGAS PM (M.II), (iii) PM from Spolchemie I field site, CZ and (iv) PM from Solvay field site, CH. NANOFER 25S mobility tests were carried out both in columns preconditioned only with F.I.m fluid and in the columns into which Na humate was pre-injected for coating of mineral surfaces. After the column conditioning and the injection of Na humate, suspension of NANOFER 25S ( $c_{particle} = 1$  g/L) was injected. All column experiments were carried out under the injection conditions with a flow velocity of ca. 100 m/d. Breakthrough of Na humate and of NANOFER 25S was monitored via UV-vis spectroscopy (at wavelength of 254 nm) and  $Fe_{\text{tot}}$  content (ICP-OES), respectively. All the tests were done at least in three replicates. NANOFER 25S particles in F.I.m suspension were characterized in terms of average size (MasterSizer 2000) and zeta potential (ZetaSizer Nano ZS). Porous media were characterised

in terms of chemical composition (ICP-MS, LECO RC-612 Carbon Analyzer), mineralogical composition (Panalytical PW 3040/60 X'Pert PRO), size (sieving) and zeta potential for both cases, with and without Na humate-coating (SurPASS, Anton Paar). Details on characterisation of porous media and on the experimental setup, as well as the outcomes of pre-experiments are reported in IDL 4.3. An effect of Na humate on the activity of indigenous bacteria in aquifers was also studied in batch reactors with enriched nitrate-reducing bacterial cultures (detailed information on the experimental procedure is included in IDL 4.3).

**Results (Cascading column experiments)** An optimal particle delivery to 0.5–0.6 m (with an allowable pressure change of  $\Delta p = 0.9$  bar) was achieved with CMC-modified suspensions containing 10 g/L Fe(0) and 5–10 g/L CMC. Particle suspensions with smaller particle content ( $0.5 \text{ g/L} < c_{\text{particle}} < 5 \text{ g/L}$ ) were less mobile compared to these with higher particle concentrations ( $5 \text{ g/L} < c_{\text{particle}} < 10 \text{ g/L}$ ). For the particle suspensions with  $c_{\text{particle}} = 10 \text{ g/L}$  the increase of CMC content from 0 to 10 g/L CMC resulted in increased particle transport distances. Further increase of CMC concentration did not significantly alter the mobility of optimized NANOFER 25S (Figure 3), neither was the particle mobility further increased by the prolonged duration of the experiment. Details on the particle travel distance depending on the experimental setup are included in Table A1 in Appendix.

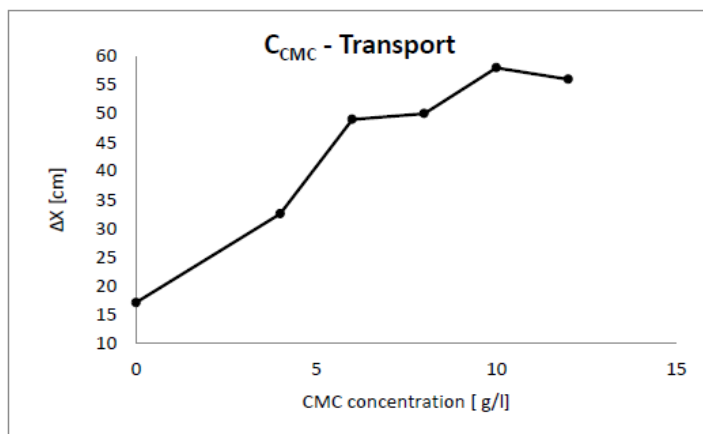


**Figure 3:** Transport distance ( $\Delta x$ ) of optimized NANOFER 25S particles in suspensions with 10 g/L Fe(0) as a function of the CMC concentration.

**In conclusion**, NANOFER 25S in fairly concentrated particle suspension ( $c_{\text{particle}} = 10 \text{ g/L}$ ) and 5–10 g/L CMC can be delivered into M.II porous medium up to 0.5–0.6 m from the injection point.

**Results (Enhancing NANOFER 25S mobility via Na humate-coating of porous media)** NANOFER 25S particles in F.I.m suspension had an average size of  $6.2 \pm 1.1 \mu\text{m}$  and a zeta potential of  $25 \pm 4 \text{ mV}$ . After the injection of Na humate solution in F.I.m, no significant changes were observed in an overall zeta potential of porous media grains, which were ca. -28 mV for M.I (moderately good sorted homogenous standard quartz sand), ca. -25 mV for M.II (poorly sorted heterogeneous standard sand), ca. -13 mV for PM from Spolchemie I field site, CZ (poorly sorted PM, containing ca. 6% of Fe oxides) and ca. -18 mV for PM from Solvay field site, CH (poorly sorted PM, containing ca. 37% of carbonate). The effects of Na humate-coating of porous media on zeta potential is in fact expected (especially for PM with surface charge heterogeneities), but was indeed not identified in the overall surface potential data.

There was an improvement of NANOFER 25S mobility in moderately good sorted homogenous M.I porous medium with the highest porosity and therefore permeability (Table 1) after the coating of mineral grains with Na humate. The particle breakthrough increased from  $c/c_0 = 0.1$  in intact porous medium to  $c/c_0 = 0.4$  in the Na humate-coated porous medium (Figure 4A). Na humate breakthrough data also showed that ca. 10% of the injected Na humate solution attached to the mineral grains (data not shown). This indicated that the attached Na humate provided better electrostatic repulsion between the coated mineral surfaces and PAA-coating on the NANOFER 25S, enhancing the particle transport. Estimated max transport distances  $L_{T,99,9}$  increased 6-fold, from 0.3 m to 1.8 m (Table 1).

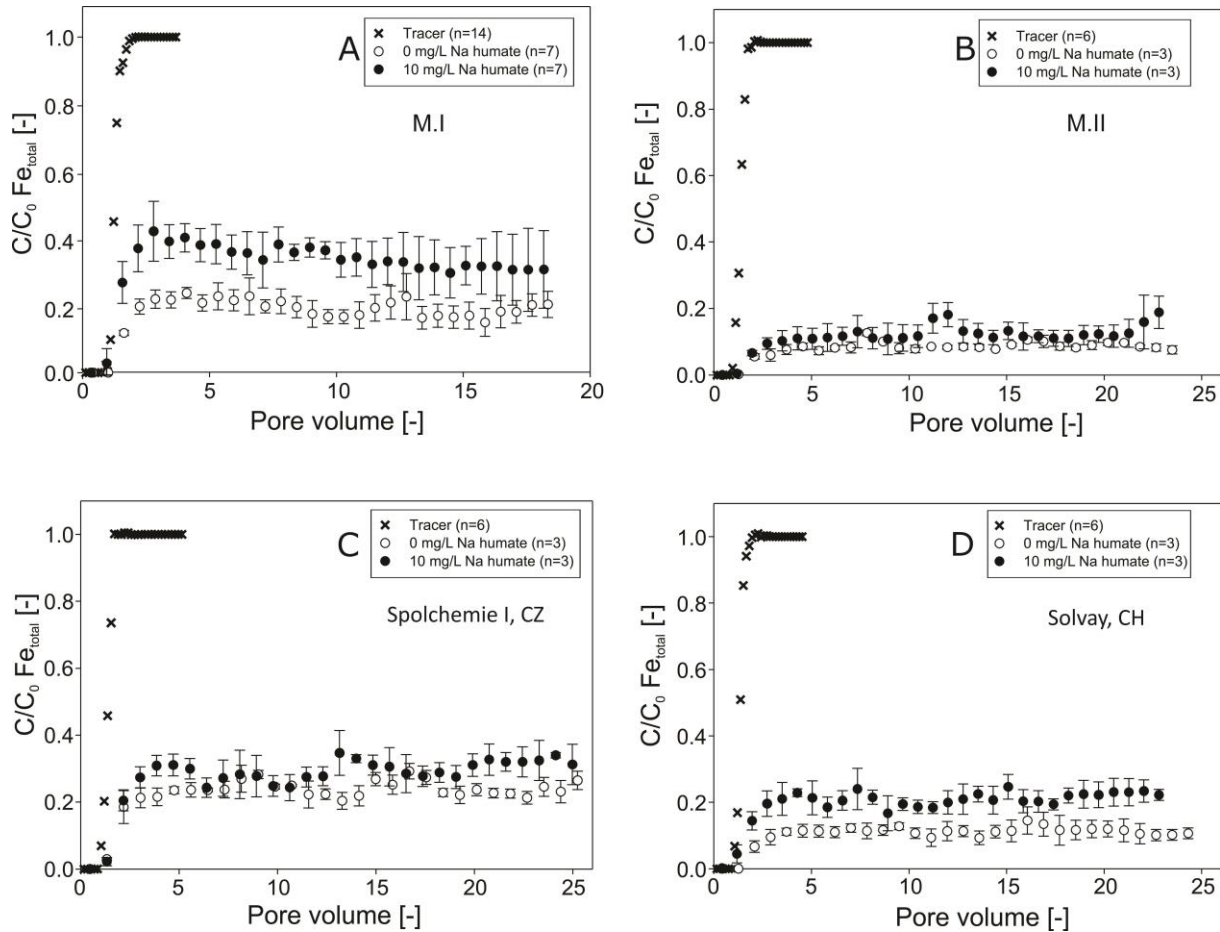


**Figure 4:** Mean breakthrough curves for NANOFER 25S (measured as  $Fe_{tot}$ ) and the corresponding standard deviation before and after the injection of 10 mg/L solution of Na humate in M.I (A), M.II (B), PM from Spolchemie I field site, CZ (C) and PM from Solvay field site, CH (D); n is number of replicates; Injection velocity: 100 m/d; initial particle concentration: 1 g/L.

**Table 1:** Mobility parameters for NANOFE R 25S particles in different porous media before and after porous media were coated with 10 g/L Na humate.

NPs	C <sub>0</sub> (NP) [g/L]	Porous media (PM)	n <sub>e</sub> [%]	Fluid	V <sub>eff</sub> [m/d]	k [1/s]	α [-]	L <sub>T</sub> (50%) [m]	L <sub>T</sub> (63%) [m]	L <sub>T</sub> (99.9%) [m]	L <sub>T</sub> (99.9%) pristine PM/ Na humate coated PM
NANOFE R 25S	1	M.I	39.7	F.I.m	100	1.9E-2	0.14	0.03	0.04	0.31	6
NANOFE R 25S	1	Na humate-coated M.I	39.7	F.I.m	100	9.2E-3	0.12	0.18	0.25	1.79	
NANOFE R 25S	1	M.II	26.7	F.I.m	100	3.2E-2	0.14	0.03	0.04	0.29	1
NANOFE R 25S	1	Na humate-coated M.II	26.7	F.I.m	100	2.8E-2	0.12	0.03	0.05	0.32	
NANOFE R 25S	1	Spochemie I, CZ	26.6	F.I.m	100	1.9E-2	0.13	0.05	0.07	0.48	1
NANOFE R 25S	1	Na humate-coated Spochemie I, CZ	26.6	F.I.m	100	1.6E-2	0.11	0.06	0.08	0.57	
NANOFE R 25S	1	Solvay, CH	28.3	F.I.m	100	2.7E-2	0.12	0.03	0.04	0.31	1
NANOFE R 25S	1	Na humate-coated Solvay, CH	28.3	F.I.m	100	1.9E-2	0.09	0.04	0.06	0.44	

No improvement of NANOFE R 25S mobility in M.II after the mineral coating with Na humate was observed (Figure 4B and Table 1). On the base on a slight shift upwards of NANOFE R 25S breakthrough in PM from Spolchemie I, CZ and Solvay, CH field sites after the Na humate coating (Figure 4C&D) it was suggested that Na humate was able to prevent the attachment of a (very) small portion of NANOFE R 25S particles. Nevertheless, as demonstrated by the estimated transport parameters (Table 1) this was not efficient enough to significantly improve the mobility of NANOFE R 25S particles.

Even 50-fold higher concentration of Na humate (500 mg/L) did not exhibit a negative impact on the activity and biomass of the nitrate-reducing indigenous bacteria, which is also expected for the concentrations applied for mineral coating (10 mg/L). Na humate was also not degraded by the bacteria. A more detailed report on this is included in IDL 4.3.

**In conclusion**, the possibility of hindering NANOFE R 25S deposition in porous media by coating of mineral grains within the aquifer with 10 mg/L Na humate is limited. A positive effect was only observed in homogenous, well sorted, highly porous and permeable aquifers, rarely found at brown-field sites. The results show that the benefit of aquifer modification by Na humate is insufficient to justify the anticipated additional costs and time. Nevertheless, the outcomes of these experiments clearly reduced the number of possibilities to be taken into account for optimal particle delivery and mobility.

#### 4.1.3 Fate of Nanofer NANOFER 25S under field relevant conditions

The following aspects of fate of NANOFER 25S under field relevant conditions were studied:

- **reactivity** with respect to PCE NAPL and **anaerobic corrosion** in a column reactor filled with porous medium from Spolchemie I, CZ field site (where these particles were actually applied), (experiment duration ca. 2 months)
- Particle **oxidation and Fe speciation** in batch reactor with groundwater from Spolchemie I, CZ field site (batch reactor, experiment duration ca. 8 days)

Since NANOFER 25S was applied at the Spolchemie I, CZ field site in aqueous suspensions (not containing CMC), these pristine suspensions were also used to test the fate under field relevant conditions.

*NANOFER 25S particles corrode fast. In the contact with the groundwater from Spolchemie I, CZ field site NANOFER 25S oxidizes to green rust (after 3 days) and then to ultra-small ferric oxides/oxyhydroxides. Major (final) degradation products of PCE NAPL in reaction with NANOFER 25S were ethene (dominating) and ethane. 92% of the overall consumed Fe(0) was anaerobically corroded within 56 days.*

**Experimental protocol** Reactivity of NANOFER 25S in the presence of a PCE NAPL was studied for 54 days in a column (3.6 cm i.d., 194 cm saturated packed bed length, following the Experimental Protocols) filled with Dorsilit® PM (M.I). The column was divided into 3 zones: a 10 cm long inflow buffer zone (contained M.I only), a 134 cm long reactive zone (contained M.I and NANOFER 25S particles) and a 50 cm long outflow buffer zone (contained M.I only). The amount of NANOFER 25S particles within the reactive zone was  $m_{\text{Fe}(0) \text{ initial}} = 13 \text{ g}$ , designed to account for complete degradation of PCE to ethane and to allow for side reactions (e.g. anaerobic corrosion). 1 mL pure PCE was emplaced into the reactive zone. A blank column (without NANOFER 25S particles) was run in parallel. Degassed tap water (F.II,  $c_{\text{O}_2} = 0.7\text{--}1 \text{ mg/L}$ ) was continuously injected into the columns at  $v_{\text{eff}} = 0.5 \text{ m/d}$ . At the outflow of the columns stainless steel valves were installed for monitoring the concentration of PCE and the degradation products (by HPLC and GC, respectively). Gaseous reaction products and by-products ( $\text{H}_2$  formed due to anaerobic corrosion) were collected in a gas trap and analysed by GC.  $\text{Cl}^-$  in the effluents was measured by potentiometric titration. Temperature was kept at  $25.2 \text{ }^\circ\text{C}$ . Changes in Fe(0) concentration during the experiment were tracked based on magnetic susceptibility measurements (Li et al., 2015).

Particle oxidation was investigated at  $25 \text{ }^\circ\text{C}$  under both anoxic and oxic conditions ( $c_{\text{particles}} = 5 \text{ g/L}$  in F.I.s (pH 7.8)). Alteration of particles was studied over a two-month period using electron and X-ray based techniques (TEM, HAADF-STEM, XRD, XAS). Measurements were complemented by recording the evolution of magnetic properties. Furthermore, particle oxidation was analysed for 8 days at room temperature in closed 2.5 L reactors containing  $c_{\text{Fe}(0)} = 0.5 \text{ g/L}$ , groundwater from Spolchemie I, CZ field site with accompanying contaminants (*cis*-DCE (16.3 mg/L), PCE (5.3 mg/L), TCE (1.9 mg/L), VC (1.4 mg/L)). Oxidation products were characterized by means of transmission  $^{57}\text{Fe}$  Mössbauer spectroscopy performed on frozen samples. Since it was necessary to extract a significant portion of Fe solids for detailed analysis, separated reactors were used for each reaction time interval of 1, 3, 6, and 8 days.

**Results (NANO FER 25S reactivity with respect to PCE NAPL)** 13–29 days after the experiment start, an accelerated dissolution of PCE was observed in the column reactor (compared to the blank column) with a peak of 85 mg/L (Figure 5). At the end of the experiment ca. 30% of the introduced PCE NAPL was discharged from the column reactor, simultaneously via dissolution and convective transport.

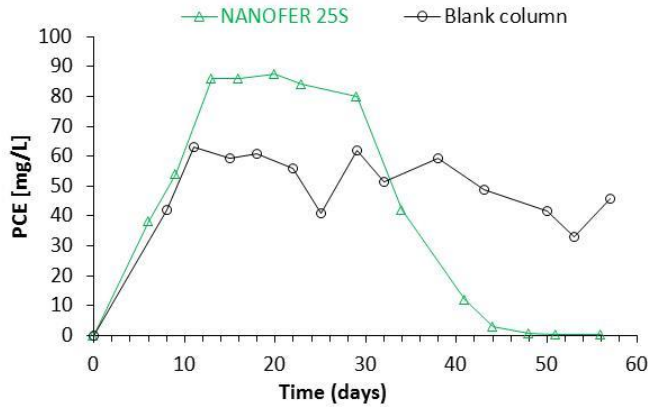


**Figure 5:** PCE concentration profile over reaction time in effluents of a column reactor (with NANO FER 25S particles, green line) and of a blank column (black line).

Highest  $\text{Cl}^-$  concentrations were detected between day 9 and 33, followed by a decrease. PCE degradation in terms of  $\text{Cl}^-$  formation ( $\text{PCE} \rightarrow \text{Cl}^-$ ) amounted to 30% (a cumulative  $\text{Cl}^-$  formation is shown in Figure 6, left). However, this does not consider the formation of intermediates. Only traces of *cis*-DCE, *trans*-DCE and VC were detected. The major intermediate degradation product was TCE (5%). Final dechlorination products were ethene (dominating) and ethane. 92% of the consumed NANO FER 25S (taking into account  $\text{Cl}^-$ ,  $\text{H}_2$  and ethane formation) was anaerobically corroded (Table 2). On the basis of magnetic susceptibility data (Figure 6, right), Fe(0) content along the column decreased for 63% during ca. 2 months of the reaction time.

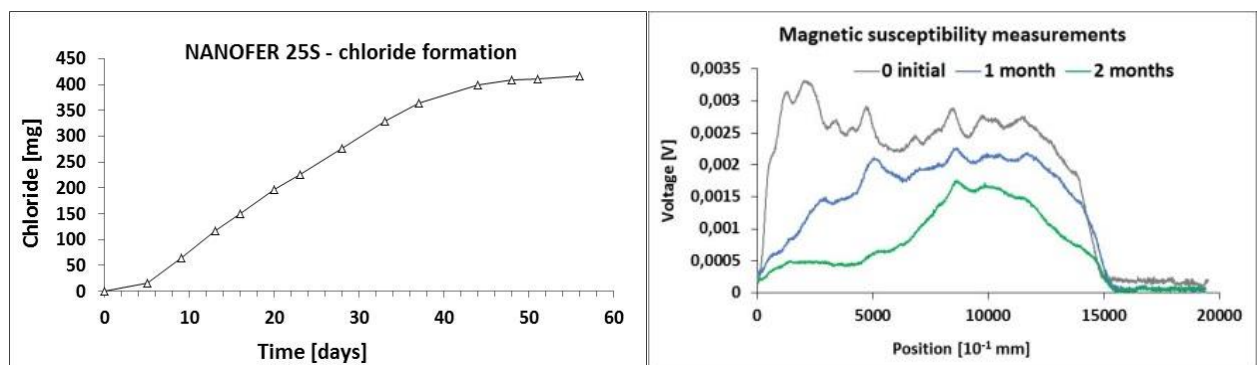


**Figure 6:** Cumulative curves showing  $\text{Cl}^-$  formation (left) and magnetic susceptibility measurements used to trace changes in Fe(0) concentration along the column (right).



**Table 2:** Percentage of PCE degradation into different reaction products during ca. 2 months reaction between a PCE NAPL and NANOFEER 25S particles in a column reactor. The ratio of the corroded over consumed Fe(0) is also indicated.

Degradation product	PCE degradation [%]
Cl <sup>-</sup>	30
TCE	5
ethene	11
ethane	6
$m_{\text{corroded Fe(0)}}/m_{\text{overall consumed Fe(0)}}$	92

**Results (Oxidation of NANOFEER 25S and Fe speciation)** Only  $17 \pm 2\%$  of Fe(0) under anoxic and  $1 \pm 0.1\%$  of Fe(0) under oxic conditions remained, after NANOFEER 25S particles were exposed for 2 days to soft water (F.I.s). This result confirmed a faster degradation of particles in the presence of dissolved O<sub>2</sub>. TEM and HAADF-STEM micrographs confirmed the core-shell structure (made of Fe(0) and Fe oxides, respectively) of fresh NANOFEER 25S. Due to the oxidation in F.I.s fluid, Fe oxide layer became irregular in shape with smaller Fe oxide nanoparticles formed. In only 3 days contact at room temperature with the groundwater from Spolchemie I, CZ field site, NANOFEER 25S transformed into green rust. This was followed by the oxidation of green rust after 8 days of aging into ultra-small ferric oxides/oxyhydroxides, as determined by Mössbauer spectra (see Figure 7).



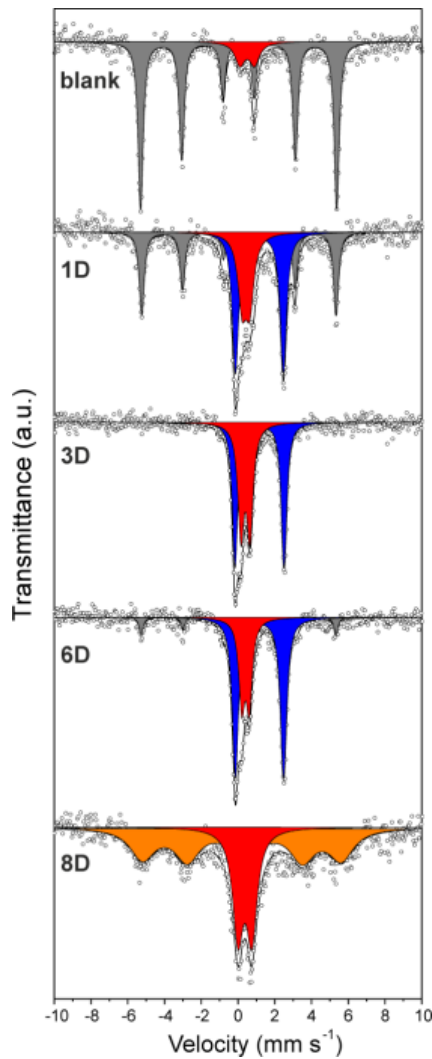


**Figure 7:** An example of Mössbauer spectra of NANOfer 25S aged in groundwater from Spolchemie I, CZ field site. Gray: Fe(0); red: Fe<sup>3+</sup>, blue: Fe<sup>2+</sup>, orange: superparamagnetic ferric oxides/oxyhydroxides. Aging time: 8 days.

**In conclusion,** the results of the tests in batch and column reactors showed that NANOfer 25S is highly sensitive to oxidation. This may result in fast and significant losses of Fe(0) during a field application, due to anaerobic corrosion and/or reaction with the electron acceptors other than contaminants, such as nitrate or sulfate and consequently less utilization of Fe(0) for contaminant degradation.

## 4.2 NANOFER STAR (NANO IRON s.r.o.)

Responsible partner: USTUTT

Contributors: UNIVIE, BRGM, CEREGE, UFZ, UPOL

NANOFER STAR (NANO IRON s.r.o.) is an air-stable nanoscale zero-valent iron powder, consisting of a Fe(0) core stabilized by a Fe oxide shell.

Previous tests showed that initial NANOFER STAR (provided at the beginning of the project, hereafter inactivated NANOFER STAR) was not stable in aqueous suspension. Therefore, optimization of NANOFER STAR particles was carried out in terms of increasing the suspension stability by addition of the following polymers: 3% PAA, 0.1% ester derived from glycerol (EMG) and 0.5% and 2% terpenes (TER). In addition to modifying particle suspensions, NANOFER STAR was activated according to the protocols provided by NANO IRON s.r.o. (hereafter activated NANOFER STAR).

Additionally, suspensions of NANOFER STAR particles (Fe(0) : H<sub>2</sub>O = 1 : 4) were modified by addition of 3% Na salt of polyacrylic acid (Ax), 0.25% carboxymethyl cellulose (CMC) and 0.1% a non-odorized detergent (i.e. mixture of hydrated alkaline-metals salts and aliphatic carboxylic acids, hereafter MSJ) and their mobility in porous medium was also studied.

### 4.2.1 Stability of NANOFER STAR

*PAA has the highest potential to stabilize NANOFER STAR, as it significantly shifts the zeta potential of particles to more negative values without changing particle size distribution.*

**Experimental protocol** PAA-, EMG- and TER-modified suspensions were characterized in terms of

- (i) Fe(0) content (measured in suspensions as delivered by the producer via H<sub>2</sub> production after acid digestion)
- (ii) zeta potential (measured in suspension with particle concentration of 200 mg/L using ZetaSizer Nano)
- (iii) sedimentation rate (measured in suspension with particle concentration of 1 g/L using a TurbiScan LAB) and
- (iv) particle size, including:
  - volume-based geometric radius (measured in suspension with particle concentration of 200 mg/L using EyeTech™)
  - volume-based equivalent spherical diameter (measured using Mastersizer 2000 in a suspension with particle concentration of 1 g/L, which was during the measurement diluted by the instrument to ca. 100 mg/L)
  - hydrodynamic radius (using ZetaSizer Nano).

**Results** Properties of the NANOFER STAR particles in PAA-, EMG- and TER-modified suspensions are shown in Table 3. For comparison, the properties of activated and inactivated NANOFER STAR in unmodified suspensions are also included. Except for PAA-stabilized NANOFER STAR, the particle size distribution was significantly changed in modified suspensions compared to inactivated NANOFER STAR (Table 3). Sedimentation rates for NANOFER STAR in modified suspensions and that of activated

NANOFER STAR were fairly similar, ranging from 118 to 154 mm/h, but higher than these of inactivated NANOFER STAR.

The best improvement of zeta potential was achieved by modifying particle suspension with PAA (zeta potential changed from -21 mV in inactivated NANOFER STAR to -60 mV in PAA-modified NANOFER STAR, Table 3). With the exception of CMC-modified suspension, where the particle's zeta potential also significantly shifted to more negative (-40 mV), other modified suspensions and activation NANOFER STAR did not significantly improve zeta potential compared to inactivated NANOFER STAR particles.

**Table 3:** Properties of NANOFER STAR particles in modified suspensions. PSD: particle size distribution.

NANOFER STAR	PSD <sup>1</sup> [d <sub>10</sub> / d <sub>50</sub> / d <sub>90</sub> ] [μm]	PSD <sup>2</sup> [d <sub>10</sub> /d <sub>50</sub> /d <sub>90</sub> ] [μm]	Hydrodynamic radius [μm]	Zeta potential [mV]	Sedimentation rate [mm/h]	Fe(0) [%]
NANOFER STAR in 0.1% CMC (batch #224)	1.6/3.3/4.9	1.1/2.5/8.2	2.4 ± 0.2	-40 ± 1	118	14–16
NANOFER STAR in 3% PAA (batch #224)	0.8/1.6/2.0	0.8/3.0/7.1	2.1 ± 0.1	-60 ± 2	126	10–13
NANOFER STAR in 0.1% EMG (batch #197)	1.3/4.4/9.3	1.4/3.8/33.5	2.7 ± 0.2	-22 ± 2	119	11–15
NANOFER STAR in 0.5% TER (batch #197)	1.4/4.5/10.5	1.5/3.9/62.0	2.6 ± 0.2	-19 ± 2	154	11–15
NANOFER STAR in 2% TER (batch #197)	1.3/4.3/8.9	1.5/3.6/54.6	2.5 ± 0.1	-16 ± 2	136	11–15
Activated NANOFER STAR (batch #197)	1.1/3.84/8.6	1.3/3.1/19.5	n.a.	-15 ± 7	145	11–15
Inactivated NANOFER STAR (batch #224)	1.1/1.9/2.1	1.4/3.7/21.5	n.a.	-21 ± 5	67	13–16

<sup>1</sup>Measured using EyeTech™; <sup>2</sup>Measured using Mastersizer, n.a. not available. Batch numbers provided by the producer.

**In conclusion**, PAA has the highest potential to stabilize NANOFER STAR, as it (i) significantly shifts the zeta potential of particles to more negative values and (ii) does not change the particle size distribution (compared to original, inactivated NANOFER STAR).

PAA-stabilized NANOFER STAR was characterized in details in terms of zeta potential and particle size as a function of pH. PAA-stabilized NANOFER STAR had a zeta potential close to 0 mV from pH 3.5–6 and a negative zeta potential from pH 6–11.5 (reaching -40 mV at pH 11.5) (data not shown), being consistent with the  $pK_a$  of the acrylic carboxyl group of the PAA found in literature at  $6.0 \pm 0.5$  (Viota et al., 2005).

PAA-stabilized NANOFER STAR appeared to be polydispersed from pH 3.5–11.5. When the particles have neutral charges at the surface ( $pH < pK_a$  (PAA)), the size of the aggregates reached 1,400–2,100 nm (intensity mean). For  $pH > pK_a$  (PAA), the size of the aggregates decreases to 700–1,400 nm

(intensity mean). Once expressed as a function of the number mean, the size is constant between 40–90 nm independent on the pH (Figure 8).

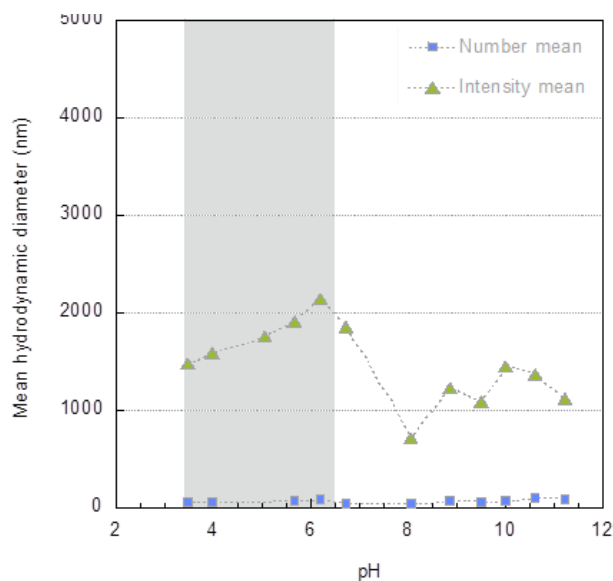


**Figure 8:** Evolution of the size (number and intensity mean) for PAA-stabilized NANOfer STAR suspension ( $c_{\text{particle}} = 10 \text{ mg/L}$ ) as a function of pH. Grey areas correspond to the pH range where the particles are neutrally charged.

The zeta potential and size of PAA-stabilized NANOfer STAR was also determined in the suspensions prepared in water with different hardness, F.I.s, F.I.m, F.I.h, and compared to that in ultrapure water. PAA-stabilized NANOfer STAR showed a size distribution of 140–160 nm (number mean) and 840–1,500 nm (volume mean) independent on the solution pH (Figure 9 left). Zeta potential of PAA-stabilized NANOfer STAR varied between -17 and -23 mV (Figure 9 right).

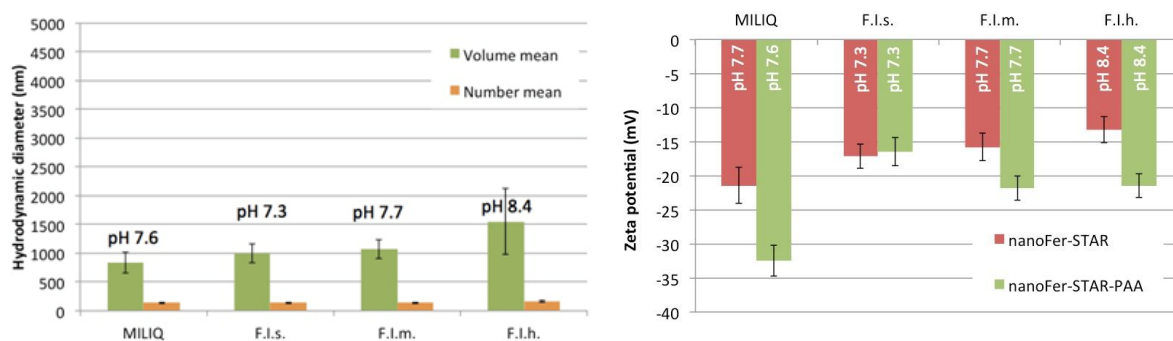


**Figure 9:** Average hydrodynamic diameter (left) and zeta potential (right) of PAA- NANOfer STAR suspensions prepared in different standardized water F.I.s, F.I.m, and F.I.h, measured in a 10 mg/L particle suspension at 25 °C. For comparison, data for ultrapure water (MILIQ) are also plotted.

#### 4.2.2 Mobility and Delivery of NANO FER STAR

*Mobility of PAA-stabilized NANO FER STAR is significantly improved (compared to immobile inactivated NANO FER STAR), with the max estimated transport distance of 1.3 m and 1.0 m in M.I and M.II porous medium, respectively. Mobility of NANO FER STAR decrease in the following order of added stabilizers: 3% PAA > 0.1% EMG = 0.5–2% TER and 3% Ax > 0.1% MSJ > 0.25% CMC.*

*Optimal delivery of NANO FER STAR was achieved when the suspension contained 10 g/L of both particle and CMC. The accomplished mobility of this suspension was comparable to that of NANO FER 25S; given that air-stable NANO FER STAR contains no additional surface coating (which may alter the reactivity of particles) and it is easier to handle, CMC-modified NANO FER STAR is preferentially recommended for field applications.*

**Experimental protocol** Mobility of EMG-, TER- and PAA-modified suspensions of NANO FER STAR particles was studied in D.I duplicate columns (i.d. 2.5 cm, 10 cm saturated packed bed length) filled with the standardized porous media M.I and M.II with EPA soft water (F.I.s) as the background solution. The experiments were carried out at two injection velocities of ca. 10m/d and ca. 100 m/d. The stabilizer-containing suspensions were diluted with F.I.s up to initial particle concentration of ca. 1 g/L. Column effluents were collected and analyzed for  $Fe_{tot}$  content (ICP-OES), used for the evaluation of the particle breakthrough.

Mobility of Ax-, CMC- and MSJ-modified suspensions of NANO FER STAR particles ( $c_{particle} = 10$  g/L) was studied in D.I columns (i.d. 2.0 cm, 22 cm saturated packed bed length) filled with commercial quartz sand (grain size 0.5–2 mm, 99.8% quartz,  $n_e = 39\%$ ,  $k_f = 1 \times 10^{-3}$  m/s) and deoxygenated tap water as the background solution. The experiments were carried out at the injection velocities of ca. 100 m/d. Evaluation of particle mobility was done by means of  $Fe_{tot}$  measurements in the column effluents (ICP-OES).

Mobility of CMC-modified suspensions of NANO FER STAR particles ( $c_{particle} = 10$  g/L as  $Fe_{tot}$ ) or suspension of activated NANO FER STAR was additionally studied in D.II column (i.d. 2.0 cm, 200 cm saturated packed bed length) filled either with 0.5–1 mm fraction of the above described commercial quartz sand (washed prior to the loading into the column) or M.II porous medium and with deoxygenated tap water as the background solution. The experiments were carried out at the injection velocities of ca. 100 m/d (for commercial quartz sand) and 300 m/d and 10 m/d for M.II porous medium. Particle breakthrough was estimated on the base of magnetic susceptibility measurements, i.e. delta frequency of magnetic susceptibility (difference between the measured frequency on the column with and without NANO FER STAR particles). There is a linear dependence between the frequency and the Fe content, allowing using delta frequency as proxy for  $Fe_{tot}$ - and therefore particle content. Magnetic susceptibility was measured along the whole length of the column, allowing the time-evolved evaluation of the particle content in particular zones of the column.

The effect of biofilm on the mobility of activated NANO FER STAR particles was tested in D.I columns (i.d. 2.5 cm, 20 cm saturated packed bed length) filled with M.II porous medium onto which a biofilm was grown. NANO FER STAR particles in a suspension containing 50 mg/L  $Fe_{tot}$  were injected at  $v_{eff} = 10$  m/d into the column, after which the column was flushed with F.I.m fluid, serving as the background solution. Column effluents were collected and analyzed for  $Fe_{tot}$  (ICP-OES), which served as a

proxy for the particle content. A control column experiment without biofilm grown on M.II porous medium was run in parallel.

Radial migration of CMC-modified NANOFER STAR particles and thus delivery of the particles into porous medium was studied in cascading column experiments filled with M.II porous medium. Cascading column experiments were carried out under the same conditions as for CMC-stabilized NANOFER 25S particles (see Section 4.1.2). Particle suspension with  $c_{\text{particle}} = 5$  or 10 g/L and 0, 5, 8, or 10 g/L CMC were injected under flow velocity of  $15.19 \text{ m/d} < v_{\text{eff}} < 100 \text{ m/d}$ . Magnetic susceptibility data were used to monitor the transport and distribution of CMC-modified NANOFER STAR particles. Detailed information on the set of cascading column experiments, including the column dimensions, flow rates and pressure changes is included in Table A2 in Appendix.

**Results** No breakthrough was observed for NANOFER STAR in suspension containing 0.1% EMG, 0.1% EMG, 0.5% TER and 2% TER and for activated NANOFER STAR in both porous media M.I and M.II and under both injection velocities applied (10 m/d and 100 m/d). Also for PAA-stabilized NANOFER STAR suspension no breakthrough in M.II was observed under  $v_{\text{eff}} = 10 \text{ m/d}$ , while in M.I the breakthrough was very low ( $c/c_0$  of ca. 0.03, data not shown). By increasing the injection velocity to 100 m/d, the particle breakthrough in porous medium M.I increased to ca.  $c/c_0 = 0.6$ , Figure 10a) while in porous medium M.II the breakthrough reached ca.  $c/c_0 = 0.5$ , Figure 10b).

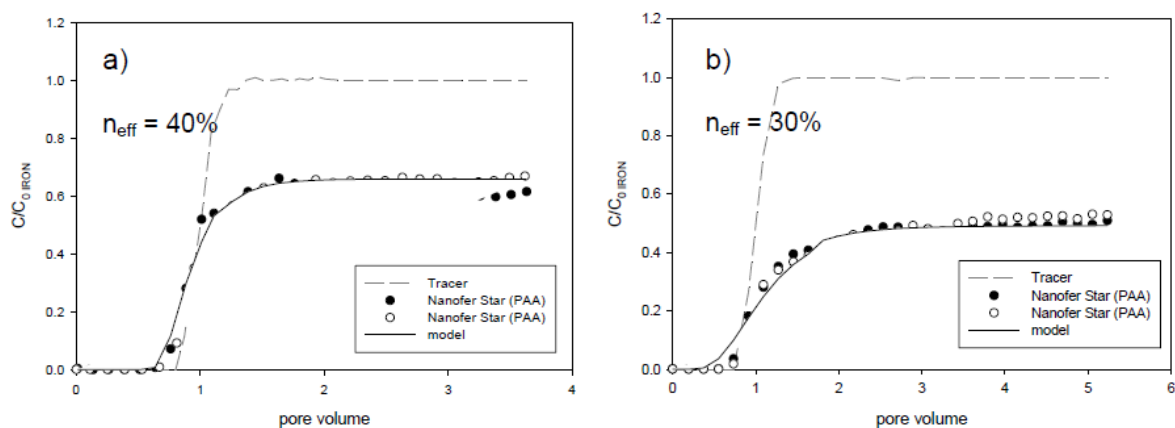


**Figure 10:** Duplicate experimental breakthrough curves (depicted as hollow and full cycles) for PAA-stabilized NANOFER STAR suspension (measured as  $\text{Fe}_{\text{tot}}$ ) in porous media M.I (a) and M.II (b).  $C_0, \text{particle} = 1 \text{ g/L}$ ;  $v_{\text{eff}} = 100 \text{ m/d}$ . Solid curves are mean values of the model generated by CXTFIT, STANMOD software, version 2.08.1130 by fitting the convection-dispersion equation to the experimental breakthrough curve.  $n_e$  is effective porosity.

The calculated maximum travel distance (corresponding to 99.9% of particle removal) according to the physicochemical filtration was 1.35 m in M.I and ca. 1.00 m in M.II (Table 4), which is a significant improvement compared to practically immobile inactivated NANOFER STAR particles.

**Table 4:** Mobility parameters for NANOFER STAR particles in suspension stabilized with 3% PAA.

NPs	C <sub>0</sub> (NP) [g/L]	Porous media (PM)	n <sub>e</sub> [%]	Fluid	V <sub>eff</sub> [m/d]	k [1/s]	α [-]	L <sub>T</sub> (50%) [m]	L <sub>T</sub> (63%) [m]	L <sub>T</sub> (99.9%) [m]
NANOFER STAR in 3% PAA	1	M.I (Dorsilit®)	40	F.I.s	100	5E-3	0.442	0.14	0.19	1.35
NANOFER STAR in 3% PAA	1	M.II (VEGAS)	30	F.I.s	100	8E-3	0.621	0.10	0.14	1.00

As to Ax-, CMC- and MSJ-modified suspensions of NANOFER STAR particles, their mobility decreased in following order: Ax-modified NANOFER STAR modified > MJS-modified NANOFER STAR > CMC-modified NANOFER STAR (the latter being practically immobile) (Figure 11).

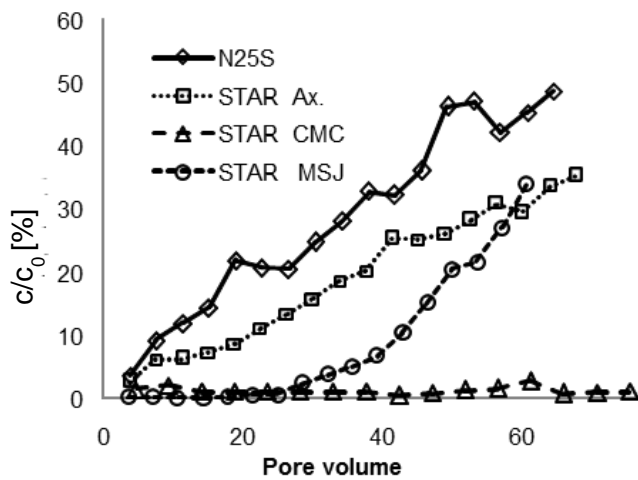


**Figure 11:** Breakthrough curves of modified NANOFER STAR. For comparison, the data for NanoRem standard NP, NANOFER 25S (N25S) are also plotted. (C<sub>0, particle</sub> = 10 g/L as Fe(0); v<sub>eff</sub> = 100 m/d).

Low mobility of CMC-modified NANOFER STAR was also confirmed in D.II column experiments. CMC-modified NANOFER STAR did show superior mobility compared to the initial inactivated NANOFER STAR (based on delta frequency data, Figure 12), but the stabilization of NANOFER STAR with CMC still did not appear to be more efficient than the activation of NANOFER STAR with respect to particle mobility. From Figure 12 it was obvious that activated NANOFER STAR travelled longer distances and was more homogeneously distributed along the column compared to CMC-modified and inactivated NANOFER STAR.



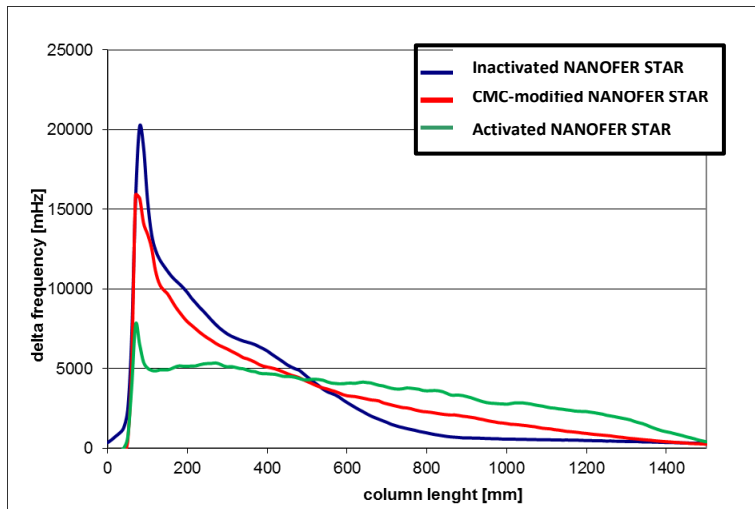


**Figure 12:** Delta frequency along the column length for activated NANO FER STAR and CMC-modified NANO FER STAR ca. 2 h from the beginning of the injection into a commercial quartz sand.  $v_{eff} = 100$  m/d. For comparison, data frequency for inactivated NANO FER STAR is also included.

The results of D.II column experiments also demonstrated a negligible mobility of activated NANO FER STAR through M.II porous medium at lower flow velocity ( $v_{eff} = 10$  m/d) compared to the injection conditions ( $v_{eff} = 300$  m/d), where the particles were detected 120 cm from the injection point, ca. 5 h after the injection (Figure 13).

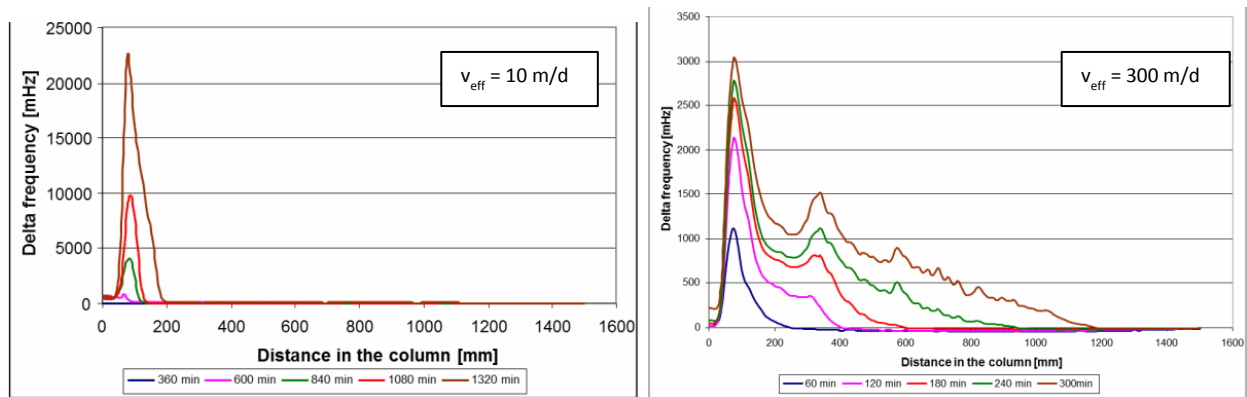


**Figure 13:** Delta frequency as a proxy for particle content along the column length during the course of the activated NANO FER STAR injection into M.II porous medium at low (10 m/d) flow velocity (left) and high (300 m/d) flow velocity (right).

Presence of biofilm grown onto porous medium M.II did not influence breakthrough of activated NANO FER STAR, which remained very low, with  $c/c_0 < 1\%$  (data not shown).

Results of the cascading column experiments revealed that NANO FER STAR suspension modified with 5 g/L CMC reached a good delivery of  $< 0.5$  m. By increasing the CMC content to 10 g/L an optimal particle delivery to 0.5–0.6 m from the injection point was achieved (data not shown), being comparable to that of CMC-modified NANO FER 25S (see Section 4.1.2). The delivery of CMC-modified NANO FER STAR suspension was significantly improved compared to that of unmodified NANO FER STAR suspensions, which were practically immobile, independently of the applied flow velocity.

Details on the particle travel distance depending on the experimental setup are included in Table A2 in Appendix.

Given the comparable delivery of CMC-stabilized NANOFE STAR and NANOFE 25S, particles, the former are preferentially recommended for field applications, as they are easy to handle and their surfaces are not coated with an additional polymer which may alter the reactivity of particles.

#### 4.2.3 Fate of NANOFE STAR under field relevant conditions

*Activation and CMC-modification of NANOFE STAR decreases its reactivity towards PCE. Transformation products of anaerobic corrosion of activated NANOFE STAR are minerals that are commonly found in sediment and soils, i.e. Fe oxides, Fe hydroxides and Fe carbonates. After one month of NANOFE STAR reaction with anaerobic contaminated groundwater from Spolchemie I field site, CZ, ca.12% of the initial Fe(0) remain unconsumed (batch experiment). In the field sample from the Spolchemie I field site, CZ, ca. 30% of the initial Fe(0) remain unconsumed 5 months after the injection.*

The following aspects of fate for optimized NANOFE STAR under field relevant conditions were studied:

- **Long term reactivity** of activated- and CMC-modified NANOFE STAR with respect to PCE (batch reactor, experiment duration: 1 month)
- **Long term anaerobic corrosion** and **Fe speciation** for activated NANOFE STAR in contact with groundwater from the Spolchemie I, CZ field site, contaminated with chlorinated hydrocarbons (batch reactor, experiment duration: 1 month)

**Experimental protocol** Reactivity of activated NANOFE STAR and CMC-modified activated NANOFE STAR with respect to PCE was compared in anoxic batch reactors containing  $c_{\text{particle}} = 1 \text{ g/L}$  as  $\text{Fe}_{\text{tot}}$  (in F.I.m fluid) and 50 ppm PCE. The experiment duration was one month. The activation of NANOFE STAR was performed for 48 h either at room temperature or in a refrigerator. Formation of the final degradation products ethane, ethene and ethyne was monitored by GC. For comparison, the experiment with inactivated NANOFE STAR was also carried out.

Anaerobic corrosion and Fe speciation for activated NANOFE STAR was studied for one month in anaerobic batch reactors in which the particle suspension was diluted with groundwater from Spolchemie I, CZ field site to a  $c_{\text{particle}} = 0.4\text{--}1.6 \text{ g/L}$  (as  $\text{Fe}_{\text{tot}}$ ). The groundwater from the field site was polluted with ca. 10 mg/L of chlorinated hydrocarbons. After one month, solid particles were extracted under inert atmosphere (in a glove box) and analysed by means of XRD, low-temperature  $^{57}\text{Fe}$  Mössbauer spectroscopy and TEM. The results were compared with the samples collected from monitoring wells at Spolchemie I, CZ field site, where activated NANOFE STAR was injected.

**Results (reactivity of NANOFE STAR)** In contact with inactivated NANOFE STAR and after ca. one month of the reaction time, PCE anaerobically degraded to final degradation products: ethene (dominated), ethane and ethyne (Figure 14 left). The specific surface area normalized reaction rate constant ( $k_{\text{SA}}$ ) for this reaction was calculated as  $1.79 \times 10^{-5} \text{ L/h/m}^2$ . Proportion of degraded PCE (which corresponded to ethene-, ethane- and ethyne formation) amounted to ca. 23, 17 and 14% of the initial PCE for inactivated NANOFE STAR, activated NANOFE STAR at room temperature and acti-

vated NANOFEER STAR in a refrigerator, respectively (Figure 14 right). CMC-modification of activated NANOFEER STAR exhibited adverse effects on particle reactivity (data not shown).

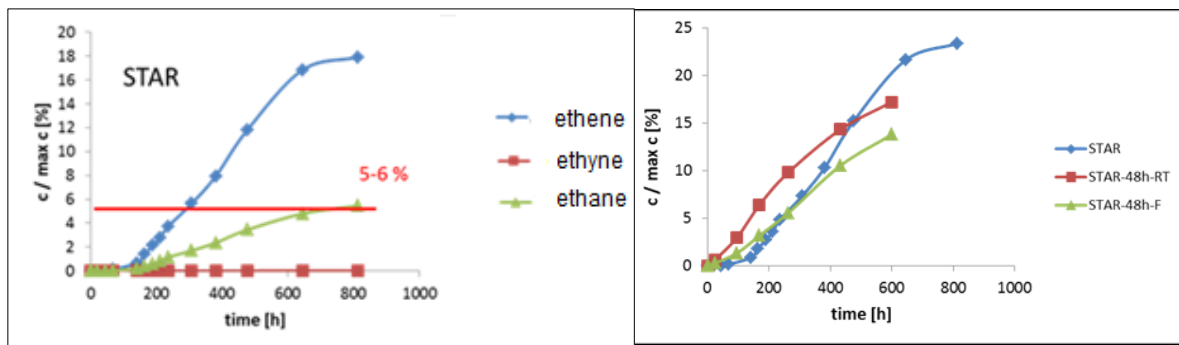


**Figure 14:** Formation of ethene, ethane and ethyne in the course of PCE degradation (left) and proportion of degraded PCE with inactivated NANOFEER STAR (blue line), activated NANOFEER STAR at room temperature (red line) and activated NANOFEER STAR in a refrigerator (green line) (right).

**In conclusion**, surface activation and/or CMC-modification decrease the reactivity of NANOFEER STAR, compared to its inactivated particles.

**Results (Anaerobic corrosion and Fe speciation for NANOFEER STAR)** Inactivated NANOFEER STAR is composed of a metallic-iron core ( $\alpha$ -Fe) and a ca. 4 nm thin Fe oxide shell (Figure 15, left). After the activation process (for details please see DL 2.2 “Assessment of Nanoparticle Performance for Removal of Contaminants - nZVI Particles”) the content of  $\alpha$ -Fe remains high (> 95 wt.%) (Figure 15, right).

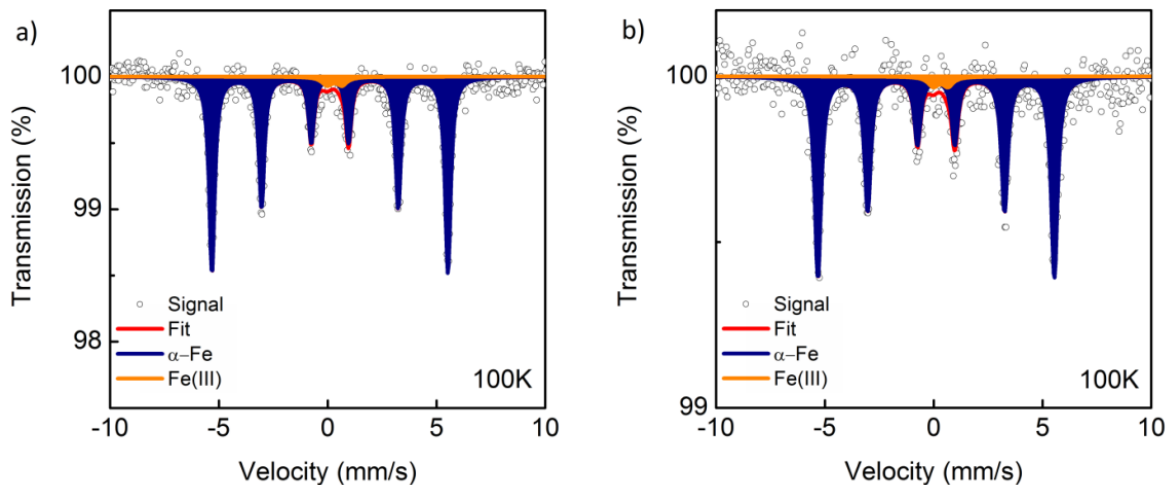


**Figure 15:** Mössbauer spectra of inactivated (left) and (for 48 h) activated NANOFEER STAR.

Activated NANOFEER STAR corrodes fast on anoxic groundwater from Spolchemie I, CZ field site. 88.5% of Fe (0) was transformed to mainly green rust, (fougerite  $[\text{Fe}^{2+}_4\text{Fe}^{3+}_2(\text{OH})_{12}][\text{CO}_3]\cdot 3\text{H}_2\text{O}$ ), chukanovite ( $\text{Fe}^{2+}_2(\text{OH})_2\text{CO}_3$ ), siderite and ferric oxides/oxyhydroxides) within 1 month (Figure 16). Nevertheless, there was 11.5% of Fe(0) within NANOFEER STAR remaining after 1 month of the experiment duration.

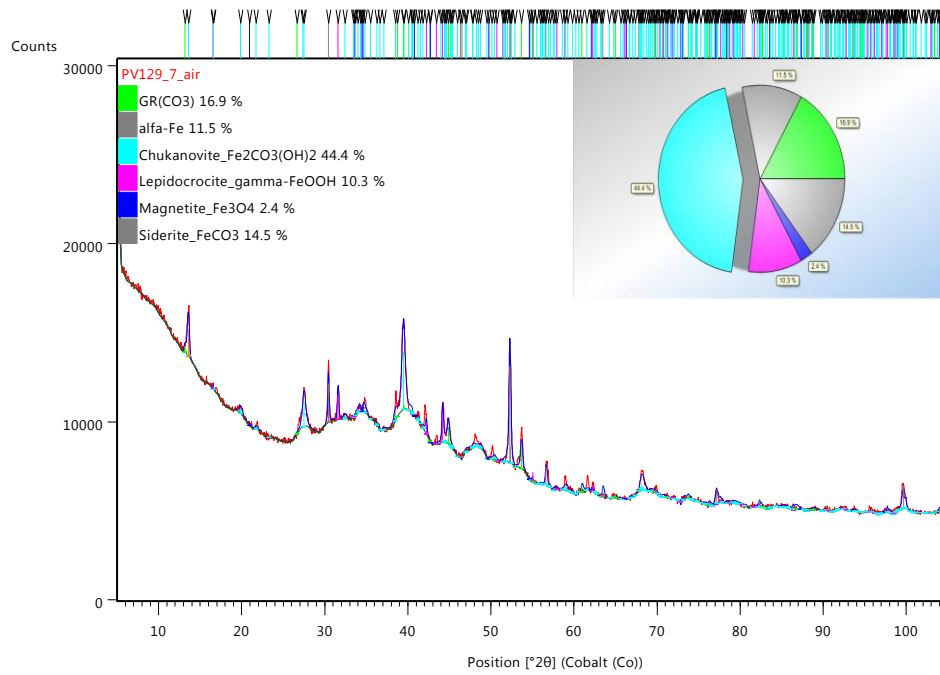


**Figure 16:** XRD pattern of activated NANOFeR STAR after being in contact with anoxic groundwater from Spolchemie I, CZ field site for one month. GR = green rust.

This observation was in good accordance with the outcomes of measurements carried out on samples collected from monitoring wells at Spolchemie I, CZ field site (Figure 17), where the same particles, activated NANOFeR STAR were injected. Nevertheless, the reaction kinetics in the batch experiment and in the field significantly differed. In the field, Fe(0) content decreased to 30 wt.% of its initial value after 5 months of reaction time, but the main reaction product was green rust, as it was in the batch reactor (Figure 16). The presence of carbon in several phases could originate from non-complete elimination of air or reaction with chlorinated hydrocarbons.

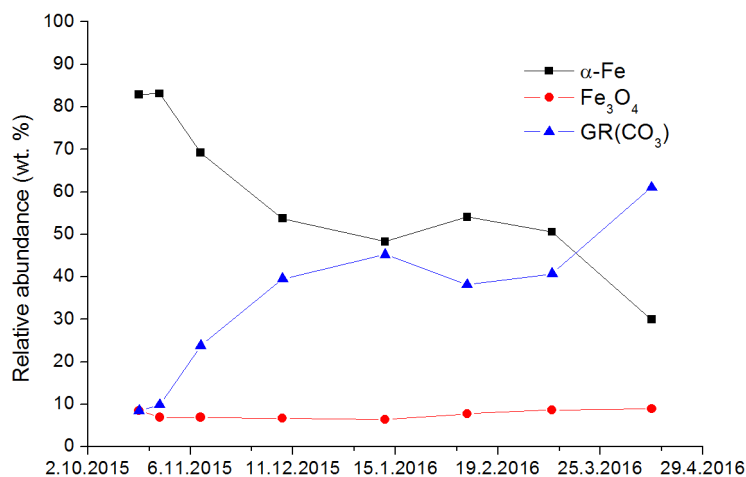


**Figure 17:** Changes over time in content of  $\alpha$ -Fe,  $\text{Fe}_3\text{O}_4$  and green rust (GR) (as determined by XRD) in a groundwater sample from Spolchemie I, CZ field site (well PV130), where activated NANOFE STAR was injected.

**In conclusion,** transformation products of anaerobic corrosion of activated NANOFE STAR are minerals, commonly found in sediment and soils, i.e. Fe oxides, Fe hydroxides and Fe carbonates. Batch experiments with activated NANOFE STAR successfully simulated transformation of NANOFE STAR particles at the contaminated field site.

### 4.3 Radiolabelled NANOFE STAR

Responsible partner: [NMBU](#)

Contributor: BRGM

Radiolabelling of NPs is one way to study NP behaviour in complex environmental matrices. Pristine NPs can be neutron activated, with minimum surface modification or changes in chemical properties (Oughton et al., 2008). Neutron activated NPs can readily be detected and quantified by gamma spectrometry without destruction of the sample matrix.

Radiolabelled NPs are produced by neutron activation of NANOFE STAR (NANO IRON s.r.o.) at a flux of 1,012 neutrons/cm/s for 24 h, in the reactor at the Institute of Energy Technology (Kjeller, Norway). After a cool-down period of 10 days, the specific activity of irradiated NPs was determined by gamma spectrometry using a Ge-detector (Canberra, Meriden, CT, USA) targeting their respective specific gamma energies (Fe-59, 1.099 MeV). The specific activity was 10 KBq/mg.

Radiolabelled NANOFE STAR were not aimed to be injected at a field site within NanoRem, but their transport behaviour was studied under field relevant conditions (in a heterogeneous porous medium with a grown biofilm), in order to evaluate the utilization of the NP radiolabelling in predicting the mobility of NPs.

#### 4.3.1 Mobility of radiolabelled NANOFE STAR

*Radiolabelled NANOFE STAR particles are not mobile in heterogeneous porous medium with a grown biofilm.*

**Experimental protocol** A mixture of 2 mg of radiolabelled NANOFER STAR and 1 g of pristine NANOFER STAR was used to prepare a particle suspension in F.I.s standard water. Mobility of this suspension ( $c_{\text{particle}} = 1 \text{ g/L}$ ) was studied in D.I column (2.5 cm i.d., 20 cm saturated packed bed length) filled with VEGAS PM (M.II) in which a biofilm had been grown for two months. Standard water F.I.s served as background electrolyte. The mobility test was carried out under the flow velocity ca. 10 m/d. Particle transport was evaluated on the basis of gamma radiation activity (Gamma counter, 1480 Wizard 3) and  $\text{Fe}_{\text{tot}}$  (ICP-MS, 8800) measurements in column effluents. After the column experiment was terminated, the column was disassembled and cut into ten 2 cm-segments, which were examined for Fe-59 activity.

**Results** Absence of radiolabelled NANOFER STAR breakthrough under the experimental conditions applied was found both by Fe-59 activity and  $\text{Fe}_{\text{tot}}$  content in the collected effluents. Both Fe-59 activity and  $\text{Fe}_{\text{tot}}$  data were very low, being 0–2.7 cpm and  $6 \times 10^{-7}$ – $6 \times 10^{-5} \text{ g/L}$ , respectively (data not shown).

It was visually observed that the injected NPs deposited in the porous medium within the first 2 cm from the injection port. In order to locate radiolabelled NANOFER STAR Fe-59 activity was measured in the column segments after the termination of the column experiment. The results showed Fe-59 activity only in the first 2 cm of the column (Figure 18) confirming that radiolabelled NANOFER STAR was filtered out and was not mobile in the porous medium with the grown biofilm under the applied experimental conditions. These results confirmed the possibility of using radiolabelled NPs to study the transport behaviour of NPs.

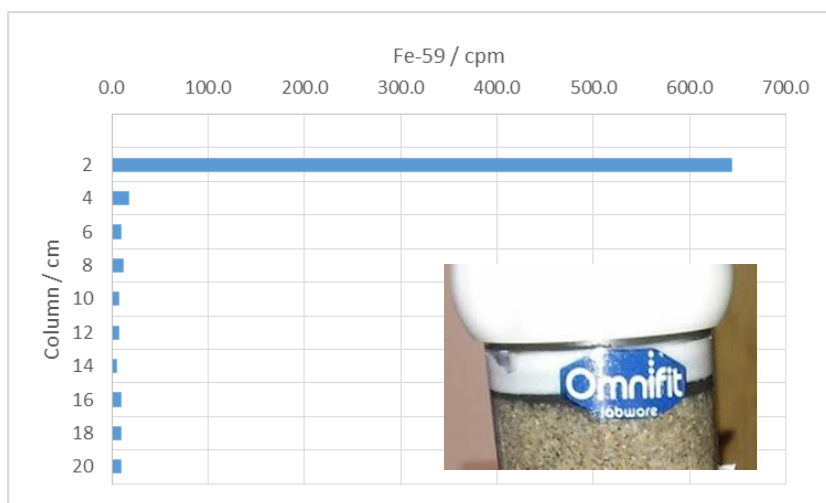


**Figure 18:** Gamma activity distribution in counts per minute (cpm) along the column length. Insert: Segment of the examined column.

#### 4.4 Milled ZVI (FerMEG12, UVR-FIA GmbH)

Responsible partner: UNIVIE

Contributors: CNRS-CEREGE, USTUTT

Milled ZVI particles (FerMEG12, UVR-FIA GmbH, Germany) have a flake shape with the lateral size of the flake of several  $\mu\text{m}$  and the flake thickness  $< 100$  nm (Figure 19). Milled ZVI particles have a BET specific surface area of  $18 \text{ m}^2/\text{g}$  and an average  $\text{Fe}^0$  mass content of 85% (Köber et al., 2014).

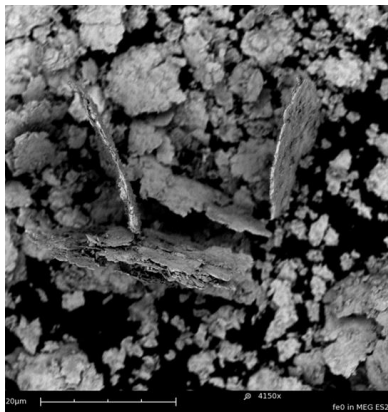


**Figure 19:** SEM image of milled ZVI particles. Source: UVR-FIA GmbH.

Optimization of milled ZVI particles was carried out in terms of stability of the particle suspension, applying five different polymers (agar agar, guar gum, gum arabic, CMC and starch), among which agar agar was selected as the best performing one. Stability, mobility and reactivity (in a batch reactor) are here reported for both aqueous and agar agar-stabilized suspensions of milled ZVI particles, while the reactivity in a column reactor as well as the long-term fate was studied for the non-stabilized milled ZVI only, as applied at the Solvay field site, CH.

##### 4.4.1 Stability of milled ZVI (FerMEG12) suspension

*Milled ZVI particles are unstable in aqueous suspension. Agar agar (1 g/L) stabilizes the particle suspension.*

**Experimental protocol** Suspension of milled ZVI particles ( $C_{\text{particle}} = 1 \text{ g/L}$ ) was prepared in (i) ultrapure water (Millipore, Elix®5-Milli-Q® Gradient A10) and (ii) 1 g/L agar agar solution in ultrapure water (for more details see Velimirovic et al., 2015).

Stability of milled ZVI suspension was determined via the sedimentation rate (Turbiscan LAB), as described in Laumann et al. (2013). Volume based average particle size ( $d_{50}$ ) in suspension ( $c_{\text{particle}} = 200 \text{ mg/L}$ ) was measured using the laser obscuration time (EyeTech™). Zeta potential was determined from the electrophoretic mobility of particles in a suspension ( $c_{\text{particle}} = 100 \text{ mg/L}$ ) using a laser Doppler velocimetry (ZetaSizer Nano ZS).

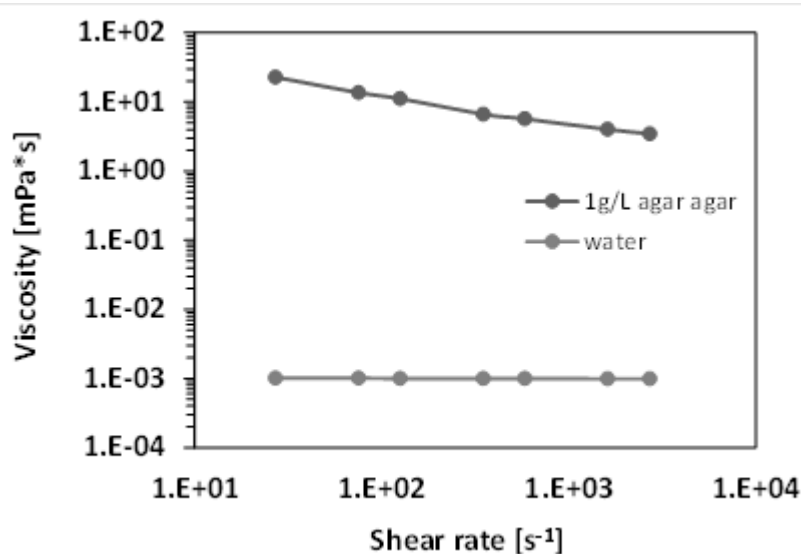
**Results** Sedimentation rate, average particle size and zeta potential of milled ZVI in pure aqueous and agar agar-stabilized suspensions are presented in Table 5.



**Table 5:** Stability parameters for milled ZVI in pure aqueous and agar agar-stabilized suspension.

Milled ZVI	Sedimentation rate [mm/min]	d <sub>50</sub> [μm]	Zeta potential [mV]
Pure aqueous suspension	18.6	11.8	-22 ± 5
Agar agar-stabilized suspension	Stable > 24 h	11.9	-33 ± 5

The best performing suspension stabilizer (agar agar) was able to significantly increase zeta potential of milled ZVI (becoming more negative) and lower the sedimentation rate, without altering the average particle size. It is suggested that this is due to the increased solution viscosity (Figure 20) and subsequently inhibited interactions between the particles and their sedimentation. The performance of the remaining 4 stabilizers is reported in Velimirovic et al. (2015).

**Figure 20:** Viscosity as a function of shear rate for water and 1 g/L of agar agar solution.

#### 4.4.2 Mobility of milled ZVI (FerMEG12)

*Aqueous suspension of milled ZVI is immobile in heterogeneous PM (D.I columns, injection condition). Agar agar-stabilization significantly improved the mobility of milled ZVI, with the predicted travel distance for 50% of particle removal  $L_{T50} > 3$  m. The predicted transport distances for viscous agar agar-stabilized milled ZVI suspensions in different porous media strongly depend on the grain size distribution of the collector.*

**Experimental protocol** Mobility of milled ZVI was studied in D.I duplicate columns (2.5 cm i.d., 22 cm saturated packed bed length, following the Experimental Protocols) filled with the following porous media (PM): (i) Dorsilit® PM (M.I), (ii) VEGAS PM (M.II), (iii) PM from Spolchemie I field site, CZ and (iv) PM from Solvay field site, CH. In order to obtain a similar size fraction for all, the 0.25–4 mm size fraction from the two field sites was used. Selected characteristics of the PM are presented in Table 6. More detailed characterisation of PM can be found in Velimirovic et al (2015). F.I.s served as a background electrolyte in all experiments. The pressure drop along one of the duplicate columns was

continuously recorded by a pressure device (TP 704 10GB; Delta Ohm HD 2124.2) connected to the column inlet and outlet. All the column tests were carried out under the injection velocity of ca. 100 m/d). Evaluation of the particle breakthrough was based on the  $Fe_{tot}$  content in the column effluents (after acid digestion) (measured by ICP-OES).

**Table 6:** Selected characteristics of PM used in column experiments.

	Dorsilit® PM (M.I)	VEGAS PM (M.II)	PM from Spolchemie I field site, CZ	PM from Solvay field site, CH
$d_{50}$ [mm]	0.65	0.48	0.80	0.48
$n_e$ [%]	39.7	29.8	26.2	27.4
Sorting <sup>a</sup>	Moderately good	Poor	Poor	Poor
TOC [%] <sup>b</sup>	< LoQ	0.056	0.042	n.d.
$\zeta$ [mV] <sup>c</sup>	$-22 \pm 4$	$-22 \pm 3$	$-18 \pm 2$	$-21 \pm 3$
SiO <sub>2</sub> [%]	98.50	84.16	69.78	49.06
Al <sub>2</sub> O <sub>3</sub> [%]	0.47	5.46	10.82	3.54
Fe <sub>2</sub> O <sub>3</sub> [%]	0.18	0.88	5.72	1.64
CaCO <sub>3</sub> [%]	0.04	4.85	3.83	36.64
MgCO <sub>3</sub> [%]	0.02	0.89	2.63	6.88

<sup>a</sup> Sorting of porous media calculated after Folk and Ward (1957).

<sup>b</sup> Total organic carbon (TOC) determined with a LECO RC-612 Carbon analyzer (St. Joseph, MI, USA) equipped with a solid-state infrared detector after Micić et al. (2013); LoQ = 0.005%.

<sup>c</sup> Calculated from the streaming potential (SurPASS, Anton Paar, Austria).

**Results** In aqueous suspension milled ZVI deposits within the first few centimetres in all PM, being practically immobile under the experimental conditions applied. Conversely, the agar agar-stabilized milled ZVI showed considerably higher elutability with the particle breakthrough reaching a plateau at  $c/c_0 = 0.84\text{--}0.97$  after only 3–7 pore volumes (Figure 21). The significantly slower breakthrough of agar agar compared to that of Br<sup>-</sup> tracer can be attributed to high fluid viscosity of agar agar (Figure 20) which is also expected for the agar agar-stabilized milled ZVI suspension.

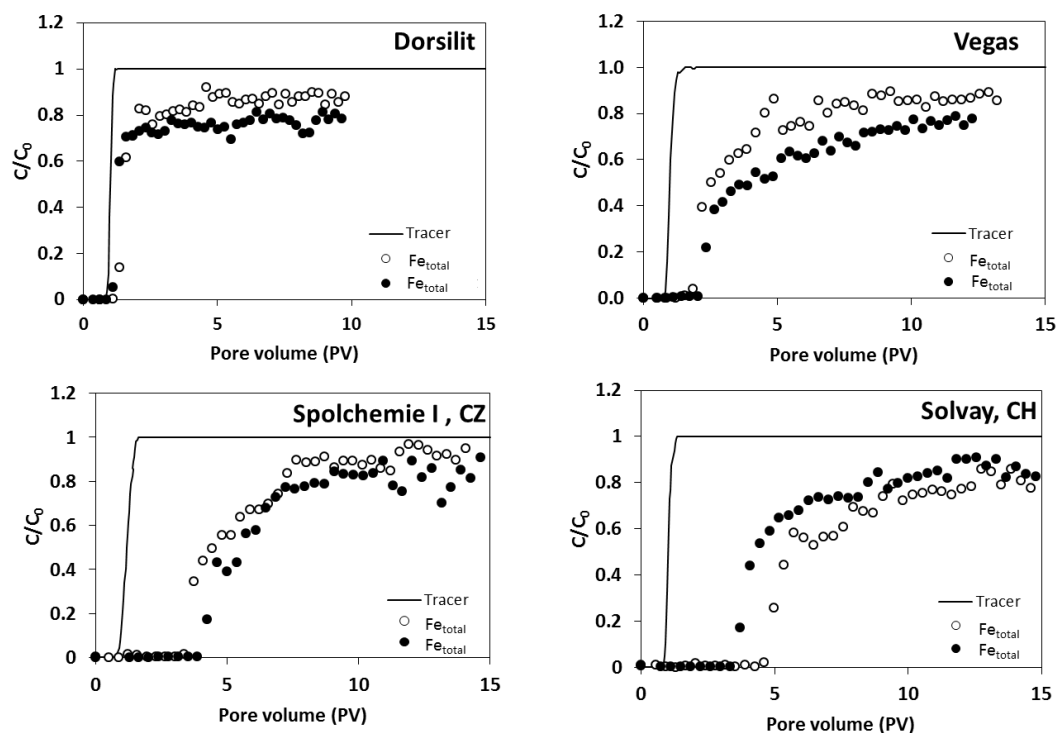


**Figure 21:** Duplicate breakthrough curves (hollow and full cycles) for agar agar-stabilized milled ZVI ( $C_0$ , particles: ca. 1 g/L in 1 g/L agar agar;  $v_{eff} = a.$  100 m/d). Solid line depicts the breakthrough of a  $Br^-$  tracer.

There was a slower increase of  $c/c_0$  in columns filled with VEGAS PM and PM from the two field sites. This may be due to (i) deposition of milled ZVI particles followed by (ii) blocking of the particles that approached afterwards by the previously deposited ones. Blocking was recorded in the average pressure data; significantly higher pressures (up to 1.7 bar) were observed in VEGAS PM and PM from field sites while in Dorsilit® PM where no blocking was suggested the pressure was much lower (ca. 150 mbar, data not shown). The breakthrough curves in Dorsilit® PM reached plateau fast and exhibited steady-state behaviour.

No correlation between the apparent breakthrough of agar agar-stabilized milled ZVI particles and the chemical composition of the investigated heterogeneous porous media was observed (data not shown). A favourable correlation was found between the median ( $d_{50}$ ) grain size of the porous media and the apparent breakthrough of agar agar-stabilized milled ZVI particles ( $R^2$  0.71), suggesting that the mobility of these viscous particle suspension largely depends on the collector grain size.

Predicting mobility parameters for agar agar-stabilized milled ZVI by means of CFT can only be semi-quantitative, given that the milled ZVI particles are not spherical (Figure 19) and therefore the particle diameter applied in calculations is not accurate. The predicted transport distances for PM studied decreased in the following order: Spolchemie I, CZ > Solvay, CH > Dorsilit® PM (M.I) > VEGAS PM (M.II) (Table 7). The estimated travel distances were significantly greater than 1 m reported by Köber et al. (2014) using non-stabilized milled ZVI suspensions. There was a remarkably good correlation ( $R^2$  0.90) between the median grain size ( $d_{50}$ ) of the investigated PM and the max particle removal (data not shown).

**In conclusion**, the results showed that the collector grain size appears to have the largest influence on the transport behaviour of viscous, agar agar-stabilized suspension of milled ZVI particles.

**Table 7:** Mobility parameters for agar agar-stabilized milled ZVI.

NPs	C <sub>0</sub> (NP) [g/L]	Porous media (PM)	n <sub>e</sub> [%]	Fluid	V <sub>eff</sub> [m/d]	k [1/s]	α [-]	L <sub>T</sub> (50%) [m]	L <sub>T</sub> (63%) [m]	L <sub>T</sub> (99.9%) [m]
Milled ZVI	1	M.I (Dor- silit®)	39.7	F.I.s	100	7E-4	2.3E-3	1.2	1.7	11.9
Milled ZVI	1	M.II (VE- GAS)	29.8	F.I.s	100	9E-4	4.8E-3	0.9	1.3	8.9
Milled ZVI	1	Spol- chemie I, CZ	26.2	F.I.s	100	4E-4	3.2E-3	3.2	4.6	32.2
Milled ZVI	1	Solvay, CH	27.4	F.I.s	100	7E-4	2.4E-4	1.2	1.8	12.2

#### 4.4.3 Fate of milled ZVI (FerMEG12) under field relevant conditions

The following aspects of fate of milled ZVI under field relevant conditions were studied:

- Particle **reactivity** (reaction rate **with respect to TCE**), particle **lifetime** and **Fe speciation** at particle surfaces under the conditions corresponding to the two field sites, Solvay, CH and Balassagyarmat, HU. The impact of agar agar stabilizer on the reaction kinetics of milled ZVI particles is also evaluated. Test duration 105 days.
- Particle **reactivity and anaerobic corrosion with respect to** contaminant at the Solvay, CH field site, a **PCE NAPL** in the more field-site realistic column reactors. Test duration 56 days.

*While the particle lifetime was in the same order of magnitude, dehalogenation of TCE by milled ZVI was somewhat faster for the Balassagyarmat, HU ( $k_{obs} = 6.9 \times 10^{-2} 1/d$ ), compared to the Solvay, CH field site conditions ( $k_{obs} = 3.5 \times 10^{-2} 1/d$ ) due to the higher  $SO_4^{2-}$  content for the former conditions. The major TCE degradation products (ethene and ethane) and the type of particle passivation appeared not to be site-specific. Presence of agar agar reduces the TCE dechlorination rate by an order of magnitude compared to that obtained using bare milled ZVI particles (batch reactors).*

*The major products of the PCE DNAPL degradation were TCE (intermediate) and ethene and ethane (final). The anaerobic corrosion accounted for 66% of the overall Fe(0) consumption during the PCE DNAPL degradation by milled ZVI (column reactors).*

**Experimental protocol in batch reactor** The evaluation of dehalogenation rate constant was carried out in batch reactors ( $c_{particle} = 1$  g/L, with/without 1 g/L of agar agar,  $c_{TCE} = 10$  mg/L of TCE, for more details see Velimirovic et al., 2015). All solutions and the particle suspension were prepared in anaerobic artificial groundwater (F.I.s). For the evaluation of dehalogenation rate constant under the experimental conditions closer to the Solvay, CH and Balassagyarmat, HU field sites, the batch reactor contained dried and sieved (< 2 mm) PM from either of the sites, 1 g of milled ZVI per kg of PM (as Fe(0), placed in a nylon membrane), 75 g of F.I.s and 5 mg/L of TCE in F.I.s. The TCE degradation was monitored via measuring the content of TCE and degradation products (ethene, ethane and ethyne)

by GC.  $H_2$  was sampled by a headspace sampler and analysed by a GC. pH, T, ORP and the selected solutes were monitored in an aliquot of the aqueous phase. The observed first order reaction rate constant ( $k_{obs}$ ) was calculated according to Johnson et al. (1996). The apparent anaerobic Fe(0) corrosion rate ( $R_{app}$ ) was determined by  $H_2$  production according to Liu and Lowry (2006). The lifetime of milled ZVI particles was then calculated dividing the Fe(0) content by  $R$ , assuming that milled ZVI is completely consumed in the reaction with groundwater (Velimirovic et al, 2014). After 7 and 105 days anaerobically dried samples of milled ZVI (from the batch reactors) were used for the Fe speciation analysis. The samples were examined by XRD and Fe K-edge XAS (ESRF, France) on the FAME beamline.

**Experimental protocol in column reactor** The reactivity of milled ZVI with respect to PCE NAPL was studied in a glass column reactor (i.d.: 3.6 cm, 200 cm saturated packed bed length) filled with M.I in which milled ZVI particles (13 g) and PCE NAPL (1 mL) were introduced, according to the Standardized Protocols. The initial amount of milled ZVI was ca. 6-fold stoichiometric amount, allowing a complete degradation of PCE to ethene as well as side reactions (such as anaerobic corrosion). Degassed tap water (F.II,  $c_{O_2}$ : 0.7–1 mg/L) was continuously injected into the column at a seepage velocity of ca. 0.5 m/d. At the column outflow a stainless steel valve was installed for monitoring the concentration of PCE and the degradation products. Gaseous reaction products and by-products ( $H_2$  formed via anaerobic corrosion) were collected in a gas trap and analysed via GC.  $Cl^-$  was measured in column effluents by potentiometric titration. Changes in Fe(0) content were tracked based on magnetic susceptibility measurements (Li et al., 2015).

**Results (batch reactor)** A summary of the kinetic data for dehalogenation of TCE by milled ZVI particles and agar agar-stabilized milled ZVI particles is shown in Table 8. The presence of agar agar reduced the TCE dechlorination rate by an order of magnitude compared to that obtained using bare milled ZVI particles (Table 8). The reduced dechlorination rate in the presence of agar agar and the similar corrosion rates observed for bare and agar agar-stabilized milled ZVI particles suggest that chemical or physical factors other than electron transfer control the reduction in TCE, as has been previously reported by Liu and Lowry (2006) for nZVI. The apparent corrosion rates presented in this study (9.3–9.7 mmol/kg/d) are significantly lower than those reported by Velimirovic et al. (2014) for nZVI particles (35–145 mmol/kg/d), indicating that milled ZVI particles are likely reactive longer than nZVIs, which may be advantageous for their *in situ* application.

**Table 8:** Summary of kinetic data for TCE dehalogenation under different conditions with calculated apparent corrosion rates for bare and agar agar-stabilized milled ZVI particles.

Type of particle	$K_{obs}$ [1/d]	$R_{app}$ [mmol/kg/d]	Lifetime [d]
Milled ZVI	$3.8 \times 10^{-2}$	9.3	1921
Agar agar-stabilized milled ZVI	$7.5 \times 10^{-3}$	9.7	1841
Milled ZVI in the presence of PM from Solvay field site, CH	$3.5 \times 10^{-2}$	98.2	182
Milled ZVI in the presence of PM from Balassagyarmat, HU field site	$6.9 \times 10^{-2}$	113.6	158

**In conclusion**, a lower reactivity for agar agar-stabilized ZVI is, however, not necessarily a drawback since the lower initial corrosion rate and consequent extended lifetime of agar-agar milled ZVI particles may in some cases be regarded as an advantage over the use of nZVI particles.

The kinetic data for milled ZVI under the field relevant conditions are also presented in Table 8. The faster degradation rate of TCE in the system with PM from Balassagyarmat, HU field site led to the higher corrosion rate and consequently somewhat shorter lifetime of milled ZVI particles. This can be explained by the 12-fold higher sulphate content in this reactor compared to the reactor with PM from the Solvay field site, CH (data not shown). According to Bi et al. (2009) the presence of sulphate can enhance the reactivity of Fe(0) by removing passivating Fe oxides and hydroxides from the Fe(0) surface and consequently increasing the number of reactive sites. However, the apparent corrosion rate and consequently the lifetime of milled ZVI particles are in the same order of magnitude for the geochemical conditions for both sites, implying that a similar fate of milled ZVI particles at these field sites is expected.

This was further confirmed by XRD analysis (Figure 22). The milled ZVI was initially composed of  $60 \pm 5\%$  Fe(0),  $35 \pm 5\%$  Fe carbide and  $5 \pm 5\%$  of magnetite/maghemite. 7 days after the incubation under the two different field site conditions, the mineralogical composition was similar to that of the initial milled ZVI with  $60 \pm 5\%$  of Fe (0) and  $35 \pm 5\%$  of Fe carbide. As expected, a slight increase of the amount of spinel phase occurred with  $10 \pm 5\%$  of magnetite/maghemite as a consequence of Fe(0) corrosion. After 105 days,  $40 \pm 5\%$  of Fe (0),  $40 \pm 5\%$  of Fe carbide, and  $20 \pm 5\%$  of magnetite/maghemite were measured indicating on further corrosion of milled ZVI present for both field site conditions.

The presence of Fe(II) in  $Fe_3O_4$  and only Fe(III) in  $\gamma Fe_2O_3$  was discriminated by obtaining XANES spectra. The structural evolution of milled ZVI obtained from XANES spectra is shown in Table 9. After 7 days of incubation the mineralogical composition was similar to the initial milled ZVI:  $91 \pm 9\%$  (Solvay, CH) and  $92 \pm 9\%$  (Balassagyarmat, HU) of signal is attributed to the initial milled ZVI. A slight contribution of maghemite ( $< 10\%$ ) was again attributed to Fe(0) corrosion.

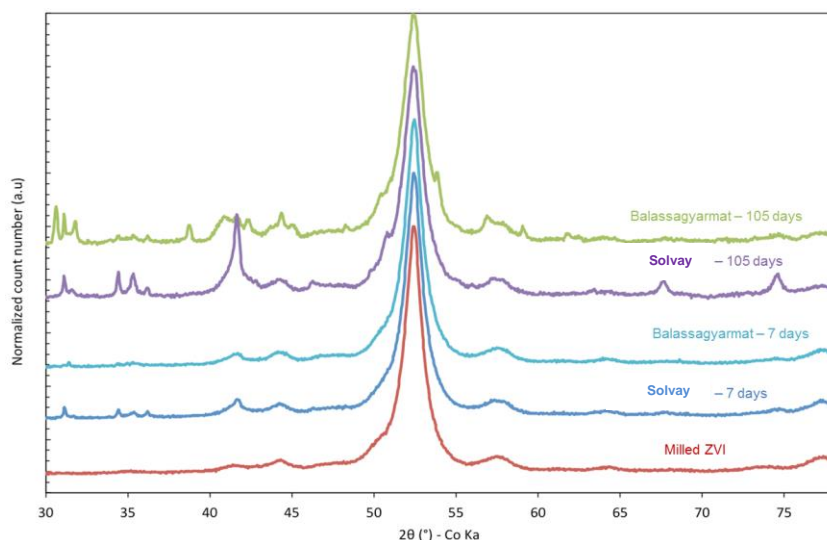


**Figure 22:** XRD patterns of the milled ZVI at the beginning of experiment (red), as well as after 7 and 105 days of contact with PM from the Solvay, CH and Balassagyarmat, HU field site.

After 105 days, a significant contribution of  $23 \pm 2\%$  of  $\gamma\text{Fe}_2\text{O}_3$  and  $10 \pm 1\%$  of  $\text{Fe}_3\text{O}_4$  was necessary to fit the spectra of the initial milled ZVI for batch reactor with the PM from Solvay field site, CH. Only  $65 \pm 7\%$  of the XANES signal is attributed to the milled ZVI. The same trend is observed for milled particles in contact with PM from Balassagyarmat site, HU with  $80 \pm 8\%$  of XANES signal attributed to the milled ZVI and  $10 \pm 1\%$  and  $12 \pm 1\%$  attributed to  $\gamma\text{Fe}_2\text{O}_3$  and  $\text{Fe}_3\text{O}_4$ , respectively. Interestingly, these slight differences on milled ZVI compositions obtained after 105 days are not statistically different to conclude on faster corrosion rate of milled ZVI in the presence of different aquifer materials. This is in agreement with apparent corrosion rate data where no significant difference in terms of Fe lifetime between the two sets was observed.

**Table 9:** Mineralogical composition of milled ZVI at the beginning of experiment and after 7 and 105 days of contact with aquifer material from the Solvay, CH and the Balassagyarmat, HU field sites determined by XANES. Fit range: -12 eV–36 eV above the edge.

	Samples from the batch reactor with PM Solvay, CH field site		Samples from the batch reactor with PM Balassagyarmat, HU field site	
	7	105	7	105
Milled ZVI (%)	$91 \pm 9$	$65 \pm 7$	$92 \pm 9$	$80 \pm 8$
Maghemite (%)	$8 \pm 1$	$23 \pm 2$	$7 \pm 1$	$10 \pm 1$
Magnetite (%)	n.d.	$10 \pm 1$	n.d.	$12 \pm 1$

n.d. – not detected

**In conclusion**, fate of milled ZVI (in terms of the corrosion rate, particle lifetime and Fe speciation) in reaction with TCE is expected to be less dependent on the porous media type at the field site. Nevertheless, as previously shown for NANOFE 25S particles (Schmid et al., 2015) the reaction rate (when normalized on the particle surface area) obtained in a batch reactor can be significantly higher than the one deriving from a column reactor (a more field-site realistic setting). Therefore, it can be expected that in a full-scale field groundwater remediation the reaction constants of milled ZVI are smaller and the particle lifetime is longer, which is advantageous for the treatment of contaminants, especially in case of a slow contaminant release.



### Results (column reactor)

The experimental data from the column reactor revealed an accelerated PCE NAPL dissolution 13–44 days from the beginning of the experiment, with an average PCE concentration of 95 mg/L. At the end of the experiment (56 days) approximately 40% of the initial PCE NAPL was discharged from the column reactor simultaneously by dissolution and convective transport.  $\text{Cl}^-$  concentration declined after 44 days. An apparent PCE degradation efficiency of ca. 20% (in terms of  $\text{Cl}^-$  formation) was determined, but this value disregards the degree of dechlorination. Only 9% of the PCE was degraded to TCE (Table 10). Traces of *cis*-DCE, *trans*-DCE and VC were detected (data not shown). Final PCE degradation products were ethane (dominating) and ethene.

**Table 10:** Degradation pathway of PCE via milled ZVI and percent of anaerobic corrosion as determined in column reactor.

Parameter	[%]
PCE → $\text{Cl}^-$	21
PCE → TCE	9
PCE → ethene	1
PCE → ethane	5
$m_{\text{corroded Fe(0)}}/m_{\text{overall consumed Fe(0)}}$	66

Magnetic susceptibility measurements revealed a decrease of ca. 13% of the scan area after ca. 2 months of the experiment duration (Figure 23). No  $\text{H}_2$  gas was detected until day 19 of the experiment, but a gas accumulation was visible in the column. With regard to  $\text{Cl}^-$ ,  $\text{H}_2$  and ethane formation, 66% of the overall consumed  $\text{Fe}^0$  was attributed to anaerobic corrosion (Table 10).

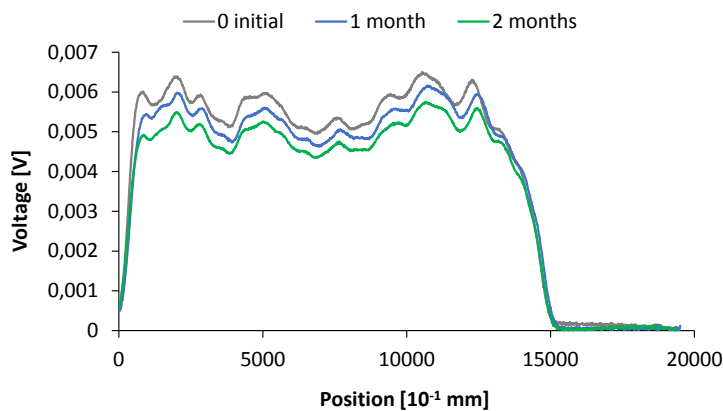


**Figure 23:** Changes in  $\text{Fe(0)}$  concentration (measured by means of magnetic susceptibility) along the column during the experiment.

**In conclusion**, as milled ZVI particles seem to offer a better relationship between PCE dechlorination and corrosion compared to NANOFER 25S (Menadier Stavelot, 2015), the application of milled ZVI may be advantageous at field sites where the oxygen content in groundwater is relatively high, such as at the PCE-contaminated Solvay, CH field site.



## 4.5 Carbo-Iron® (SciDre GmbH, UFZ Leipzig)

Responsible partner: UFZ

Contributors: USTUTT

Carbo-Iron® is a composite material developed at the UFZ Leipzig and produced by Scientific Instruments GmbH, Germany. The composite consists of finely ground activated carbon ( $d_p \approx 1 \mu\text{m}$ ) and embedded nano sized zero valent iron structures with a mean size  $d_{\text{Fe}(0)} \approx 50 \text{ nm}$  (Figure 24) (MacKenzie et al., 2012).

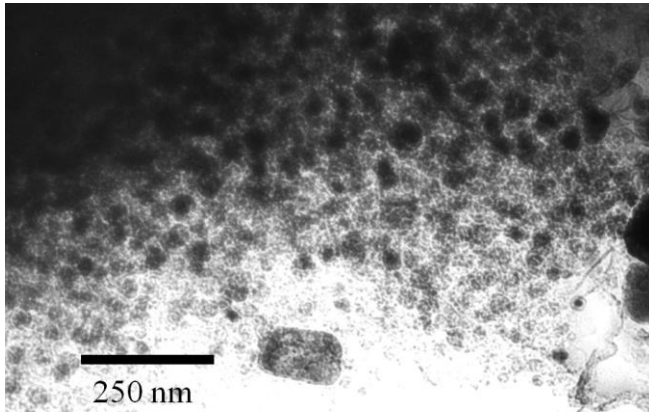


**Figure 24:** Bright field TEM image of Carbo-Iron®

Optimization of Carbo-Iron® was carried out in terms of upscaling the production of particles with the adjusted Fe content (to 30 wt%), improving the suspension stability and transport (including the targeted emplacement) by means of CMC, as well as the reactivity and lifetime of the particle in suspension. This report focuses on the transport behavior of optimized Carbo-Iron®.

### 4.5.1 Stability of Carbo-Iron® suspension

*Carboxymethyl cellulose (CMC) effectively stabilizes Carbo-Iron® (when  $c_{\text{particle}} \leq 30 \text{ g/L}$ ). Long-term suspension stability is achieved with  $c_{\text{CMC}} = 0.1\text{--}0.2 \times c_{\text{particle}}$ , allowing for longer particle travel distances during the injection ("plume treatment mode",  $L_{T, 50} \approx 2 \text{ m}$ ). When  $c_{\text{CMC}} = 0.05\text{--}0.09 \times c_{\text{particle}}$  a "metastable" suspension is formed, suitable for shorter injection time and particle emplacement closer to the injection port ("source treatment mode",  $L_{T, 50} < 1 \text{ m}$ ).*

**Experimental protocol** Stability of particle suspension ( $c_{\text{particle}} = 20 \text{ g/L}$  in artificial groundwater F.II.a) was determined by measuring the sedimentation profile in suspension containing 20 wt% Fe(0). Static sedimentation experiments were carried out in closed bottles under inert atmosphere; an aliquot of the particle suspension was sampled at a pre-defined height (1 or 4 cm below the water table) and analyzed for the particle concentration.

**Results** Variation of the sedimentation profile for Carbo-Iron® suspension depending on the CMC concentration is shown in Figure 25. The uppermost aliquot (1 cm below the water table) appeared to be more sensible and therefore better suitable for determination of suspension stability (Figure 25B). An adequate stability was achieved with a higher CMC content (Figure 25A).

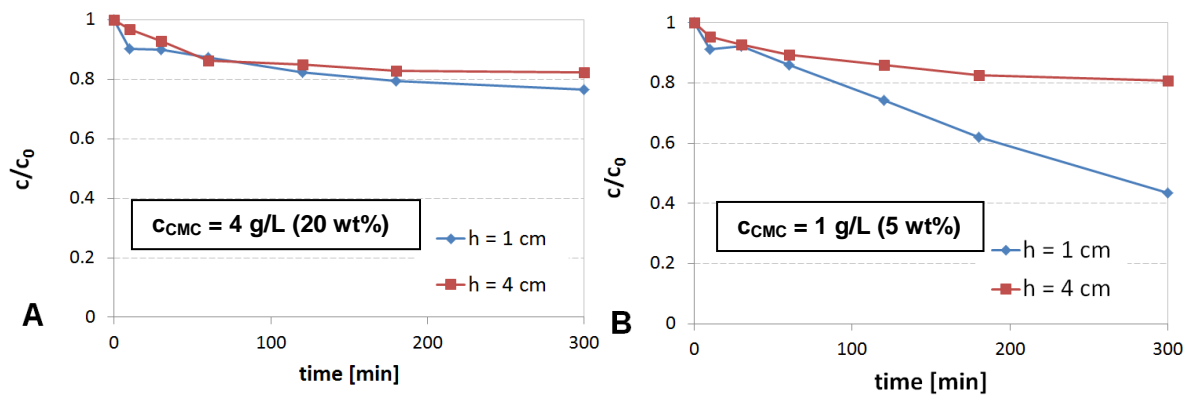


**Figure 25:** Sedimentation profile of Carbo-Iron® suspensions measured at 1 and 4 cm below the water table. A:  $C_{CMC} = c_{particle} \times 0.2$ , B:  $C_{CMC} = c_{particle} \times 0.05$ .

Sedimentation experiments with the suspensions containing even higher content of Carbo-Iron® ( $c_{particles} = 30 \text{ g/L}$ ,  $c_{Fe(0)} = 6 \text{ g/L}$ ) and various CMC concentrations (1–25 wt%) showed that the maximum particle stabilization was achieved with 20 wt% CMC. Higher CMC content (25 wt%) did not improve the suspension stability (Figure 26A). After longer time (>25 min) the suspension with 5 wt% of CMC appears to be less stable compared to the others and is therefore referred to as “metastable”. Independently on the particle concentration the long-term ( $t > 3 \text{ h}$ ) stability of the suspension (for 70–80% of the particle mass) was achieved with  $C_{CMC} = c_{particle} \times 0.2$  (Figure 26B). The remaining 30–20% mass are attributed to agglomerates, which deposited within the first cm prior to sampling of the aliquots.

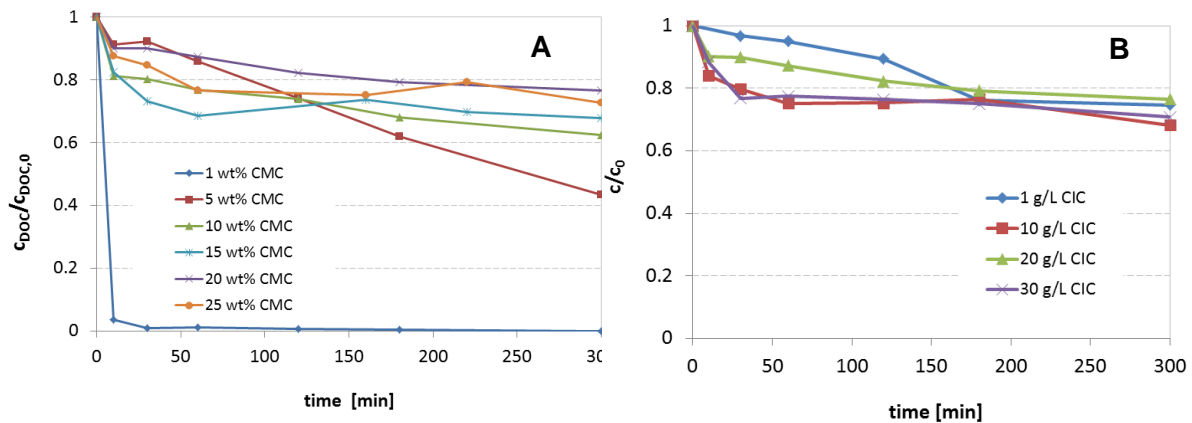


**Figure 26:** Sedimentation profile of Carbo-Iron® suspensions containing A: 30 g/L of particles and varying CMC content and B: varying particle and CMC content with  $C_{CMC} = c_{particle} \times 0.2$ . Aliquots sampled 1 cm below the water table.

#### 4.5.2 Mobility and Delivery of Carbo-Iron

*CMC-stabilized Carbo-Iron® is mobile both in standardized quartz porous medium M.I and in the porous medium from the Balassagyarmat field site, HU, with the max travel distance ( $L_{T,99.9}$ ) > of ca. 4.5 m estimated for the latter. Variation of particle and CMC content offers the possibility for both, broad treatment zone and source-targeted particle emplacement.*

*Metastable Carbo-Iron® suspension and the 3-fold intermittent injection are recommended for source treatment. This was confirmed in the LSF experiment, where a near-source emplacement of the large proportion of particles mass was demonstrated.*

**Experimental protocol** Mobility of CMC-stabilized Carbo-Iron® ( $c_{\text{particle}} = 5.7 \text{ g/L}$ ,  $c_{\text{Fe(0)}} = 1.1 \text{ g/L}$ ,  $c_{\text{CMC}} = 1.1 \text{ g/L}$ ) was studied in D.I columns (1.6 cm i.d., 25 cm saturated packed bed length) filled with Dorsilit® (M.I). Standardized water with different hardness served as a background electrolyte. The pressure drop was continuously recorded by a pressure device connected to the column inlet and outlet. The column tests were carried out under the injection conditions ( $v_{\text{eff}} = 10 \text{ m/d}$ ). The influence of the CMC content on particle mobility was additionally studied under the same experimental conditions but with varying particle-to-stabilizer ratio and with particle suspensions prepared in moderately hard water (F.I.m).

In order to reveal the Carbo-Iron® mobility after the injection at the Balassagyarmat field site, HU, the mobility of Carbo-Iron® suspensions (as applied at the site,  $c_{\text{particle}} = 15 \text{ g/L}$ ,  $c_{\text{CMC}} = 1.5 \text{ g/L}$  prepared in groundwater from the site) was tested in horizontal D.I columns (3.5 cm i.d., 18.9 cm saturated packed bed length) filled with porous medium (fraction < 2 mm,  $d_{50} = 0.38 \text{ mm}$ ,  $n_e = 0.26$ ) and groundwater from this field site (F.II) under the injection condition ( $v_{\text{eff}} = 10 \text{ m/d}$ ). The injected Carbo-Iron® contained 21.4% Fe(0) and 55.9% C and had the following size distribution  $d_{10}/d_{50}/d_{90} = 0.4 \text{ }\mu\text{m}/1.3 \text{ }\mu\text{m}/2.5 \text{ }\mu\text{m}$ .

In preparation for the LSF experiment the performance of the (meta)stable Carbo-Iron® suspension was tested in vertically orientated D.II columns (3.5 cm i.d., 100 cm saturated packed bed length) filled with M.II. Artificial groundwater F.II.a served as a background electrolyte. A 3-fold intermittent injection mode was applied at the injection flow velocity of 52 m/d and subsequent resting time of ca. 24 h with groundwater flow velocity of 0.25 m/d. CMC-Carbo-Iron® sorption isotherm experiments were performed in search for the best performing particle suspension. The emplacement of the selected optimal suspension within the selected distances from the injection port was further tested under the same experimental conditions.

#### **Results (Optimization of CMC-stabilized Carbo-Iron® suspensions towards an enhanced mobility)**

Particle breakthrough was close to unity (Figure 27), indicated that CMC-stabilized Carbo-Iron® is highly mobile in M.I, independently on the type of water the particle suspension was prepared in. For all the experimental conditions there was 50% of the particle breakthrough after only 1.2 exchanged pore volumes. Suspensions prepared in F.I.s and F.I.m showed a breakthrough of ca. 90%, while more retardation (ca. 40%) was observed for the suspensions prepared in hard water (F.I.h). This is most likely due to particle destabilization caused by the higher content of bivalent cations in the latter water type, causing particle aggregation and subsequently aggregates filtration by the porous medium. Nevertheless, no clogging of the saturated column occurred ( $\Delta p \leq 11 \text{ mbar}$ ). The predicted max travel distances ( $L_{T,99}$ ) varied from ca. 3 to ca. 16 m (Table 11).

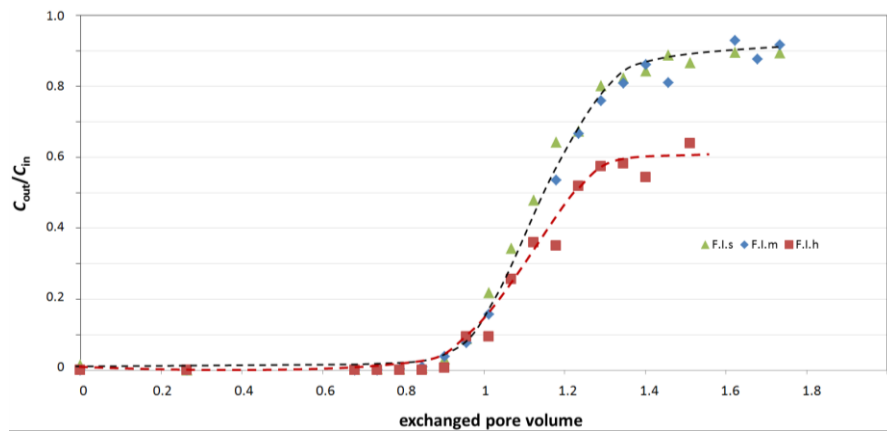


**Figure 27:** Breakthrough curves for CMC-stabilized Carbo-Iron® prepared in different types of standard water (D.I column filled with M.I,  $c_{0,particle} = 5.7 \text{ g/L}$ ,  $c_{Fe(0) \text{ in particles}} = 1.1 \text{ g/L}$ ,  $c_{CMC} = 1.1 \text{ g/L}$ ,  $v_{eff} = 10 \text{ m/d}$ ,  $n_{e(M.I)} = 0.33$ ).

Mobility of Carbo-Iron® suspensions prepared in F.l.m strongly depends on the particle-to-CMC ratio. The most mobile is the particle suspension with  $c_{particle}/c_{CMC} = 5$  (green line in Figure 28). The suspension mobility decreased in the following order of particle-to-CMC ratio:  $5 > 10 > 20$  (Figure 28).

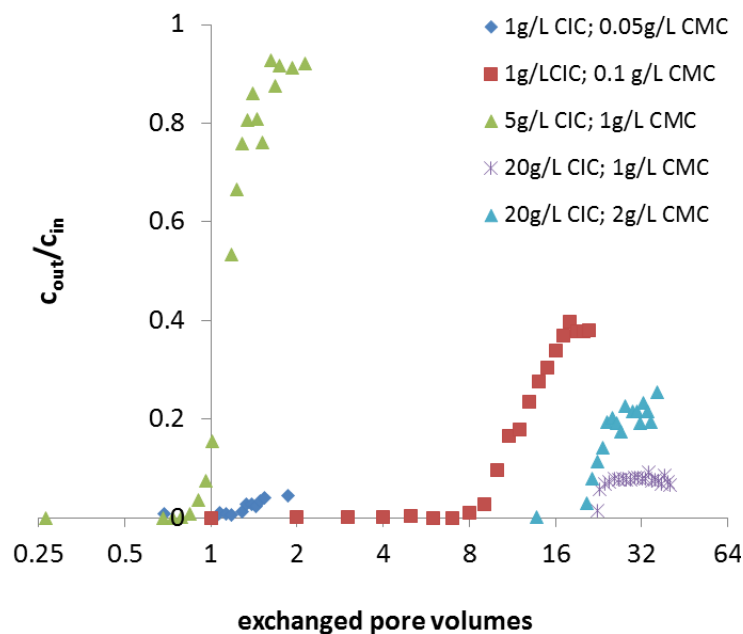


**Figure 28:** Breakthrough curves for CMC-stabilized Carbo-Iron® suspension in F.l.m with various particle-to-CMC ratio (D.I column filled with M.I,  $v_{eff} = 10 \text{ m/d}$ ,  $n_{e(M.I)} = 0.33$ );  $c_{Fe(0) \text{ in particles}} = 19.9 \text{ wt\%}$ ). Note that “CIC” in this figure legend refers to Carbo-Iron® particles.

The predicted travel distances of the suspensions in F.l.m for 50% of particle removal reached 1.5 m, while the max particle removal occurred at ca. 15 m (Table 11).

**In conclusion**, since not-stabilized CMC Carbo-Iron® suspensions are not mobile in porous medium (see Table 11, first row) the stabilization of Carbo-Iron® is necessary for the successful injection of these particles, whereby the best performing suspensions (in soft and moderately hard water) contain the particle-to-CMC ratio of 5.

**Table 11:** Mobility parameters and estimated transport distances for CMC-stabilized Carbo-Iron® in M.I under the injection conditions.

$c_0$ (NP) [g/L]	$c_{CMC}$ [g/L]	PM	$n_e$ [%]	Fluid	$V_{eff}$ [m/d]	$k$ [1/s]	$\alpha$ [-]	$L_T$ (50%) [m]	$L_T$ (63%) [m]	$L_T$ (99.9%) [m]
1	0	M.I		F.l.m	10	-	-	-	-	-
1	0.05	M.I	0.35	F.l.m	10	1.4E-3	>1	0.06	0.08	0.56
1	0.1	M.I	0.43	F.l.m	10	4.2E-4	0.45	0.19	0.27	1.9
5.7	1.1	M.I	0.37	F.l.s	10	4.9E-5	0.05	1.6	2.4	16.4
5.7	1.1	M.I	0.37	F.l.m	10	5.4 E-5	0.05	1.5	2.1	14.8
5.7	1.1	M.I	0.37	F.l.h	10	2.4E-4	0.22	0.34	0.49	3.4
20	1	M.I	0.34	F.l.m	10	1.2E-3	$\approx 1$	0.07	0.09	0.68
20	2	M.I	0.42	F.l.m	10	7.0 E-4	0.72	0.11	0.16	1.14
20	4	M.I	0.41	F.l.m	10	6.3 E-4	0.64	0.13	0.18	1.28

### **Results (Mobility of Carbo-Iron® in porous medium and groundwater from the Balassagyarmat field site, HU)**

The preliminary results demonstrated that the larger aggregates of CMC present in the CMC solution clogged the porous media. Therefore, the subsequent column tests were performed with the particle suspension stabilized with the filtrated fraction of the CMC solution.

Permeability of the porous medium from the Balassagyarmat field site, HU was heterogeneous (with impermeable lenses of fines), which lead to an inhomogeneous distribution of Carbo-Iron® on the mineral grains (Figure 29). Nevertheless, > 70% of the injected mass was mobile, with the particle breakthrough reached after 2.2 exchanged pore volumes (Figure 30). The mean particle loading on the sediment was 5 g/kg.

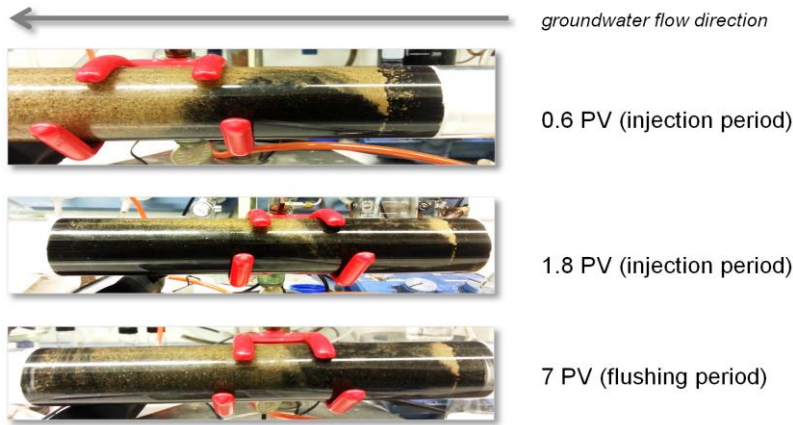


**Figure 29:** Glass columns filled with porous medium from the Balassagyarmat field site, HU, showing an inhomogeneous distribution of Carbo-Iron® during and after the injection of the particle suspension.

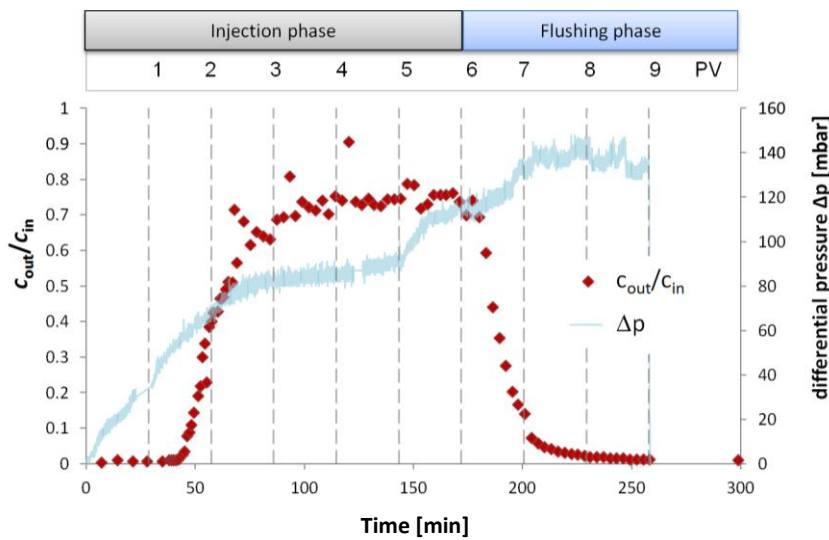


**Figure 30:** Breakthrough of Carbo-Iron® in porous medium and groundwater from the Balassagyarmat field site, HU ( $C_{particle} = 15$  g/L,  $C_{CMC} = 1.5$  g/L, D.II column,  $n_e = 0.26$ ,  $v_{eff} = 10$  m/d).

Predicted travel distances and transport parameters are shown in Table 12. 50% of the particle mass reached ca. 0.5 m, while the max estimated travel distance was > 4.5 m (Table 12).

**Table 12:** Mobility parameters and estimated transport distances for CMC-stabilized Carbo-Iron® in porous medium and groundwater from the Balassagyarmat field site, HU under the injection conditions.

$C_0$ (NP) [g/L]	$C_{CMC}$ [g/L]	Porous media (PM)	$n_e$ [%]	Fluid	$V_{eff}$ [m/d]	$k$ [1/s]	$\eta_0$ [-]	$\alpha$ [-]	$L_T$ (50%) [m]	$L_T$ (63%) [m]	$L_T$ (99.9%) [m]
15	1.5	Balassagyarmat, HU field site (< 2 mm)	0.26	F.II	10	1.7E-4	5.5E-3	0.09	0.47	0.67	4.65

A slight decrease in the particle size distribution in the column inflow was observed compared to that in the injected suspension, suggesting that a portion of somewhat larger Carbo-Iron® particles was filtered out and remained in the porous medium (data not shown).

### **Results (Targeted particle deposition within porous medium (delivery) in preparation for the LSF experiment)**

The prerequisite for Carbo-Iron® injection in the LSF experiment was an irreversible particle emplacement in a near-source zone, of a sufficiently stable suspension with max amount of reactive particles. As described in Section 4.5.1., a (meta)stable suspension of Carbo-Iron® contains  $C_{CMC} = 0.05-0.2 \times C_{particle}$ .

Carbo-Iron® suspensions containing higher CMC concentrations ( $C_{CMC} > C_{particle} \times 0.15$ ) showed high mobility, with only < 55% of the particle mass being retarded within 1 m. Similar results were obtained in a 2D small-scale flume test carried out by USTUTT. This result opposed the irreversible particle deposition being the aim of the abovementioned LSF experiment. In order to better control particle deposition and provide optimal distribution of particles within the sediment, the amount of CMC and especially the freely dissolved fraction of CMC needed to be reduced, but the suspension stability for a given injection time needed to be maintained. The sorption isotherms experiments revealed that the CMC-stabilized Carbo-Iron® suspensions optimal for the injection in the LSF experiment contains  $C_{particle} = 20$  g/L, with 5–10 wt% of CMC ( $C_{CMC} > C_{particle} \times 0.05-0.1$ ) (Table 13). Within that range the freely dissolved CMC fraction  $C_{CMC, free}$  reached a minimum, while the fraction of CMC able to stabilize the particles was still sufficiently high to maintain metastable suspensions. The metastable suspension ( $C_{particle} = 20$  g/L,  $C_{CMC} = 1$  g/L) was therefore selected as the optimal suspension for testing the targeted deposition of desired amount of Carbo-Iron® particles.

**Table 13:** Calculated equilibrium concentrations for freely dissolved ( $C_{CMC, free}$ ) and CMC loaded on particles ( $\rho_{CMC \text{ on particles}}$ ) from sorption isotherm measurements ( $C_{particles} = 20$  g/L).

$C_{CIC}$ [g/L]	$C_{CMC, total}$ [g/L]		$C_{CMC, free}$ [mg/L]	CMC loading on particles $\rho$ [wt%]
		$C_{CMC}/C_{particle}$		
20	4	0.2	2600	7 <sup>1</sup>
20	2	0.1	600	7 <sup>1</sup>
20	1.5	0.075	157	6.7
20	1	0.05	99	4.5

<sup>1</sup> maximal reachable loading of particles with CMC according to sorption isotherms

The results showed that ca. 90 % of injected particle mass in the chosen metastable suspension travelled a distance of 1 m. The sediment loading with Carbo-Iron® was up to 1 wt% higher in the close vicinity of the injection point (ROI: 0–30 cm, Figure 31), being in accordance with the LSF experimental goal.



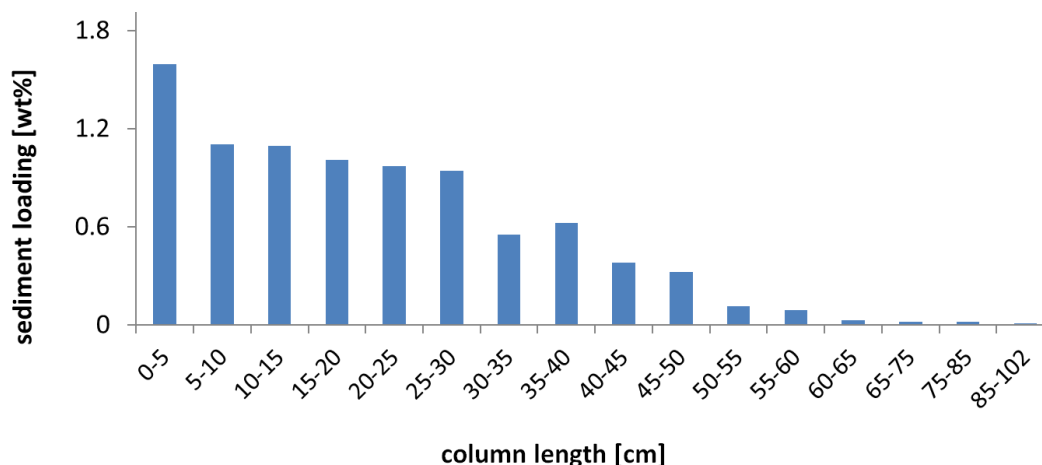


**Figure 31:** Spatial distribution of Carbo-Iron® in the sediment as function of the distance from the injection port.  $c_{\text{particle}} = 20 \text{ g/L}$ ;  $c_{\text{CMC}} = 1 \text{ g/L}$ ; porous media: M.II; 3 intermittent injection cycles;  $v_{\text{eff}} = 52 \text{ m/d}$ , subsequent resting time ca. 24 h at groundwater flow at  $v_{\text{eff}} = 0.25 \text{ m/d}$ .

#### 4.5.3 Fate of Carbo-Iron® under field relevant conditions

The following aspects of fate of Carbo-Iron® under field relevant conditions were studied:

- Particle **reactivity** ( $k_{\text{dechl, obs}} = 1.3 \times 10^{-2} / \text{h}$  **with respect to dissolved PCE or PCE NAPL**), particle **efficiency** and long-term **transformation of Fe(0) - Fe speciation**
- **Contaminant sorption** by Carbo-Iron® after the long-term aging

*Carbo-Iron® particles combine sorption and degradation of organic contaminants, such as PCE. There is no significant difference between the reactivity of Carbo-Iron® in groundwater and synthetic water. Reaction rate constants with dissolved PCE (plume treatment simulation) derived from batch- and column reactors were almost identical.*

*In a PCE source-treatment simulation the PCE conversion amounted to ca. 72% under Fe-limited conditions within 75 days. Compared to a particle-free column, the PCE discharge from a Carbo-Iron®-loaded column was lower for several orders of magnitude.*

*Transformation of Fe(0) e.g. into magnetite is comparable to that of nZVI.*

**Experimental protocol** Long-term transformation of Fe(0) was studied by means of X-ray diffraction (XRD) measurements in fresh samples and in the aged sample (for 27 days at 25 °C) in moderately hard water (F.I.m). The sorption of PCE and dichloromethane was studied for activated carbon colloids, fresh Carbo-Iron® and aged Carbo-Iron®.

Abiotic dechlorination of a PCE plume by Carbo-Iron® was studied in column reactor ( $\text{pH} = 9.4$ ;  $c_{\text{PCE},0} = 25 \text{ mg/L}$ ) as described in Bleyl et al. (2012). Degradation of a PCE NAPL by Carbo-Iron® was studied in a column reactor (3.5 cm i.d., 20 cm saturated packed bed length) filled with M.II porous medium ( $n_e = 0.26$ ) following Standardized experimental protocols for non-aqueous phase remediation. In brief, Carbo-Iron® powder was mechanically mixed with the porous medium in final particle load of 1 wt% ( $m_{\text{tot, particle}} = 2.54 \text{ g}$ ,  $m_{\text{tot, Fe(0)}} = 0.51 \text{ g}$ ) creating a 14 cm long reactive zone, with a non-particle-loaded area in front of it. After an equilibration time of 24 h, the contaminant pool, the PCE NAPL, was emplaced at the inflow area ( $V_{\text{PCE}} = 100 \mu\text{L}$ ;  $m_{\text{PCE}} = 162 \text{ mg}$ ). The applied amount of reactants corresponded to a molar ratio of  $n_{\text{Fe(0)}} : n_{\text{PCE}} = 9 : 1$  and to a 2-fold stoichiometric excess of Fe(0)

(in a scenario with ethene as major dechlorination product). This represented Fe(0)-limited conditions, since previous work showed that a 5–10-fold stoichiometric excess is recommended for complete degradation of chlorinated hydrocarbons, when taking into account undesired side reactions (Henn, 2005). O<sub>2</sub>-free standard water F.I.m served as an eluent pumped into the column reactor with a flow rate of  $q = 0.78$  mL/min, obtaining simulated groundwater flow velocity of  $v_{\text{eff}} = 4.5$  m/d. Column effluents were continuously collected and their aliquots analysed for Cl<sup>-</sup> content (considered to be the most reliable for calculation of mass balance). Ethene, ethane and ethyne were measured from the headspace. Fe(0) content in Carbo-Iron<sup>®</sup> after the reaction was determined by H<sub>2</sub> production after the acidification of the re-suspended particles. In order to elucidate the PCE retardation by Carbo-Iron<sup>®</sup> particles, an experiment in Fa control column reactor (without Carbo-Iron<sup>®</sup>) was conducted in parallel.

**Results (Transformation of Fe(0))** XRD revealed single peaks of crystalline Fe(0) clusters (estimated size ca. 50 nm) within the fresh Carbo-Iron<sup>®</sup> and the background intensity deriving from the amorphous carbon backbone at observed diffraction angle (Figure 32a). In the sample long-time exposed to near-natural water F.I.m., Fe(0) crystallites transformed into Fe crystalline oxide magnetite (Figure 32b).

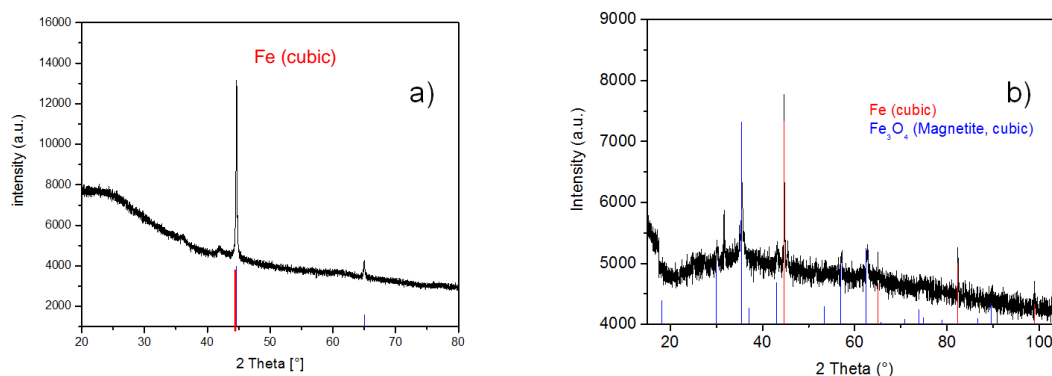


**Figure 32:** Powder XRD spectrum of fresh Carbo-Iron<sup>®</sup> (a) and Carbo-Iron<sup>®</sup> aged in F.I.m for 27 days at 25 °C (b).

**Results (Contaminant sorption onto Carbo-Iron<sup>®</sup>)** From the literature it is known, that formation of Fe precipitates (such as Fe(III)-oxide-hydroxides or carbonates) may lead to their deposition on the particle surface, which in turn may influence the reaction rate and mechanism but also can hinder the transfer of reactive species (e.g. e<sup>-</sup>, H<sub>2</sub>). The Freundlich sorption isotherms revealed in fact a very similar behaviour of activated carbon colloids, Carbo-Iron<sup>®</sup> and aged Carbo-Iron<sup>®</sup> for PCE and dichloromethane (Table 14), indicating that the carbon backbone did not lose the sorption abilities by particle alteration and formation of Fe oxides. It is therefore expected that the sorption ability of Carbo-Iron<sup>®</sup> won't be significantly reduced at the field.

**Table 14:** Freundlich parameters calculated for Carbo-Iron<sup>®</sup>, activated carbon colloids and Carbo-Iron<sup>®</sup> for the sorption of two contaminants. Note that there are no parameters for Carbo-Iron<sup>®</sup> and PCE due to significant PCE degradation during the sorption experiment.

Contaminant	Particle type	Log K <sub>F</sub> [mg <sup>(1-1/n)</sup> L <sup>1/n</sup> /kg]	n
PCE	Activated carbon colloids	4.8	0.50
	Aged Carbo-Iron <sup>®</sup>	4.8	0.44
Dichloromethane	Activated carbon colloids	3.3	0.90
	Carbo-Iron <sup>®</sup>	3.2	0.84
	Aged Carbo-Iron <sup>®</sup>	3.2	0.91

**Results (Reactivity of Carbo-Iron<sup>®</sup> during the PCE plume dechlorination in a column reactor)** Low concentrations of PCE (in a PCE plume) are effectively sorbed by and enriched in the porous activated carbon within Carbo-Iron<sup>®</sup>, being brought to the vicinity of the reactive Fe(0). It was shown for the first time in a column reactor that dissolved PCE was degraded by the Carbo-Iron<sup>®</sup> to fully dechlorinated products. The observed dechlorination rate constant ( $k_{\text{dechl, obs}}$ ) was  $1.3 \times 10^{-2}/\text{h}$  under the experimental conditions (with > 90% of the initial PCE sorbed onto activated carbon), which was comparable to that of a batch reactor.

**Results (Reactivity of Carbo-Iron<sup>®</sup> during the PCE NAPL dechlorination in a column reactor)**

The Cl<sup>-</sup> concentration increased sharply in the column effluent after 3–4 pore volumes were exchanged, reaching a max of 90 ppm, after which the concentration lowered to < 20 ppm and remained constant (Figure 33). These two phases in Cl<sup>-</sup> formation can be explained as (i) PCE sorption and fast dechlorination at highly reactive reducing centres and (ii) PCE degradation at lower reaction rate or mass transfer limited reaction due to inhomogeneous spatial PCE distribution. When after 75 days of the reaction (and 362 pore volumes exchanged) no significant change of Cl<sup>-</sup> concentration was observed, the experiment was terminated. The total Cl<sup>-</sup> mass was about 99.9 mg, equivalent to a conversion of 72.1% PCE. The remaining PCE was extracted from the column and amounted to 32%, being in a good accordance with the Cl<sup>-</sup> mass balance. Less than 0.5 wt% Fe(0) was detected after 75 days of the reaction, indicating a limited lifetime of Fe(0) in Carbo-Iron<sup>®</sup> under the tested conditions.

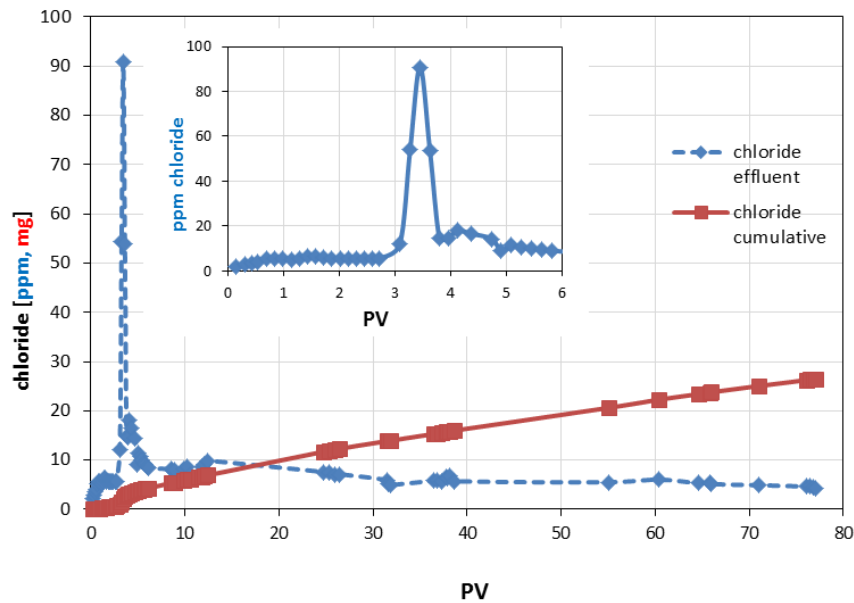


**Figure 33:** Concentrations of  $\text{Cl}^-$  at the outlet of the column reactor (M.II,  $n_e = 0.26$ ,  $v_{\text{eff}} = 4.5 \text{ m/d}$ , length of reactive zone: 14 cm,  $m_{\text{PCE}} = 162 \text{ mg}$ ). PV = pore volume.

Particle efficiency is expected to be lower in a column- compared to a batch reactor, given the inhomogeneous contaminant distribution, sorption-controlled contaminant transport, relevance of undesired side reactions (such as anaerobic corrosion) and inability of achieving an optimal content and distribution of reactive particles in the vicinity of the PCE NAPL (contaminant source). Nevertheless, the particle efficiency derived from a column reactor reflects more near-natural conditions. The efficiency of Carbo-Iron<sup>®</sup>, calculated after Equation 1 (Liu et al., 2005) amounted to 29%.

$$\epsilon = \frac{(M_{\text{PCE},0} - M_{\text{PCE},f}) \times n}{2 \times N_{\text{Fe}(0),0}} = \frac{(0.98 \text{ mmol} - 0.31 \text{ mmol}) \times 8}{2 \times 9.1 \text{ mmol}} = 29\% \quad \text{Equation 1}$$

Two thirds of the initial PCE NAPL was reduced. The low remaining concentration of PCE detected in the column effluents in the course of the experimental pointed out an effective retardation of the PCE NAPL by the activated carbon backbone within Carbo-Iron<sup>®</sup>, with the final PCE effluent concentration < 50 ppb, and only traces of chlorinated intermediates, such as TCE and *cis*-1,2-DCE, as shown in Figure 34.

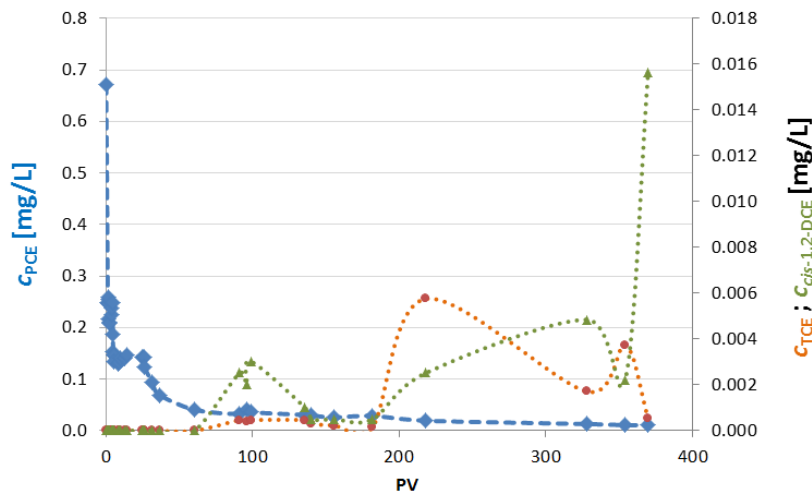


**Figure 34:** Concentrations of chlorinated hydrocarbons (PCE, TCE and *cis*-1,2-DCE) in the column effluents (M.II,  $n_e = 0.26$ ,  $v_{eff} = 4.5$  m/d, length of reactive zone: 14 cm,  $c_{PCE} = 162$  mg); PV = pore volume.

As confirmed in the effluents of the control column reactor (without Carbo-Iron®) ca. 90% of the PCE NAPL was dissolved after ca. 100 exchanged pore volumes, compared to < 0.4% (after ca. 370 exchanged pore volumes) in the column reactor containing Carbo-Iron® (Figure 35). The extracted amount of PCE from the column matrix (after 140 pore volumes) amounted to 11% of the initial amount in the control column reactor, compared to 30% in the column reactor containing the reactive zone with Carbo-Iron®. This all evidenced an intensive PCE retardation by- and reaction with Carbo-Iron® particles within the reactive zone.

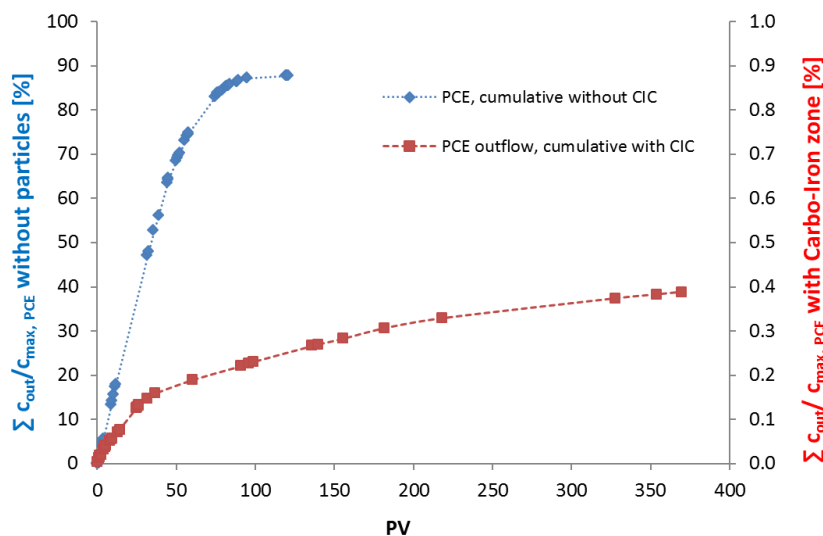


**Figure 35:** Cumulative amount of PCE in column effluents in column reactor containing the reactive zone with Carbo-Iron® (red line) and in control column reactor (without Carbo-Iron®, blue line). Note that CIC refers to Carbo-Iron® particles.

**In conclusion**, these results illustrated a need for further optimization of the source treatment by reactive particles. The focus should be given to delivery of sufficient amount of redox equivalents within the sediment pores as well as to enhancement of particle lifetime, selectivity towards contaminants and efficiency of particles.

## 4.6 Trap-Ox Fe-zeolites

Responsible partner: [UFZ](#)

Trap-Ox Fe-zeolites is a group of particles designed for *in situ* **trapping** of organic contaminants by adsorption and catalytic **oxidation** of adsorbed contaminants in combination with H<sub>2</sub>O<sub>2</sub> (Georgi et al., 2015). Two types of complementary Trap-Ox Fe-zeolite particles were optimized within NanoRem: Trap-Ox Fe-BEA35 and Trap-Ox Fe-MFI120, the former one available in large quantity. Trap-Ox Fe-MFI120 belongs to the group of hydrophobic MFI type zeolites (Gonzalez-Olmos et al., 2013) and is a high performance adsorbent for small organic molecules, including many typical groundwater contaminants. On the other hand, Trap-Ox Fe-BEA35 is a more universal adsorbent and catalyst, able to adsorb and degrade larger contaminant molecules too. A detailed report on reactivity of the two Trap-Ox Fe-zeolites can be found in DL.3.2 (“Assessment of Nanoparticle Performance for Removal of Contaminants – Non-ZVI and Composite Particles”).

Trap-Ox Fe-BEA35 and Trap-Ox Fe-MFI120 are comprised of small spherical primary particles (200–400 nm, Figure 36). Their physical-chemical properties are listed in **Table 15**.

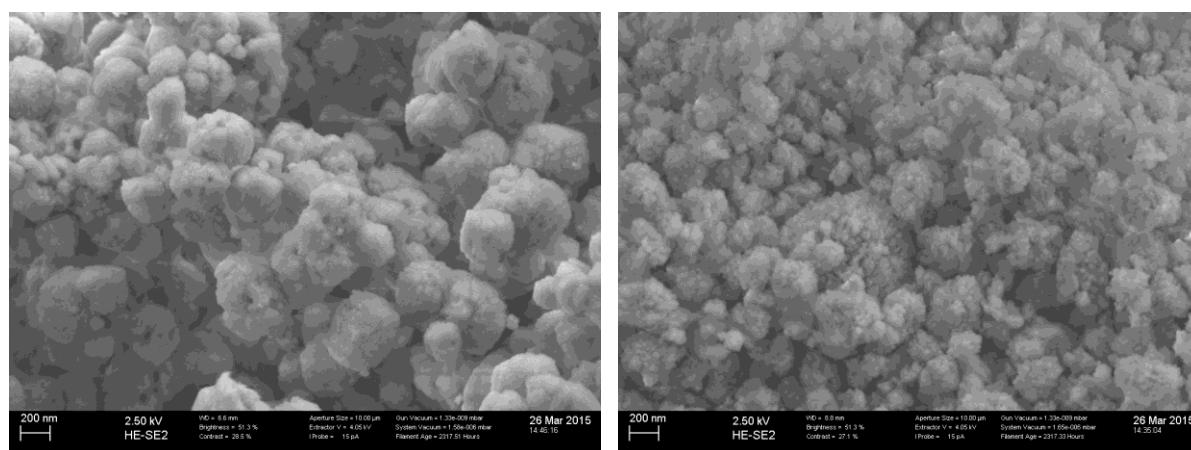


**Figure 36:** Scanning electron microscope (SEM) images of Trap-Ox Fe-BEA35 (left) and Trap-Ox Fe-MFI120 (right).

**Table 15:** Physical-chemical properties of Trap-Ox Fe-zeolites.

Trap-Ox Fe-zeolite type	Molar ratio SiO <sub>2</sub> /Al <sub>2</sub> O <sub>3</sub> [-]	Fe (III) content [%]	Shape of primary particles (SEM images)	Size of primary particles (SEM images) [nm]	Density of particles with water-filled pores [g/mL]
Trap-Ox Fe-BEA35	35	1.3	Spheres, round	ca. 300–400 nm	2.2
Trap-Ox Fe-MFI120	120	0.3	Spheres, round	ca. 200 nm	2.3

Optimization of Trap-Ox Fe-zeolites was carried out in terms of increasing suspension stability and consequently mobility in porous media as well as particle reactivity. This was done by means of particle pre-treatment, addition of stabilizers (CMC, guar gum) and adjustment of suspension pH. Optimal suspensions were finally obtained by a combination of (i) oxidative pre-treatment and (ii) adjustment of slightly alkaline conditions (pH 8 to 8.5).

Trap-Ox Fe-zeolites were not aimed to be injected at a field site within NanoRem, since these particles are still in the premarket developing phase. Nevertheless, as for other NanoRem particles, the tests with Trap-Ox Fe-zeolites were carried out under the conditions that resemble field relevant conditions (e.g. in hard synthetic groundwater (F.l.h) and in presence of NOM).

#### 4.6.1 Stability of Trap-Ox Fe-zeolites

*Slightly alkaline suspensions of Trap-Ox Fe-zeolites (pH 8.0–8.5) are stable over several hours even at high particle concentrations (10 g/L) in very hard water (F.l.h) in the absence of stabilizers.*

**Experimental protocol** Stability of particle suspension, zeta potential and particle size were determined in the relevant pH range from 5.5 to 8.5. The stability of particle suspensions ( $c_{\text{particle}} = 10 \text{ g/L}$ ) was determined by static sedimentation experiments carried out in a measuring cylinder; an aliquot of the particle suspension was sampled at a pre-defined height (17 mm below the water table) in certain time intervals and analyzed for the particle concentration by turbidity measurement (absorbance at 860 nm). Methods for determination of Fe-zeolite concentration in aqueous samples are described in details by Gillies et al. (2016). Intensity-weighted average of particle size (in 1 g/L particle suspension) and zeta potential were measured using Zetasizer Nano ZS (Malvern Instruments Ltd, U.K.).

**Results** The stability of particle suspensions are strongly affected by the suspension's pH (Figure 37). At slightly alkaline suspensions (pH 8.3), Trap-Ox Fe-zeolites are stable for at least 1 h with  $(c/c_0) > 0.8$  even in the absence of stabilizers.

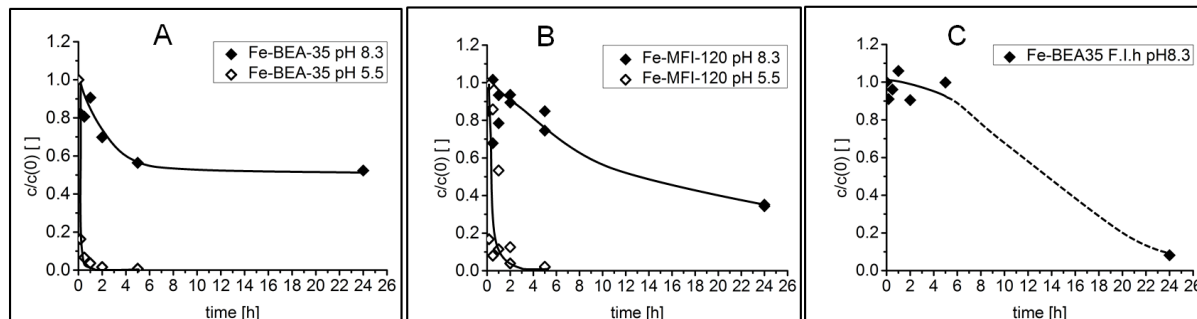


**Figure 37:** Stability of particle suspensions for Trap-Ox Fe-BEA35 (A) and Trap-Ox Fe-MFI120 (B) at pH 5.5 (dashed line) and 8.3 (solid line) and for Trap-Ox Fe-BEA35 in F.l.h (C) (dashed line in C indicates interpolation).

Slightly acidic suspensions (pH 5.5) are highly unstable, despite an overall negative zeta potential of particles (Table 16). This is probably because of the surface charge inhomogeneity caused by a small portion of Fe oxide clusters with positively charged surfaces (point of zero charge at ca. pH 7), which are not reflected in the net measured zeta potential (dominated by the negatively charged aluminosilicate framework of zeolites). Due to attractive electrostatic interactions, Trap-Ox Fe-zeolites are prone to agglomeration at slightly acidic pH, as confirmed by the increased aggregate sizes in suspensions at pH 5.5 compared to those at pH 8.3 (Table 16). Consequently, the stability of Trap-Ox Fe-zeolite suspensions was optimized by adjusting the pH (by NaOH) to close to that of groundwater (8.0–8.5). At this pH, Trap-Ox Fe-zeolites are stable even if very hard water (F.l.h) was used as sus-



pension medium and at high particle concentration (10 g/L, Figure 37C). Thus, the Trap-Ox Fe-zeolite suspension with 10 g/L particles is recommended for future field applications.

**Table 16:** Particle size and zeta potential for Trap-Ox Fe-zeolites in suspensions with various pH.

Zeolite type	pH [-]	Suspension medium	$d_{50}$ [nm] <sup>1</sup>	Zeta potential [mV]
Trap-Ox Fe-BEA35	5.5	10 mM KNO <sub>3</sub>	860 ± 120	-26.2
	8.3	10 mM KNO <sub>3</sub>	545 ± 5	-34.8
	8.5	F.l.h	550 ± 5	-30.0
Trap-Ox Fe-MFI120	5.5	10 mM KNO <sub>3</sub>	600 ± 13	-41.5
	8.3	10 mM KNO <sub>3</sub>	480 ± 29	-49.6
	8.5	F.l.h	840 ± 19	-27.7

<sup>1</sup> intensity-weighted average particle size determined by DLS in suspensions with 1 g/L in 10 mM KNO<sub>3</sub> or F.l.h.

#### 4.6.2 Mobility and Delivery of Trap-Ox Fe-zeolites

*Slightly alkaline suspensions of Trap-Ox Fe-zeolites (pH 8.0–8.5) are highly mobile at flow velocity of 10 m/d even at high particle concentrations (10 g/L) in very hard water (D.I column experiments).*

**Experimental protocol** Optimal Trap-Ox Fe-zeolites suspensions used for mobility studies were obtained by (i) oxidative pre-treatment of Trap-Ox Fe-zeolites (oxidation in suspension by addition of H<sub>2</sub>O<sub>2</sub>) and (ii) pH adjustment to 8.0–8.5 (slightly alkaline conditions). Mobility of these suspensions ( $C_{\text{particle}} = 10$  g/L) was studied in vertically orientated D.I columns (1.7 cm i.d., 20 cm saturated packed bed length) filled with Dorsilit® (M.I) or VEGAS PM (M.II) under the injection conditions ( $v_{\text{eff}} = 10$  m/d). Standardized water with different hardness served as a background electrolyte. The particle concentration on the column effluents was determined by UV/Vis measurements (absorbance at 860 nm).

**Results** The optimized suspensions of Trap-Ox Fe-zeolites showed a good mobility, even at high particle concentration (10 g/L) and relatively low injection velocity of 10 m/d (Table 17).

**Table 17:** Mobility parameters for optimized Trap-Ox Fe-zeolites ( $C_0$  (particle) = 10 g/L) in various porous media and fluids.

NPs	Porous media (PM)	$n_e$ [%]	Fluid / pH	$V_{eff}$ [m/d]	$k$ [1/s]	$\eta_0$ [-]	$\alpha$ [-]	$L_T$ (50%) [m]	$L_T$ (63%) [m]	$L_T$ (99.9%) [m]
Trap-Ox Fe-BEA35	M.I	38	F.l.s/ 8.3	10	3.6E-4	3.1E-3	0.25	0.6	0.8	6.0
Trap-Ox Fe-BEA35	M.I	38	F.l.h/ 8.5	10	3.2E-4	3.1E-3	0.22	0.6	1	6.6
Trap-Ox Fe-BEA35	M.II	27	F.l.h/ 8.5	10	4.6E-4	*	*	0.7	1.0	7.0
Trap-Ox Fe-MFI120	M.I	38	F.l.s/ 8.3	10	1.9E-4	4.4E-3	0.09	1.1	1.6	10.8
Trap-Ox Fe-MFI120	M.I	38	F.l.h/8.5	10	2.8E-4	4.4E-3	0.14	0.8	1.1	7.5

\* transport parameters based on calculation of  $\eta_0$  were not determined due to the grain sizes heterogeneity of M.II.

Breakthrough curves showed a steep increase after only one pore volume was exchanged and reached a plateau of  $c/c_0 \geq 0.75$  in both porous media (even in M.II which has a significant content of fines and Fe oxides, data not shown). In contrast, there was no breakthrough in M.II of slightly acidic suspensions (pH 5.5) (initial pH of suspensions of Fe-zeolites in F.l.s,  $c/c_0 \approx 0$ ) within the first 10 pore volumes, but then it slightly increased within 10 to 20 pore volumes. This was most likely due to the preferential deposition of Trap-Ox Fe-zeolites to positively charged sites (e.g. Fe oxides) within the porous medium and subsequent surface blocking, i.e. inhibition of additional particle deposition by previously formed monolayer. In addition, the pH change from the initially acidic infiltration suspensions (pH 5.5) to slightly alkaline background fluid (pH 8.0–8.5) lead to remobilization of particles, which was not observed when the pH of infiltration suspensions was already adapted to slightly alkaline conditions. Thus, the optimized Trap-Ox Fe-zeolite suspensions are adjusted to pH 8.0–8.5.

For both types of Trap-Ox Fe-zeolites the simulated transport distances for 50% particle removal ( $L_{T,50}$ ) were found, ranging from 0.6 to 1.1 m (Table 17). It should be noted that prediction of long-range transport ( $L_{T,99.9}$ ) based on short-column tests is associated with a high uncertainty. Thus, the upscaling of the column test is necessary in order to be able to predict the transport properties of Trap-Ox Fe-zeolites in the field.

Considering the flow velocity of 10 m/d as the lower limit of the injection velocity, Trap-Ox Fe-zeolites are expected to be even more mobile under higher injection velocity even in the absence of suspension stabilizers.

#### 4.6.3 Fate of Trap-Ox Fe-BEA35 under field relevant conditions

*Trap-Ox Fe-BEA35 actively adsorbs and catalytically (with H<sub>2</sub>O<sub>2</sub>) oxidizes MTBE even beyond 4 adsorption/regeneration cycles and remains active for at least 2 months. Aging of Trap-Ox Fe-BEA35 in very hard water containing NOM for 38 days altered the uptake of divalent cations, but the Fe<sup>3+</sup> content and specific surface area of particles remained nearly unchanged.*

The following aspects of fate of Trap-Ox Fe-BEA35 zeolite under field relevant conditions were studied:

- **Alteration of elemental composition** (related to dry mineral phase), BET specific surface area, catalytic activity and MTBE adsorption after long-term aging in the presence of NOM (batch reactor, experiment duration 38 days)
- **Sorption and degradation potential with respect to MTBE** (column reactor, experiment duration 60 days, with 4 adsorption/oxidation cycles and subsequent analysis of the column filling)

**Experimental protocol** Catalytic activity and adsorption properties of fresh and aged Trap-Ox Fe-BEA35 were studied for 38 days in a recycling batch reactor containing the 10 g/L particle suspension in F.I.h fluid with 7.5 mg/L NOM and pH adjusted (with NaOH) to 8.5. The reactor was constantly shaken on an orbital shaker in a dark room at 10 °C. Fluid in the reactor was 11-fold exchanged every 3–4 days. This was achieved by centrifugation of the suspension, removal of liquid and re-dispersion of the solids in fluid (F.I.h + NOM) in fluid to solid ratio of 1:100. At the end of the experiment an aliquot of Trap-Ox Fe-BEA35 was recovered, dried at 105 °C and afterwards subjected to XRF, UV/Vis-DRS and BET analysis. Another aliquot of the suspension was used to determine catalytic activity and MTBE adsorption properties of the aged Trap-Ox Fe-BEA35.

Long-term changes of adsorption and catalytic properties of Trap-Ox Fe-BEA35 were also studied for 60 days in a column reactor (1.7 cm i.d., 20 cm saturated packed bed length) filled with Dorsilit® (M.I). Porous medium was loaded with Trap-Ox Fe-BEA35 by injection of a particle suspension ( $c_{\text{particle}} = 1 \text{ g/L}$  in F.I.h, pH 5.5 corresponding to native pH of Trap-Ox Fe-zeolite suspension) at  $v_{\text{eff}} = 10 \text{ m/d}$  in a closed-circuit mode, with the particle final load of  $\sim 1.1 \text{ wt\%}$ . The same water type (F.I.h) was used for preparing both the MTBE and H<sub>2</sub>O<sub>2</sub> solutions. The experiment consisted of two alternating phases: MTBE adsorption (analyzed by a Headspace GC/MS) and regeneration with H<sub>2</sub>O<sub>2</sub> (analyzed photometrically at 405 nm after complexation with titanil sulfate). In the adsorption phase, a 10 mg/l solution of MTBE was injected at  $v_{\text{eff}} = 1 \text{ m/d}$  (groundwater flow conditions). After complete breakthrough of MTBE ( $c/c_0 = 1$ ), the column was regenerated by flushing with 10 g/L H<sub>2</sub>O<sub>2</sub> solution.

**Results (Long-term fate in batch reactor)** Changes in the elemental composition of Trap-Ox Fe-BEA35 after the aging was mainly seen in the content of divalent cations (Ca<sup>2+</sup> and Mg<sup>2+</sup>) adsorbed from the F.I.h. The ion exchange positions on the zeolite are associated with the presence of alumina in the zeolite framework, so that each Al creates a negative charge and site for cation binding. As shown by the results from XRF analysis (Table 18), Fe<sup>3+</sup> is the only relevant cation (beside protons) in the original Trap-Ox Fe-BEA35 and its content is not significantly changed in the aged Trap-Ox Fe-BEA35. However, the aged sample contains in addition a significant fraction of Ca and Mg and the molar ratio of (Fe + Ca + Mg)/Al reaches a value very close to 1, which indicates that all Al sites are occupied by 2- or 3-valent cations in a 1:1 binding ratio. In comparison, the ratio of cations/Al for the original Fe-BEA35 was 0.33 and the zeolite showed significant release of protons when contacted

with F.I.h. This indicates that in the original zeolite only part of the ion exchange sites is occupied by Fe and the remaining sites are occupied by protons which are exchanged by divalent cations. The zeolite framework remained intact as indicated by the constant specific surface area and the nearly constant Si/Al ratio (Table 18). The slightly alkaline pH of F.I.h favours some dissolution of Si from the zeolite, as indicated by the slight decline in Si/Al ratio. However, it should be noted that different to natural groundwater, F.I.h contains no dissolved silica which could reflect worst case conditions for Si leaching. According to the UV/Vis- diffuse reflectance spectra (DRS), there is only a very minor increase in the fraction of Fe oxides after the ageing of the zeolite and isolated Fe<sup>3+</sup> on ion exchange positions remains the dominant Fe species.

**In conclusion**, changes in zeolite composition are mainly due to uptake of divalent cations from the hard water.

**Table 18:** Changes in elemental composition (related to dry mineral phase), BET specific surface area, catalytic activity (MTBE, TCE) and MTBE adsorption of Trap-Ox Fe-BEA35 before and after being aged for 38 days.

Property	Trap-Ox Fe-BEA35 fresh	Trap-Ox Fe-BEA35 aged
Al	23.9	26.5
Si	415	421
Fe	16.2	15.8
Ca	0.34	5.5
Mg	< 0.3	12
Na + K	< 0.7	6.6
Molar ratio Si/Al	34	31
Molar ratio (Fe + Mg + Ca)/Al	0.33	1.1
Specific surface area [m <sup>2</sup> /g]	627	634
K <sub>d,MTBE</sub> (at C <sub>free,MTBE</sub> = 6–7 mg/L) [L/kg]	1200	900
A <sub>MTBE</sub> [L/kg/h] <sup>1</sup>	12	1.2
A <sub>TCE</sub> [L/kg/h] <sup>2</sup>	140	52

<sup>1</sup> 50 g/L particles, C<sub>MTBE</sub> = 500 mg/L, 8–10 g/L H<sub>2</sub>O<sub>2</sub>, pH = 8.3–8.5; medium: F.I.h; <sup>2</sup> 7–9 g/L particles, C<sub>TCE</sub> = 100 mg/L, pH 8.3–8.5; medium: F.I.h.

Catalytic activity for MTBE degradation was reduced from 20 L/kg/h in fresh Trap-Ox Fe-BEA35 to 1.2 L/kg/h in aged Trap-Ox Fe-BEA35. In contrast, degradation of a significantly smaller molecule TCE was much less affected by a decrease in catalytic activity (A) of aged Trap-Ox Fe-BEA35. There was only a slight reduction in sorption of MTBE after the ageing of Trap-Ox Fe-BEA35 (f = 1.3 in K<sub>d</sub>, Table 18).

**In conclusion**, the obtained results indicate that full saturation of ion-exchange sites with  $\text{Ca}^{2+}$  and  $\text{Mg}^{2+}$  (in F.I.h) reduces the free diameters of zeolite pores and thus can reduce reaction rates for relatively large contaminant molecules by hindering diffusive mass transfer within zeolite pores. Nevertheless, such a hard water (as F.I.h) is seldom found at contaminated sites, indicating that the expected reduction in the activities is smaller at a field site compared to the experiments here. Prior to application of Trap-Ox Fe-BEA35 at a field site, the reactivity experiments with the on-site groundwater are recommended.

**Results (Long-term fate in column reactor).** Trap-Ox Fe-BEA35 was able to adsorb and degrade MTBE for 4 reuse cycles and a total of ca. 350 exchanged pore volumes. The retardation factor ( $R$ ) for MTBE (determined from the  $c/c_{0.5}$  in the MTBE breakthrough curve, Figure 38) decreased over the repeated reuse steps by a factor of 2.5 with a stronger decrease between the 1<sup>st</sup> and 2<sup>nd</sup> sorption cycle. During this initial period a loss of Trap-Ox Fe-BEA35 particles from the column occurred (due to the pH changes between the particle injection suspension with pH 5.5 and the MTBE solution in F.I.h with pH 8.5). The reduction in MTBE retardation factors in the subsequent 2<sup>nd</sup> to 4<sup>th</sup> adsorption steps (where particle loss should play a minor role) still continued but was less pronounced (by a factor of 1.6). This decrease is most likely caused by ageing processes of the particles in the slightly alkaline F.I.h medium and minor particle mobilisation when  $\text{H}_2\text{O}_2$  solution is injected (resulting in a slight pH drop to pH 7.8 and gas formation). The particle loss can be in future avoided by applying the particle suspension with identical pH as the model groundwater in subsequent adsorption/oxidation steps.

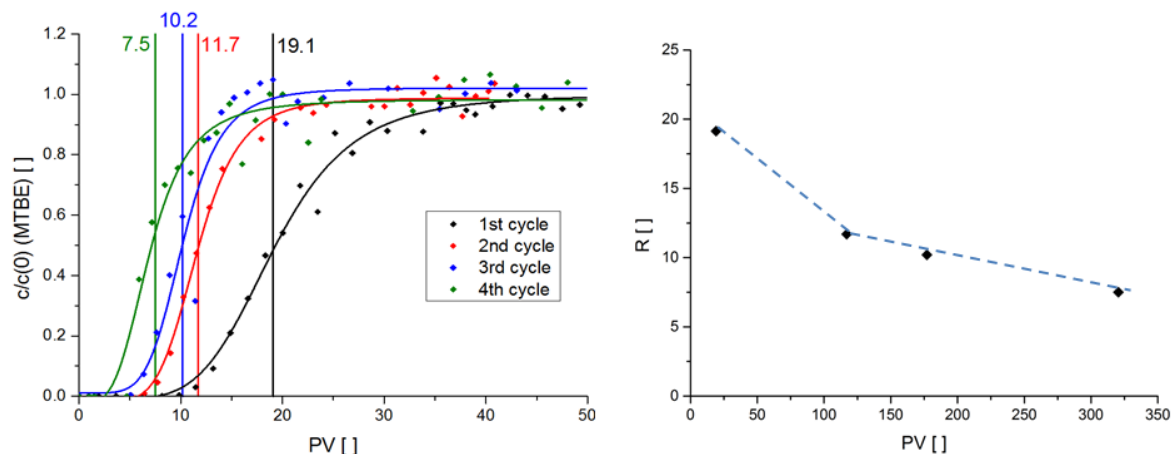


**Figure 38:** Breakthrough curves for MTBE over exchanged pore volume (PV) during individual adsorption cycles (left) and retardation factors for MTBE within the 4 adsorption cycles over total exchanged PV (right). Initial particle loading onto M.I: 1.1 wt%.  $c_{\text{MTBE}} = 10$  mg/L,  $v_{\text{eff}} = 1$  m/d (in adsorption steps),  $C_{\text{H}_2\text{O}_2} = 10$  g/L,  $v_{\text{eff}} = 1$  m/d).

**In conclusion**, Trap-Ox Fe-BEA35 is active as adsorbent and Fenton-like catalyst for contaminant oxidation with  $\text{H}_2\text{O}_2$  even in very hard groundwater with slightly alkaline conditions (pH 8.5) and significant NOM content. It can be anticipated that after the injection and deposition on the porous medium Trap-Ox Fe-BEA35 actively adsorb and catalytically oxidize MTBE by subsequent  $\text{H}_2\text{O}_2$  injections within a period of at least two months under these ‘worst case’ conditions (very hard water, high NOM content). During this period Trap-Ox Fe-BEA35 can trap (eliminate) dissolved contaminants and allows catalytic oxidation of adsorbed contaminants. Longer usage periods are likely as changes in zeolite properties after the initial equilibration with groundwater occur at a very low rate. The life-

time of Trap-Ox Fe zeolites at specific site conditions needs, nevertheless, to be evaluated in experiments with on-site groundwater.

#### 4.7 Bionanomagnetite (University of Manchester)

Responsible partner: UMAN

Contributors: UNIVIE, USTUTT

Bionanomagnetite is synthesized by Fe (III)-respiring subsurface bacteria e.g. *Geobacter sulfurreducens* and *Shewanella oneidensis* (Lovley, 1987), in the presence of an electron donor such as lactate, acetate or hydrogen and an insoluble Fe (III) electron acceptor. Bionanomagnetite particles are spherical, with the BET specific surface area of 17.1 m<sup>2</sup>/g (Watts et al., 2015), an average diameter in aqueous (F.I.s) suspension of 3.5 µm, with a portion of particles within the range of 10–50 nm (Byrne et al., 2011).

As bionanomagnetite in aqueous (F.I.s) suspension aggregate (hydrodynamic diameter increases from 8.7 µm to 100 µm after 1 week), optimization of bionanomagnetite was carried out in terms of increasing suspension stability and thus mobility in porous media (applying various stabilizers) and also functionalization with Pd in order to enhance particle reactivity (palladized bionanomagnetite) by reductive precipitation of Pd(0). Such synthesized heterocatalyst acts as continual source of electrons in presence of external electron donor such as H<sub>2</sub>/formate for applications in contaminant remediation (Coker et al., 2010).

##### 4.7.1 Stability of bionanomagnetite

*Stability of bionanomagnetite suspensions decreases in the following order of stabilizers: humic acid sodium salt (2 g/L) > starch > sodium humate (0.5 g/L) ≈ guar gum (3 g/L) > agar agar (2 g/L) > guar gum (2 g/L). On the basis of highly negative zeta potential, smallest particle size and good suspension stability, 0.5 g/L of Na humate is recommended as an optimal suspension stabilizer for bionanomagnetite.*

**Experimental protocol** Suspension of bionanomagnetite (Fe<sub>tot</sub> = 1 g/L in soft water F.I.s) was modified by addition of following stabilizers: agar agar (2 g/L), guar gum (3 g/L), starch (2 g/L) and humic acid sodium salt, hereafter Na humate (0.5 and 1 g/L). The suspensions were prepared in soft water F.I.s. Stability of particle suspension was determined by static sedimentation experiments carried out in a measuring cylinder; an aliquot of the particle suspension was sampled at a pre-defined height (1 cm below the water table) over a defined time period. Particle concentration in the aliquots was determined on the basis of Fe<sub>tot</sub>, determined spectrophotometrically by ferrozine assay. Hydrodynamic diameter of particles in suspension and zeta potential were determined by ZetaSizer Nano ZS (Malvern Instruments, UK), while the volume-based average particle size was determined by EyeTech™ (Ambivalue Ltd, the Netherlands).

**Results** Stability of the modified suspensions bionanomagnetite decreased in the following order of stabilizers: Na humate (1 g/L) > starch (2 g/L) > Na humate (0.5 g/L) ≈ guar gum (3 g/L) > agar agar (2 g/L) > guar gum (2 g/L) within the first 4 h (240 min, Figure 39).

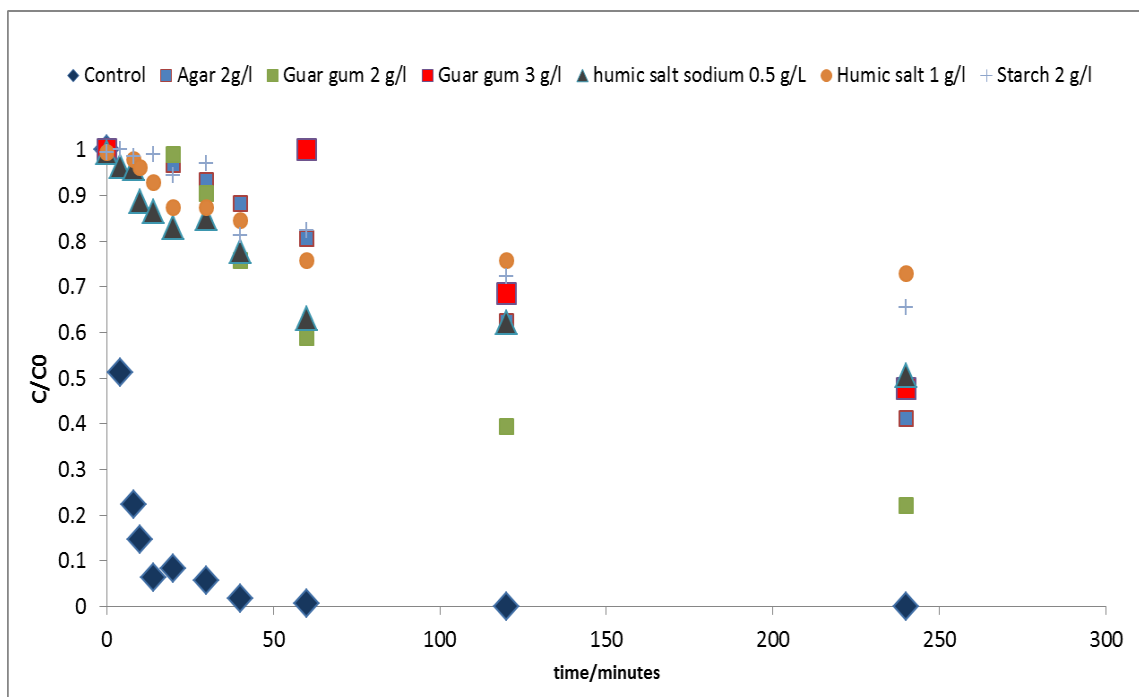


**Figure 39:** Normalized concentration of bionanomagnetite in the upper 1 cm of the modified suspension over time.  $c_0$  is the initial particle concentration.  $c$  is the particle concentration after a defined time. Control stands for pure aqueous Bnm. Agar stands for agar agar-modified suspension, humic salt (sodium) stands for Na-humate-stabilized suspensions.

Stabilization of bionanomagnetite suspensions transferred the zeta potential of particles from positive (in pure aqueous suspension) to negative, as needed for a better mobility of these particles in porous media (Table 19). The modifiers also altered the size distribution of the particles to various extent.



**Table 19:** Size distribution and zeta potential of bionanomagnetite in modified- and pure aqueous suspensions.

Bionanomagnetite in different suspensions	Average particle diameter [ $\mu\text{m}$ ]	$d_{10}$ [ $\mu\text{m}$ ]	$d_{50}$ [ $\mu\text{m}$ ]	$d_{90}$ [ $\mu\text{m}$ ]	Zeta potential [mV]
Bnm in aqueous (F.I.s) suspension	3.50	3.90	5.70	7.70	+13.0
Bnm in guar gum (3 g/L) suspension	13.13	5.96	12.30	21.49	-5.5
Bnm in agar agar (2 g/L) suspension	5.52	2.82	5.49	8.31	-13.5
Bnm in starch (2 g/L) suspension	23.49	7.84	22.43	41.25	-8.8
Bnm in Na humate (0.5 g/L) suspension	3.22	1.41	2.67	5.65	-35

**In conclusion**, on the basis of highly negative zeta potential, smallest particle size (Table 19) and fairly good suspension stability (Figure 39), 0.5 g/L of Na humate is recommended as an optimal suspension stabilizer for bionanomagnetite.

#### 4.7.2 Mobility and delivery of bionanomagnetite

*Na humate-stabilized suspensions of bionanomagnetite showed the highest mobility in D.I columns with estimated transport distance with 50% particle removal > 2 m.*

*Predicted transport distance with 50% particle removal ( $L_{T, 50}$ ) for guar gum-stabilized suspensions of bionanomagnetite ceased from of ca. 0.5 m in D.I column filled with homogenous porous medium to zero in D.II column filled with heterogeneous porous medium, emphasizing the importance of the selection of experimental conditions and scale for predicting the mobility of nanoparticles.*

**Experimental protocol** Mobility of stabilized bionanomagnetite suspensions ( $\text{Fe}_{\text{tot}} = 1 \text{ g/L}$ ) was firstly studied in D.I duplicate columns (2.8 cm i.d., 11.5 cm saturated packed bed length) filled with Dorsilit® PM (M.I). F.I.s served as a background electrolyte in all experiments. All the column tests were carried out under the injection conditions ( $v_{\text{eff}} = \text{ca. } 100 \text{ m/d}$ ). Furthermore, mobility of one selected stabilized suspension (with 3 g/L guar gum) was tested in D.II duplicate columns (7.8 cm i.d., 34 cm saturated packed bed length) filled with VEGAS PM (M.II) and with F.I.s as a background electrolyte. These tests were carried out both under groundwater flow condition ( $v_{\text{eff}} = 1 \text{ m/d}$ ) and the injection condition ( $v_{\text{eff}} = 100 \text{ m/d}$ ). Evaluation of the particle breakthrough was based on the  $\text{Fe}_{\text{tot}}$  content in the column effluents.

**Results** Modified suspensions of bionanomagnetite were significantly more mobile compared to the unmodified ones. Based on the particle breakthrough ( $c/c_0 > 0.9$ ), as anticipated from the suspension stability (see Section 4.7.1) Na humate-stabilized bionanomagnetite suspension appeared to be the most mobile in D.I columns under the conditions applied, followed by agar agar- and starch and guar gum-stabilized particle suspensions (Figure 40).

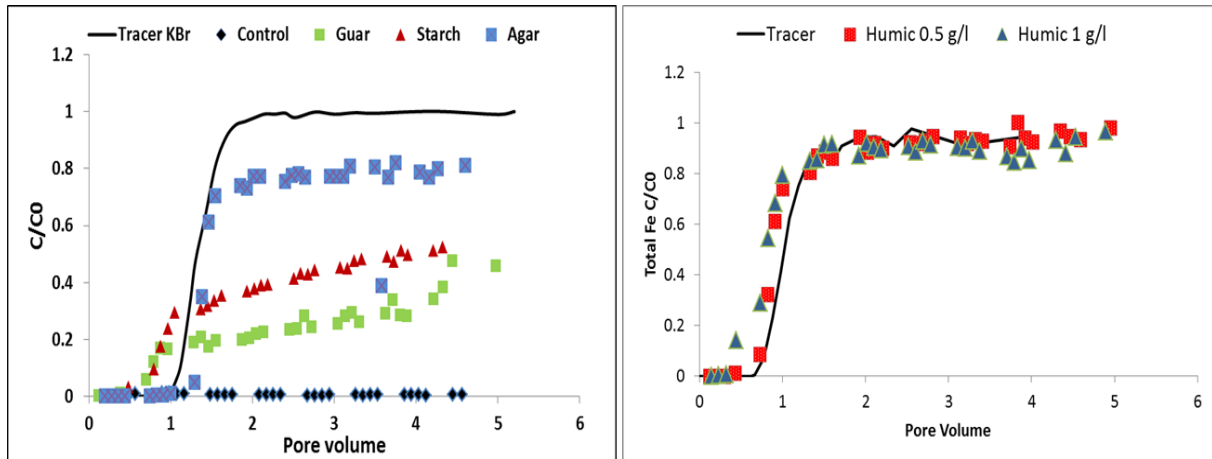


**Figure 40:** Mean breakthrough curves of stabilized bionanomagnetite suspensions with agar agar, guar gum and starch (left) and Na humate (right) in D.I columns. Injection velocity: 100 m/d;  $c_0, Fe_{tot} = 1$  g/L. Solid line is the breakthrough of KBr tracer. Control stands for Bnm in unmodified aqueous suspension. Note that guar stands for guar gum, agar stands for agar agar and humic stands for Na humate.

The estimated transport distances for 50% of particle removal were, as expected, largest for Na humate stabilized bionanomagnetite suspensions, reaching > 2 m, with the max transport distance (99.9% particle removal) being > 4 m, while independently on the differences in the particle breakthrough the predicted transport distances for other suspensions were lower and comparable (Table 20).

**Table 20:** Mobility parameters for bionanomagnetite particles in various stabilized suspensions.

NPs	C <sub>0</sub> (NP) [g/L]	PM	n <sub>e</sub> [%]	Fluid	V <sub>eff</sub> [m/ d]	k [1/s]	α [-]	L <sub>T</sub> (50%) [m]	L <sub>T</sub> (63%) [m]	L <sub>T</sub> (99.9%) [m]
Bionanomagnetite in guar gum (3 g/L)-modified suspension	1	M.I	0.38	F.I.s	100	7.0E-3	5.0E-3	0.47	0.52	1.09
Bionanomagnetite in starch (2 g/L)-modified suspension	1	M.I	0.38	F.I.s	100	6.0E-3	5.0E-3	0.50	0.55	1.71
Bionanomagnetite in agar agar (2 g/L)-modified suspension	1	M.I	0.35	F.I.s	100	2.2E-3	2.6E-2	0.47	0.52	1.15
Bionanomagnetite in Na humate (0.5 g/L)-modified suspension	1	M.I	0.38	F.I.s	100	1.6E-3	4.9E-2	2.13	2.35	4.13

Mobility of the guar gum-stabilized suspension of bionanomagnetite was further tested in D.II column filled with heterogeneous porous medium (M.II) under the injection conditions. The outcomes of the experiments showed that in this porous medium and at this experimental scale bionanomagnetite was not mobile. There was no particle breakthrough observed, since most of the bionanomagnetite particles accumulated at the column inlet, evident by the dark colour of the porous medium next to the injection port (Figure 41, left).

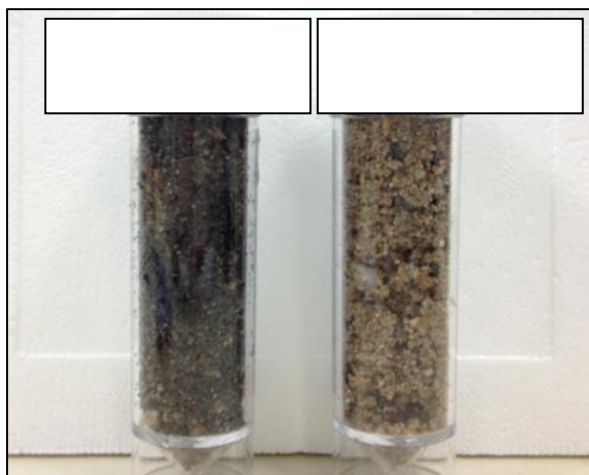


**Figure 41:** Sample of M.II collected from the column inlet (left) and column outlet (right), indicating bionanomagnetite accumulation (dark colour, left) around the column inlet and its absence at the column outlet (original colour of M.II, right).

**In conclusion**, as shown on the example of Na humate-stabilized bionanomagnetite, favourable parameters for particle stability i.e. highly negative zeta potential, small particle diameter and narrow particle size distribution are good indicators for high mobility potential of the particles. Mobility of bionanomagnetite particle is nevertheless strongly affected by the type of porous medium and the scale of the experiment; bionanomagnetite breakthrough in guar gum-stabilized suspension ceased from ca. 40% in D.I column filled with M.I to 0% in D.II column filled with M.II under the injection condition. This confirms that the upscaling of column experiments is necessary to better predict the particle mobility at the field.

#### 4.7.3 Fate of bionanomagnetite and palladized bionanomagnetite under field relevant conditions

*Suspension stabilizers lessen the reactivity of bionanomagnetite with respect to Cr(VI), but the reactivity can be recovered by particles functionalization with Pd. Palladized bionanomagnetite rapidly (both in stabilized and pure aqueous suspensions) is able to remove > 99% and > 90% of initial Cr(VI), respectively. Palladized bionanomagnetite is also able to completely dehalogenate PCE to ethane with  $k_{obs} = 0.265 \pm 0.014$  1/min (ca.  $4.4 \times 10^{-3}$  1/h).*

The following aspects of fate of Bionanomagnetite were studied:

- **Removal of Cr (VI)** for both stabilized particle suspensions of bionanomagnetite and palladized bionanomagnetite
- **Reactivity** of bionanomagnetite and palladized bionanomagnetite **with respect to PCE**

**Experimental protocol** Reactivity of bionanomagnetite in different suspensions was studied in batch reactors and the impact of suspension stabilizer was investigated. As for the stability studies, the bionanomagnetite suspensions were prepared in soft water (F.I.s), deoxidized by purging with N<sub>2</sub>, also used for preparation of a model 0.7 mM K<sub>2</sub>CrO<sub>4</sub> solution. The following suspension stabilizers were added: Na humate (0.5 g/L), guar gum (3 g/L) or starch (2 g/L). A control without stabilizer was also included. The final particle concentration in all reactors amounted to Fe<sub>tot</sub> of 1.5 g/L and the pH

was 6.9–7. The reactors were incubated on a roller shaker and aliquots were collected at defined time periods and were analysed for Cr(VI) spectrophotometrically by diphenylcarbazide (DPC) assay.

Removal of Cr(VI) was additionally studied by pristine- and palladized bionanomagnetite stabilized with starch or guar gum in batch reactors. Bionanomagnetite was firstly coated with Pd(0) and then stabilized with starch (2 g/L) or guar gum (3 g/L) in a buffer solution with pH 7 and  $Fe_{tot}$  of 0.5 g/L. Furthermore, 10 ml head space was replaced with  $H_2$ . 1 mM of Cr(VI) was finally added and the aliquots were analysed for Cr(VI) by the DPC assay over 360 min.

Both bionanomagnetite and palladized bionanomagnetite were used to study the potential for PCE removal. This was done in batch reactors filled with anaerobic synthetic water F.I.s (purged with  $N_2$ ) in a volumetric ratio of 1:1 for liquid and headspace (purged with  $H_2$ ) and pH 6.8 (during the reaction). PCE was added to a final concentration of 50 mg/L. Bionanomagnetite or palladized bionanomagnetite were then added to the reactor to a final  $Fe_{tot}$  concentration of 1 g/L and 0.025 g/L, respectively. The batch reactions were mixed and left to equilibrate and head space analysis was done for both, PCE and intermediates, by GC-FID.

**Results (Cr(VI) removal by bionanomagnetite in various suspensions)** The overall removal of Cr(VI) by bionanomagnetite in stabilized/modified suspensions decreased in the following order of stabilizers: no stabilizer > guar gum  $\approx$  Na humate > starch (Figure 42).

This loss of reactivity for bionanomagnetite in suspensions stabilized with starch and Na humate compared to the control (without stabilizer) is most likely due to the passivation of the surface reactive sites by these stabilizers, which was not observed for guar gum. The performance of guar gum-stabilized bionanomagnetite, was on the other hand, very similar to the control, removing ca. 85% of the initial Cr(VI) at the end of the experiment (Figure 42 B). Na humate-stabilized bionanomagnetite removed close to 75% of the initial Cr(VI), while starch-stabilized bionanomagnetite was able to remove only a half of the initial Cr(VI) (Figure 42 B).

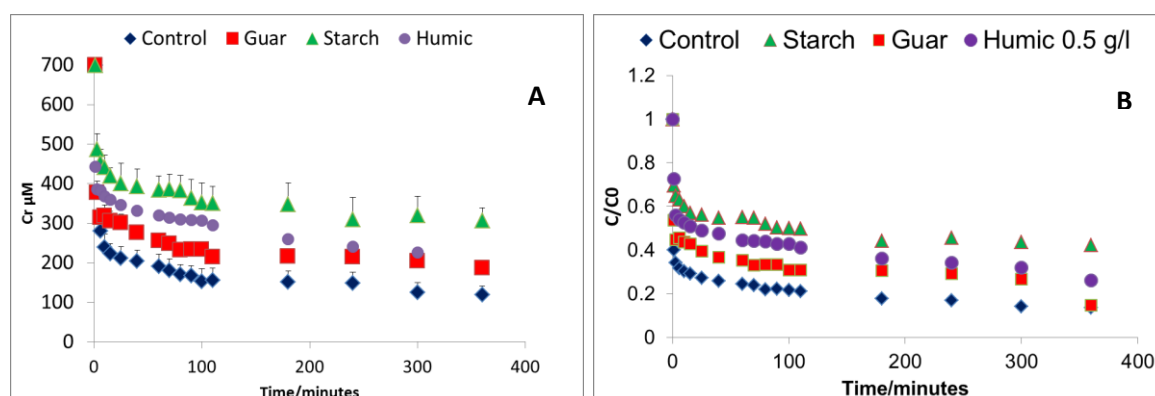


**Figure 42:** Reduction of Cr (VI) by bionanomagnetite in differently stabilized suspensions and in control (A). Changes in Cr (VI) concentrations normalized to initial  $Cr_{tot}$  in the course of the reaction (B). “Guar” stands for guar gum-, “starch” for starch- and “humic” for Na humate-stabilized suspensions. Control refers to the aqueous particle suspension without modifiers.

**In conclusion**, even though the Na humate-stabilized suspensions of bionanomagnetite showed the highest mobility potential, their Cr(VI) removal is somewhat lower compared to the bare- or guar

gum-stabilized particles. This points to the need to further optimization of stabilized bionanomagnetite towards complete removal of Cr(VI).

**Results (Cr(VI) removal by palladized bionanomagnetite)** Pristine palladized bionanomagnetite improved Cr(VI) removal to 99.2%, compared to that of pristine bionanomagnetite (ca. 85%, Figure 42B) after 240 min of reaction time, with Cr (VI) concentration dropping from 1000  $\mu\text{M}$  to 80  $\mu\text{M}$  (Figure 43). Independently of the stabilizer applied, palladized bionanomagnetite in stabilized suspensions was able to remove 90% of the initial Cr(VI), with Cr (VI) concentration dropping from 700  $\mu\text{M}$  to 70  $\mu\text{M}$  after 6 h of the reaction time (Figure 43).

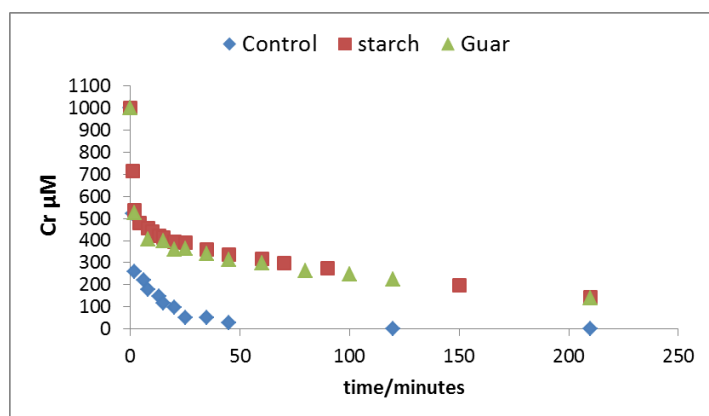


**Figure 43:** Cr(VI) removal by pristine palladized bionanomagnetite, i.e. control and palladized bionanomagnetite stabilized with guar gum (3 g/L) or starch (2 g/L); Initial  $\text{Fe}_{\text{tot}} = 0.5 \text{ g/L}$ .

**In conclusion**, the applied stabilizer somewhat decrease the reactivity of palladized bionanomagnetite, but the reactivity of stabilized palladized bionanomagnetite remains higher than that of pristine or stabilized bionanomagnetite. Therefore, palladized bionanomagnetite can be considered as better means of Cr(VI) removal from contaminated groundwater.

**Results (Removal of PCE by bionanomagnetite and palladized bionanomagnetite)** It was observed that unlike bionanomagnetite, 40 x less concentrated palladized bionanomagnetite was able to rapidly dechlorinate PCE with ethane formed as an end product (data not shown).

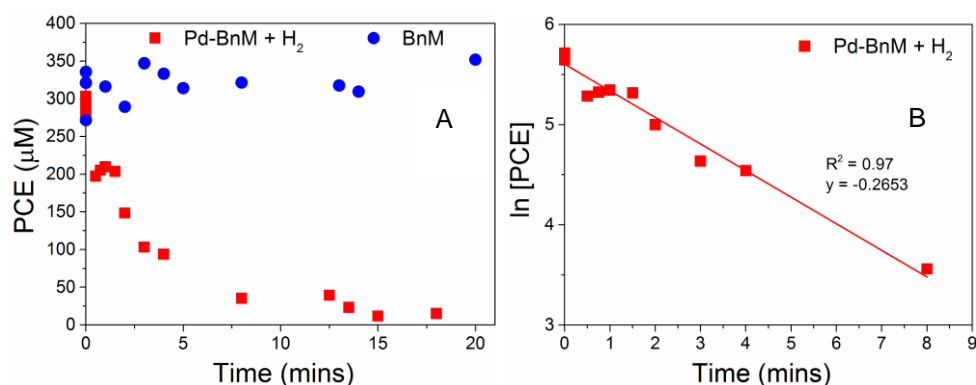


**Figure 44:** Decrease of PCE concentration in the synthetic groundwater treated with 1 g/L Fe bionanomagnetite (BnM, blue circles) and the 0.025 g/L palladized bionanomagnetite (Pd-BnM, red squares) the latter supplied with an excess of H<sub>2</sub>(A) and linear regression of ln[PCE] used to calculate dechlorination kinetics ( $k_{obs}$ ) (B).

Kinetic data for TCE dehalogenation by palladized bionanomagnetite are presented in Table 21 and obtained from the slope of ln- transformed PCE concentration decrease during the reaction time (Figure 44B) following the approach of Hildebrand et al. (2009).

**Table 21:** Summary of kinetic data for TCE dehalogenation by palladized bionanomagnetite.  $K_{obs}$  is pseudo first order reaction rate constant,  $K_{Pd}$  is reaction rate constant normalized to concentration of Pd, and  $A_{Pd}$  is specific catalyst activity.

Catalyst	Pd [g/L]	$K_{obs}$ [1/min]	$K_{Pd}$ [L/g <sub>Pd</sub> /min]	$A_{Pd}$ [L/g <sub>Pd</sub> /min]
Palladized bionanomagnetite	7.94E-4	$0.265 \pm 0.014$	$334 \pm 18$	$492 \pm 25$

**In conclusion**, unlike bionanomagnetite, palladized bionanomagnetite is able to efficiently and rapidly dehalogenate PCE in presence of H<sub>2</sub> as external electron donor with ethane as the final degradation product.



## 4.8 Nano-Goethite (University of Duisburg-Essen)

Responsible partner: UDE

Nano-Goethite particles serve as highly reactive electron acceptors for microbial reduction and consequently simulated microbial oxidation of pollutants, such as BTEX compounds. For example, the genus *Geobacter* is capable to use Fe(III) as electron acceptor for the degradation of toluene.

Optimization of Nano-Goethite was carried out in terms of increasing the stability and consequently mobility of particle suspensions and by adding humic acid solution into aqueous suspension of particles. The optimized suspension of Nano-Goethite contains 12 g/L TOC and 5–10 g/L Al (resulting from the particle production process).

### 4.8.1 Stability of Nano-Goethite

*Nano-Goethite particles are stable (for > 24 h) in optimized aqueous suspension, as a consequence of electrostatic repulsion between the particles.*

**Experimental protocol** Stability of Nano-Goethite particles was determined by static sedimentation experiments carried out in a measuring cylinder. An aliquot of the particle suspension (prepared in deionized water containing 0.12 g/L Ca<sup>2+</sup> and 100 mM Fe<sub>tot</sub>) was sampled at a pre-defined height (1 cm below the water table) in certain time intervals and the particle concentration was calculated based on Fe<sub>tot</sub> content (ferrozine assay). Hydrodynamic radius and zeta potential of Nano-Goethite particles was determined in a (1:10 deluted) suspension by ZetaSizer Nano ZS, Malvern, UK).

**Results** Hydrodynamic radius of Nano-Goethite particles in suspension was 240 ± 10 nm, and this value was independent on the procedure used for the suspension preparation (15 min homogenization in an ultrasonic bath or 15 min by Ultra-Turrax at 30,000 rpm). Zeta potential was -56 ± 2 mV, indicating the significance of electrostatic repulsions for particle stabilization. The results demonstrated long-term stability of Nano-Goethite particles (> 24 h), most likely due to their small size and electrostatic repulsion provided by humic acid coating.

### 4.8.2 Mobility and Delivery of Nano-Goethite

*Nano-Goethite is mobile in M.II porous medium, with  $L_{T,50}$  being 1.2-2.2 m, depending on the water hardness. Nano-Goethite can be delivered into porous medium from Spolchemie II, CZ field site to ca. 2.5 m from the injection point. Mobility of renegade particles is unlikely, since Nano-Goethite loses its stabilizing humic acid coating while moving through porous medium.*

**Experimental protocol** Mobility of Nano-Goethite suspension ( $c_{\text{particle}} = 1 \text{ g/L}$ ) was studied in D.I columns (3.6 cm i.d., 20 cm saturated packed bed length) filled with VEGAS PM (M.II). Background electrolytes of different hardness were applied (F.I.s, F.I.m and F.I.h). All the column tests were carried out under the injection conditions (injection velocity: of ca. 43 m/d). The evaluation of the particle breakthrough was done on the bases of Fe<sub>tot</sub> content in the column effluents determined by the ferrozine assay.

Delivery of Nano-Goethite into the BTEX-contaminated porous medium from Spolchemie II, CZ field site (where Nano-Goethite particles were injected) was studied in cascading column experiments. Five columns were used in the cascading column set. The Fe<sub>tot</sub> concentration of the feeding suspen-

sion was ca. 92 mM. Details on the columns, including the column length, porosity, flow rate and velocity are presented in in Table 22. The column effluents were analysed for  $Fe_{tot}$  used to estimate mobility of Nano-Goethite. Particle size and zeta potential of Nano-Goethite, as well as the DOC content were monitored in each column effluent.

**Table 22:** Experimental conditions for cascading column experiment with Nano-Goethite.

Column number	$L_{column}$ [m]	Q [mL/min]	$v_{eff}$ [m/h]	$n_e$
1	0.11	24.70	1.54	0.40
2	0.20	14.07	0.877	0.38
3	0.35	8.01	0.500	0.41
4	0.61	4.56	0.285	0.36
5	1.08	2.60	0.162	0.38

**Results (D.1 column experiments)** Independently of the hardness of the background electrolyte, the breakthrough of Nano-Goethite particle was high, ranging from 89 to 94% (data not shown). Estimated transport distances for 50% particle removal were 1–2 m, while max transport distances (for 99.9% of particle removal) amounted to ca. 13–20 m, depending on the background fluid (Table 23).

**Table 23:** Mobility parameters for optimized Nano-Goethite particles.

NPs	$C_0$ (NP) [g/L]	Porous media (PM)	$n_e$ [%]	Fluid	$V_{eff}$ [m/d]	k [1/s]	$\alpha$ [-]	$L_T$ (50%) [m]	$L_T$ (63%) [m]	$L_T$ (99.9%) [m]
Nano-Goethite	1	M.II	35	F.I.s	43	2E-3	2E-3	2.0	2.9	20.2
Nano-Goethite	1	M.II	33	F.I.m	43	3E-3	3E-3	1.2	1.9	12.9
Nano-Goethite	1	M.II	33	F.I.h	43	2E-3	2E-3	2.2	3.1	21.8

**Results (cascading column experiments)** On the basis of the  $Fe_{tot}$  concentrations in the initial column (1) and the subsequent cascading columns (2–5) it was apparent that Nano-Goethite was mobile in porous medium from Spolchemie II field site, CZ. Concentration of the injected Nano-Goethite was reduced by ca. 4.7 mM per meter of travel distance and reached 86% of the original injected suspension concentration after 2.5 m. The breakthrough of Nano-Goethite particles was modelled by the MNMs model (micro-and nanoparticle transport, filtration and clogging model suite developed by WP7) and presented in Table 23. The distance of 2.5 m was estimated by the MNMs model as a travel distance at which Nano-Goethite can be successfully delivered after the injection (Figure 45 and Table 24).

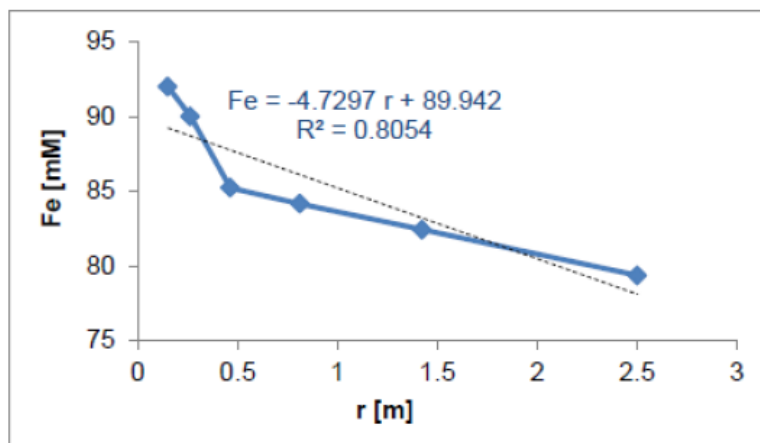


**Figure 45:** Mobility of Nano-Goethite (estimated from  $Fe_{tot}$  content) as a function of theoretical distance from the injection well ( $r$ ).

**Table 24:** Transport parameters for Nano-Goethite as delivered by the MNMs model.  $q_c$ : flow rate;  $r_c$ : theoretical distance from the injection well;  $n_{modelled}$ : modelled porosity;  $a_x$ : longitudinal dispersivity;  $k_a$ : attachment rate;  $k_d$ : detachment rate. Note that  $q_c$  and  $r_c$  are measured, while the remaining parameters are calculated.

Measured position in the system of cascading columns	$q_c$ [m/h]	$r_c$ [m]	Column number	$n_{modelled}$	$a_x$ [m]	$k_a$ [1/s]	$k_d$ [1/s]
Before column 1	2.122	0.150	1	0.49	0.0136	1.0E-04	1.0E-04
Between columns 1-2	1.209	0.263	2	0.44	0.0256	1.0E-04	1.0E-04
Between columns 2-3	0.688	0.462	3	0.45	0.0030	1.0E-04	1.0E-04
Between columns 3-4	0.392	0.812	4	0.34	0.0288	1.0E-04	1.0E-04
Between columns 4-5	0.223	1.425	5	0.40	0.0034	1.0E-04	1.0E-04
After column 5	0.127	2.502				1.0E-04	1.0E-04

Detailed inspection of the particle properties and DOC content in column effluents offered insights into the fate of optimized Nano-Goethite particles with the increasing transport distance.

As the theoretical transport distance increased, the particles in the column effluents became smaller, indicating that the larger aggregates had been filtered out by the porous medium. Nevertheless, in the last meter of the travel path the particle size in the column effluents was constant at ca. 450 nm (data not shown), indicating that this is a stable fraction of Nano-Goethite suspension. Also zeta potential of the particles along the transport path changed from ca. -50 mV to ca. -35mV, but was constant within the last meter. This result clearly indicated the loss of humic acid coating during transport mostly within the first meter of the theoretical travel distance from the injection point. This was confirmed by a decreasing trend of the DOC contents in the column effluents (data not shown), also within the first meter of the transport distance.

**In conclusion**, the results of the cascading column experiments had two implications for the application of Nano-Goethite at Spolchemie II field site, CZ. Firstly, the humic acid coating enabled the transport of Nano-Goethite of min 2.5 m from the injection and secondly, the mobility of renegade particles is highly unlikely, as Nano-Goethite lost its humic acid coating, and therefore its mobility potential, along the transport path.

#### 4.8.3 Fate of Nano-Goethite under field relevant conditions

*Nano-Goethite assist biodegradation of both benzoate and toluene, but higher Fe(II) reduction and contaminant degradation rate was found for benzoate. Slow Nano-Goethite-assisted benzoate reduction is observed in flow-through column reactor, with benzoate being degraded in the presence of electron acceptors other than Nano-Goethite.*

*Nano-Goethite does not change its elemental composition upon long-term (1 year) aging; the size and crystallinity of the particles does increase over time.*

The following aspects of fate of Nano-Goethite under field relevant conditions were studied:

- **Reactivity** of Nano-Goethite with respect to biodegradation of **toluene and benzoate** in the presence of porous medium from Spolchemie II field site, CZ (**batch reactor**)
- **Reactivity of Nano-Goethite in column reactor** with respect to **benzoate**
- Long-term changes in **Fe content and Fe speciation of Nano-Goethite** particles exposed for 1 year to BTEX-contaminated porous medium from Spolchemie II field site, CZ

#### **Experimental protocol**

Reactivity of Nano-Goethite with respect to biodegradation of toluene was studied in a set of batch reactors, containing the porous medium from Spolchemie II field site, CZ, Nano-Goethite particles in concentration of 10 mM (zeta potential -33.1 mV, particle size: 597.6 nm), and toluene in F.I.s fluid. Reactivity of Nano-Goethite with respect to biodegradation of benzoate was studied in a set of batch reactors, containing the porous medium from Spolchemie II field site, CZ, Nano-Goethite particles in concentration of 10 mM (zeta potential -60.7 mV, particle size: 350.3 nm), and toluene in F.I.s fluid. Detailed experimental conditions for each set of the batch reactors are presented in Table 25.

**Table 25:** Detailed experimental condition in batch reactors for studying toluene and benzoate biodegradation and corresponding Fe(III) reduction within Nano-Goethite.

Denotation of batch experiment	Sediment (PM)	Medium	Benzoate	Toluene	Fe(III) citrate	Nano-Goethite particles
PK_Batch 2	10 g	45 mL	2 mM	-	10 mM	-
NK	-	45 mL	2 mM	-	-	10 mM
K	-	45 mL	-	-	-	10 mM
P1	10 g	45 mL	-	-	-	10 mM
P2	10 g	45 mL	2 mM	-	-	10 mM
P3	10 g	45 mL	2 mM	20 mg/L	-	10 mM
PK_Batch 1	20 g	100 mL	-	20 mg/L	10 mM	-
NKN	20 g (sterile)	100 mL	-	-	-	10 mM
NKT	20 g (sterile)	100 mL	-	20 mg/L	-	10 mM
PN	20 g	100 mL	-	-	-	10 mM
PT	20 g	100 mL	-	20 mg/L	-	10 mM

In order to provide more field relevant information on Nano-Goethite reactivity, the experiment in a column reactors filled with porous medium from Spolchemie II field site, CZ, and artificial groundwater were carried out. The artificial groundwater was prepared with 0.292 g/L NaCl, 0.0075 g/L KCl, 0.2035 g/L MgCl<sub>2</sub>·6H<sub>2</sub>O, 1.029 g/L CaCl<sub>2</sub>·2H<sub>2</sub>O. Four stages of the experiment were defined: (i) column saturation with deionized water (flow rate 1 PV/d), (ii) column conditioning by artificial groundwater containing benzoate (flow rate 1 PV/d), (iii) alternating injection of Nano-Goethite ( $c_{\text{particle}} = 10 \text{ g/L}$ ,  $\text{Fe}_{\text{tot}} = 13.5 \text{ mM}$ ) and groundwater (flow rate 5 PV/d) and (iv) bioremediation (flow rate 0.3 PV/d). Note that due to the alternating injection of Nano-Goethite and artificial groundwater three biodegradation steps were allowed. In the first, second and third biodegradation step the respective benzoate concentrations in groundwater were 1 mM, 1 mM and 0.1 mM, respectively. The whole experiment lasted > 2 weeks.

The fifth column within the cascading column set described in Section 4.8.2 (1.75 cm i.d., 108 cm saturated packed bed length, filled with BTEX-contaminated porous medium from Spolchemie II, CZ) was sealed for 1 year. After which period the changes of  $\text{Fe}_{\text{tot}}$  and Fe speciation within Nano-Goethite particles were determined by measuring ferrous and ferric Fe content at different column depths, as well as the  $\text{Fe}_{\text{tot}}$  content of the column effluent (after column flushing with deionized water), determined by the ferrozine assay, upon flushing the column. Complementary, SEM-EDX, XRD were performed to get deeper insights into the changes of mineralogical composition and morphology of the particles.

**Results (Reactivity of Nano-Goethite with respect to bioremediation of toluene and benzoate, batch reactor)** 30.3% of Fe(III) was reduced in the batch reactors containing sediment and Nano-Goethite particles, while 42.7% of Fe(III) was reduced in the batch reactors containing sediment, Nano-Goethite particles and benzoate. This indicated that more Nano-Goethite was used in the presence of a contaminant. 35.7% of Fe(III) was reduced in the batch reactors containing sediment, Nano-Goethite particles, benzoate and toluene, indicating that there is less Nano-Goethite consumption in the presence of both contaminants (Figure 46). Positive controls (containing sediment, benzoate and Fe(III) citrate) showed a Fe(III) reduction of 65.4%, indicating that more Nano-Goethite is consumed when a contaminant co-exists with Fe(III) citrate as the electron acceptor.

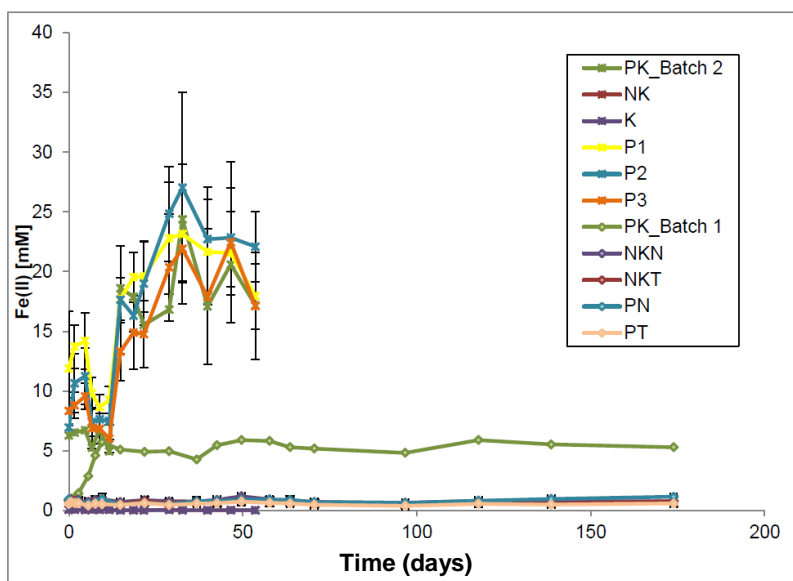


**Figure 46:** Fe(II) formation during the bioremediation of toluene and benzoate in sets of batch reactors. Detailed information on experimental sets denoted in the legend is given in Table 25.

The obtained reaction rate for Nano-Goethite-assisted biodegradation and correspondingly the Fe reduction rate are higher for benzoate than for toluene (Table 26).

**Table 26:** Degradation rates and Fe reduction rates during the Nano-Goethite-assisted biodegradation of toluene and benzoate.

	Bioremediation of toluene	Bioremediation of benzoate
Contaminant degradation rate	0.47 $\mu\text{M}/\text{d}$	1.86 $\mu\text{M}/\text{d}$
Fe reduction rate	0.004 mM/d	0.25 mM/d

**Results (Reactivity of Nano-Goethite with respect to bioremediation of benzoate, column reactor)**

Three bioremediation steps were recognized in benzoate degradation in column reactor in the presence of Nano-Goethite. In the first biodegradation both Fe(III) reduction/Fe(II) formation and degradation of benzoate were observed (Figure 47). Nevertheless, since degradation of benzoate was also observed in the controls without Nano-Goethite, there is an indication that other electron acceptors (such as  $\text{NO}_3^-$  and  $\text{SO}_4^{2-}$ ) were present in sediments.

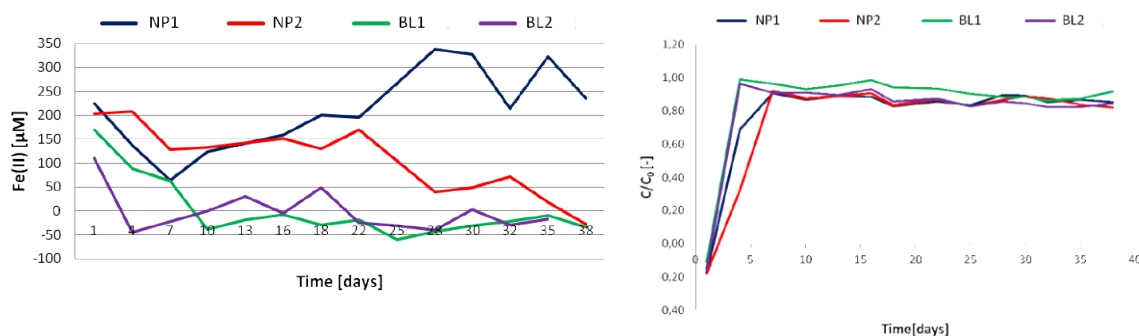


**Figure 47:** Increase of Fe(II) content (left) and degradation of benzoate (right) in the column reactor after the first bioremediation step. NP1 and NP2 refer to columns with Nano-Goethite, while BL1 and BL2 refer to blanks (without Nano-Goethite).

In the second bioremediation step, the formation of Fe(II) was evident in columns with Nano-Goethite. In the columns with Nano-Goethite concentration of benzoate continued to slowly decrease, indicating that biodegradation occurs (Figure 48), with a steeper decrease in concentration in the column reactors containing Nano-Goethite particles.

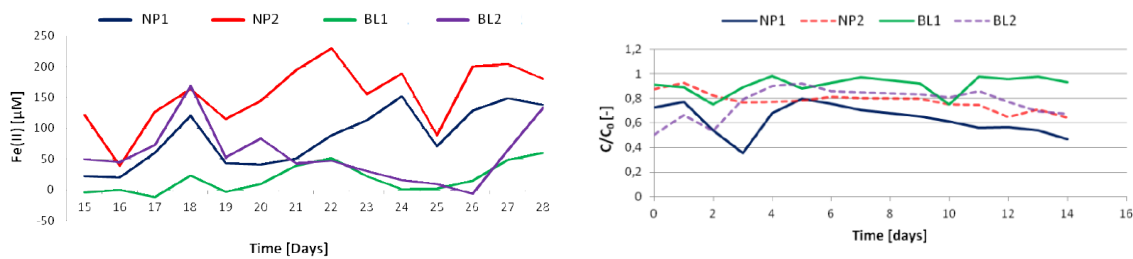


**Figure 48:** Increase of Fe(II) content (left) and slow degradation of benzoate (right) in the column reactor after the second bioremediation step. NP1 and NP2 refer to columns with Nano-Goethite, while BL1 and BL2 refer to blanks (without Nano-Goethite).

The third bioremediation step showed similar results as the second one (data not shown).

**In conclusion**, the results of the reactivity test in column reactors demonstrated the potential of Nano-Goethite to enhance the bioremediation of Nano-Goethite. Slower degradation of benzoate was also observed in the absence of Nano-Goethite particles, indicating the presence of other electron acceptors, such as  $\text{NO}_3^-$  and  $\text{SO}_4^{2-}$  in the sediments. No significant leaching of Nano-Goethite was observed under these experimental conditions (very slow flow rate of 0.3 PV/day during the bioremediation stage). Fe reduction was limited to 200–300  $\mu\text{M}$ , independently of the particle transport. This is probably due to the very slow flow and inability to provide a sufficient interaction between benzoate and Nano-Goethite within porous media.

**Results (Long-term changes in Fe content and Fe speciation of Nano-Goethite)**  $\text{Fe}_{\text{tot}}$  content decreased along the column length, from 30–45 mM in the upper and middle segments of the column, up to 14 mM at the column end, indicating heterogeneous distribution of Nano-Goethite particles within the porous medium from Spolchemie II, CZ field site, and the higher particle content closer to the column inlet. After the column was flushed with deionized water only ca. 8 mM  $\text{Fe}_{\text{tot}}$  were detected in the column effluent, indicating that the majority of Nano-Goethite was irreversibly loaded onto the porous medium. Most of the measured Fe was as Fe(III).



SEM images proved that Nano-Goethite aggregates in the column effluent (after the column was sealed for 360 days) are much larger with larger and more distinct nano-needles, compared to the particle size in the originally injected suspension, indicating higher crystallinity (Figure 49).

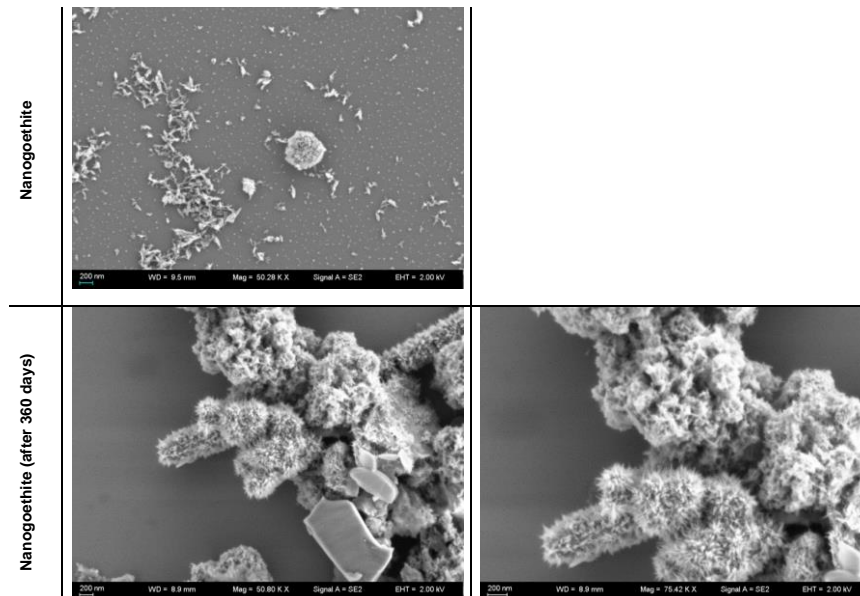


**Figure 49:** SEM images of fresh Nano-Goethite (upper image) and 360 days aged Nano-Goethite from the column effluent (lower image), also in higher magnification (lower image right).

EDX spectra showed that the aged Nano-Goethite particles had a similar composition (in terms of Fe, O, C, Cl and occasionally traces of S and P) as compared to the freshly produced ones (Figure 50).

XRD analysis showed a clear pattern for goethite in the freshly produced Nano-Goethite particles and in the particles recovered from the column segments, but the goethite pattern was not detected within the aged particles from the aged column effluent, nor was it detected in the original porous medium from Spolchemie II field site, CZ (data not shown). These findings confirm that all goethite recorded within the sediment column derives from the injection suspension and remain as goethite in the column. Goethite leached in the effluent of the aged column was associated with large amount of sulfate (data not shown).

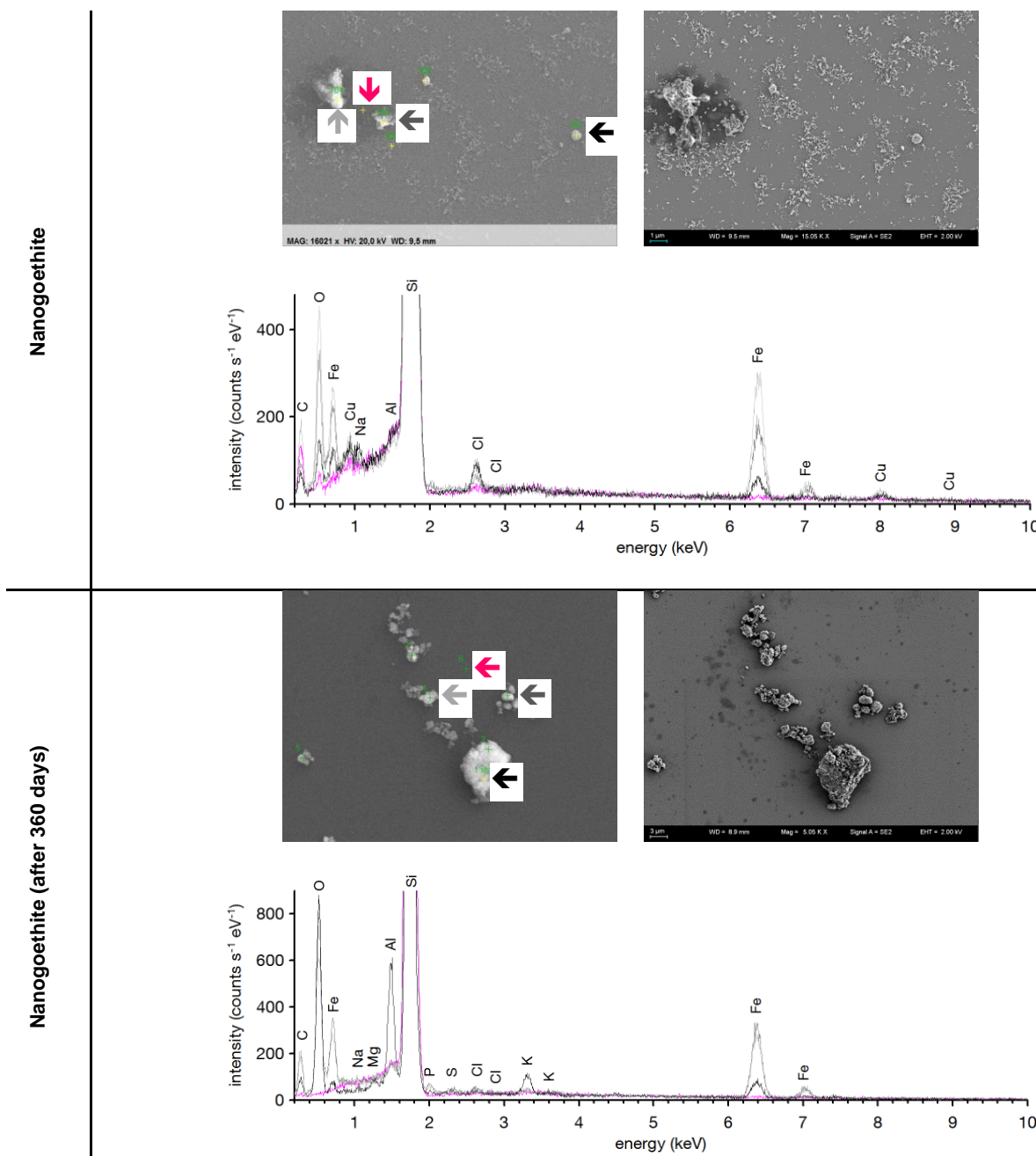


**Figure 50:** EDX spectra and SEM images (indicating the positions selected for EDX analysis) for fresh Nano-Goethite (upper images) and 360 days aged Nano-Goethite. SEM images at the left-hand side were recorded at 20 kV, while those at the right-hand side at 2 kV (providing better visualization of the topographic features). Black, dark grey and light grey arrows indicate the positions selected for the EDX analysis (associated EDX spectra with corresponding colour). Pink spectra depict blank measurements of the silicon wafer.

**In conclusion,** Fe-speciation showed that Nano-Goethite is resistant to chemical changes after a long (1 year) period. Also mineral composition of particles remains the same, but the size and the crystallinity of nano-needle increased over time.

## 4.9 Mg/Al particles (VEGAS, University of Stuttgart)

Responsible partner: USTUTT

Mg/Al particles ( $\text{Mg}^0 : \text{Al}^0 = 1 : 1$ ) have a particle size of ca. 100  $\mu\text{m}$  (producers data) and a BET specific surface area of 0.2  $\text{m}^2/\text{g}$  (reported by the producer Omikron GmbH, Germany).

Mg/Al particles were not aimed to be injected at a field site within NanoRem, since these particles are still in the laboratory research and development phase. Nevertheless, as for other NanoRem particles, the reactivity tests with Mg/Al particles were carried out under the conditions that resemble field relevant conditions.

### 4.9.1 Fate of Mg/Al particles under field relevant conditions

*Poor long-term reactivity of Mg/Al particles with respect to PCE was observed, making these particles not beneficial for field application.*

The following aspect of fate of Mg/Al particles under field relevant conditions was studied:

- Long-term reactivity of Mg/Al particles with respect to PCE in the presence of porous medium (column reactor)

**Experimental protocol** Long-term reactivity of Mg/Al particles with respect to PCE was studied for 60 days in a column reactor (3.6 cm i.d., 200 cm saturated packed bed length) filled with Dorsilit® (M.I), loaded with 1.25 g of Mg/Al particles. An aqueous PCE solution (in F.II,  $c_{\text{O}_2} = 0.7\text{--}1$  mg/L) was continuously injected into the column reactor at  $v_{\text{eff}} = \text{ca. } 0.5$  m/d. Stainless steel valves were installed at the column inflow and outflow for monitoring the concentration of PCE and the degradation products. Effluent samples were taken every pore volume and analysed for PCE and TCE (by HPLC) and for DCE, VC, ethene, ethane and ethyne (by headspace GC). Gaseous reaction products (such as  $\text{H}_2$  formed via anaerobic corrosion) were collected in a gas trap and analysed by GC.  $\text{Cl}^-$  was measured in the column effluent by potentiometric titration. pH was continuously recorded every hour (by Hermes Messtechnik, Germany measuring technique), while the temperature was kept to an average of 22 °C (monitored by a PT100 sensor).

**Results** Mg/Al particles showed a poor long term reactivity towards PCE; PCE degradation (in terms of  $\text{Cl}^-$  formation) was most pronounced within the first 2–3 weeks (14–25 days) of the experiment (Figure 51). After 60 days of the reaction, the amount of PCE transformed equivalent to produced amount of  $\text{Cl}^-$  amounted to 37%. Only traces of TCE (equivalent to  $\ll 1\%$  transformation of PCE to TCE) and DCE were found (but no VC). Ethene and ethane were detected as final degradation products. A pH value of ca. 9 was recorded throughout the reaction.

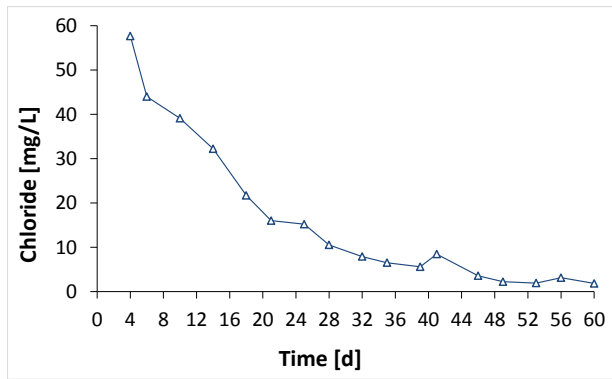


**Figure 51:** Cl<sup>-</sup> formation during the 60-days reaction of dissolved PCE with Mg/Al particles in a column reactor.

**In conclusion,** Mg/Al particles showed a poor long-term reactivity with respect to PCE, being with it not beneficial for field application.

## 5 List of References

- Adel Benchabane KB (2008) Rheological properties of carboxymethyl cellulose (CMC) solutions. *Colloid Polym. Sci.* 286(10), p. 1173-1180.
- Bi E, Bowen I, Devlin JF (2009) Effect of mixed anions ( $\text{HCO}_3^-$ – $\text{SO}_4^{2-}$ – $\text{ClO}_4^-$ ) on granular iron (Fe0) reactivity. *Environ. Sci. Technol.* 43 (15), p 5975-5981.
- Bleil S, Kopinke FD, Mackenzie K (2012) Carbo-Iron®—Synthesis and stabilization of Fe(0)-doped colloidal activated carbon for *in situ* groundwater treatment. *Chem. Eng. J.* 191, p. 588-595.
- Byrne JM, Telling ND, Coker VS, Patrick RAD, van der Laan G, Arenholz E, Tuna F, Lloyd JR (2011) Control of nanoparticle size, reactivity and magnetic properties during the bioproduction of magnetite by *Geobacter sulfurreducens*. *Nanotechnol.* 22(45):455709, p. 1-9.
- Coker VS, Bennett JA, Telling ND, Henkel T, Charnock JM, van der Laan G, Patrick RAD, Pearce CI, Cutting RS, Shannon IJ, Wood J, Arenholz E, Lyon IC, Lloyd JR (2010) Microbial Engineering of Nanoheterostructures: Biological Synthesis of a Magnetically Recoverable Palladium Nanocatalyst. *ACS Nano* 4, p. 2577-2584.
- Comba S and Braun J (2012) A new physical model based on cascading column experiments to reproduce the radial flow and transport of micro-iron particles. *J. Contam. Hidro.* 140-141, p. 1-11.
- Folk RL and Ward W (1957) Brazos River bar: a study in significance of grain-size parameters. *J. Sediment. Petrol.* 27, p. 3-26.
- Georgi A, Gillies G, Mackenzie K, Kopinke FD (2015) Colloidal Fe-zeolites - A novel material for sorption-supported in-situ chemical oxidation (ISCO), *Extended Abstract, Proceedings of AquaConSoil 2015, 9–12 June, Copenhagen*, <http://www.aquaconsoil.org/proceedings.html>.
- Gillies G, Mackenzie K, Kopinke FD, Georgi A (2016) Fluorescence labelling as tool for zeolite particle tracking in nanoremediation approaches. *Sci. Tot. Environ.* 550, p. 820-826.
- Gonzalez-Olmos R, Kopinke FD, Mackenzie K, Georgi A (2013) Hydrophobic Fe-zeolites for removal of MTBE from water by combination of adsorption and oxidation. *Environ. Sci. Technol.* 47, p. 2353-2360.
- Henn K (2005) Presentation on U.S. EPA Workshop on Nanotechnology for Site Remediation, Oktober, 2005. ([http://www.frtr.gov/nano/pdf/day1/henn\\_keith.pdf](http://www.frtr.gov/nano/pdf/day1/henn_keith.pdf)).
- Hildebrand H, Mackenzie K, Kopinke FD (2009) Highly active Pd-on-magnetite nanocatalysts for aqueous phase hydrodechlorination reactions. *Environ. Sci. Technol.* 43 (9), p. 3254-3259.
- Hua LB, Banucu R, Buchau A, Klaas N, Rucker WM (2015) Optimization of a Concentration Measurement Sensor for Nano Sized Zero Valent Iron Using Numerical Simulation. *IET Sci. Meas. Technol.* 9(5), p. 636-643.
- Jang MH, Lim M and Hwang YS (2014) Potential environmental implications of nanoscale zero-valent iron particles for environmental remediation. *Environ Health Toxicol.* 29, p.1-9.
- Johnson TL, Scherer M M, Tratnyek PG (1996) Kinetics of halogenated organic compound degradation by iron metal. *Environ. Sci. Technol.* 30. p. 2634-2640.
- Köber R, Hollert H, Hornbruch G, Jekel M, Kamptner A, Klaas N, Braun J (2014) Nanoscale zero-valent iron flakes for groundwater treatment. *Environ. Earth Sci.* 72 (9), p. 3339-3352.
- Laumann S, Micić V, Lowry GV, Hofmann T (2013) Carbonate minerals in porous media decrease mobility of polyacrylic acid modified zero-valent iron nanoparticles used for groundwater remediation. *Environ. Pollut.* 179 (0), p. 53-60.
- Li H, Banucu R, Buchau A, Klass N, Rucker WM (2015) Optimisation of a concentration measurement sensor for nano sized zero valent iron using numerical simulation. *IET Sci Meas Technol.* 9(5), p. 636-643.
- Liu Y, Majetich SA, Tilton RD, Sholl DS, Lowry GV (2005) TCE dechlorination rates, pathways, and efficiency of nanoscale iron particles with different properties. *Environ. Sci. Technol.* 39, p. 1338-1345.
- Liu Y, Lowry GV (2006) Effect of particle age (Fe0 content) and solution pH on NZVI reactivity: H<sub>2</sub> evolution and TCE dechlorination. *Environ. Sci. Technol.* 40, p. 6085-6090.
- Lovley DR, Stolz JF, Nord, GL, Phillips EJP (1987) Anaerobic Production of Magnetite by a Dissimilatory Iron-Reducing Microorganism. *Nature* 330, p. 252-254.
- Mackenzie K, Bleil S, Georgi A, Kopinke FD (2012) Carbo-Iron – An Fe/AC composite – As alternative to nano-iron for groundwater treatment. *Water Res.* 46, p. 3817-3826.
- Menadier Stavelot M (2015) Source zone remediation of tetrachloroethene using composite materials: Reactivity test in columns. Stuttgart, University of Stuttgart. PhD Thesis.

- Micić V, Kruge MA, Hofmann T (2013) Variations of common riverine contaminants in reservoir sediments. *Sci. Total Environ.* 458–460, p. 90-100.
- Oughton DH, Hertel-Aas T, Pellicer E, Mendoza E, Joner EJ (2008) Neutron activation of engineered nanoparticles as a tool for tracing their environmental fate and uptake in organisms. *Environ. Toxicol. Chem.* 27(9), pp. 1883-1887.
- Schmid D, Micić V, Laumann S, Hofmann T (2015) Measuring the reactivity of commercially available zero-valent iron nanoparticles used for environmental remediation with iopromide. *J. Contam. Hydrol.* 181, p.35-45.
- US EPA (2002) Methods for measuring the acute toxicity of effluents and receiving waters to freshwater and marine organisms. Fifth edition. EPA-821-R-02-012. U.S. Environmental Protection Agency, Office of Water (4303T) 1200 Pennsylvania Avenue, NW Washington DC, U.S.A.
- Velimirovic M, Carniato L, Simons Q, Schoups G, Seuntjens P, Bastiaens L (2014) Corrosion rate estimations of microscale zerovalent iron particles via direct hydrogen production measurements. *J. Hazard. Mater.* 270 (0), p. 18-26.
- Velimirovic M, Schmid D, Wagner S, Micić V, von der Kammer F, Hofmann T (2015) Agar agar-stabilized milled zerovalent iron particles for *in situ* groundwater remediation, *STOTEN* 563–564, p. 713-723.
- Viota JL, de Vicente J, Durán JDG, Delgado AV (2005) Stabilization of Magnetorheological Suspensions by Polyacrylic Acid Polymers. *J. Colloid. Interface Sci.* 284: p. 527-541.
- Watts MP, Coker VS, Parry SA, Patrick RAD, Thomas RAP, Kalin R, Llyod JR (2015) Biogenic nano-magnetite and nano-zero valent iron treatment of alkaline Cr(VI) leachate and chromite ore processing residue. *Appl. Geochem.* 54, p. 27-42.

## 6 Appendix

**Table A 1:** Experimental setup for cascading column experiments with CMC-modified NANOFR 25S particles. r: radius of the column; L: length of the column; A: cross section area of the column;  $V_b$ : bulk volume of the column;  $\delta_b$ : bulk density of porous medium; n: porosity; K: hydraulic conductivity, Q: injection rate; v: seepage velocity; q: Darcy velocity;  $c_{particle}$ : particle concentration;  $c_{CMC}$ : CMC concentration;  $\Delta t$ : duration of the injection;  $\Delta V$ : injected volume;  $PV_{inj}$ : number of injected pore volumes;  $\Delta m$ : particle load onto the column;  $\Delta x$ : particle traveled distance;  $\Delta p$ : max pressure difference between column inflow and outflow.

Set No/ Column No	Porous media	r	L	A	$V_b$	$\delta_b$	n	K	Q	v	v	q	$c_{particle}$	$c_{CMC}$	$\Delta t$	$\Delta V$	$PV_{inj}$	$\Delta m$	$\Delta x$	$\Delta p$
		[m]	[m]	[m <sup>2</sup> ]	[m <sup>2</sup> ]	[kg/m <sup>3</sup> ]	[-]	[m/s]	[m <sup>3</sup> /h]	[m/h]	[m/d]	[m/h]	[g/L]	[g/L]	[h]	[L]	[-]	[g]	[m]	[bar]
1 C1	M.II	4.40E-02	0.25	1.52E-03	3.80E-04	1832	0.26	1.94E-04	0.47	1.43	34.30	0.43	10	0	2	1.3	11.4	11.32	0.17	0.072
2 C1	M.II	4.40E-02	0.25	1.52E-03	3.80E-04	1901	0.31	1.70E-04	0.47	1.43	34.30	0.43	1	0	2	1.3	11.4	1.27	0.07	0.129
3 C1	M.II	4.40E-02	0.25	1.52E-03	3.80E-04	1891	0.26	1.82E-04	0.47	1.43	34.30	0.43	0.5	0	2	1.3	11.4	0.57	0.04	n.m.
4 C1	M.II	4.40E-02	0.25	1.52E-03	3.80E-04	1893	0.28	1.10E-04	0.47	1.43	34.30	0.43	10	4	2	1.3	11.4	10.86	0.24	0.034
5 C1	M.II	4.40E-02	0.25	1.52E-03	3.80E-04	1922	0.27	1.10E-04	0.47	1.43	34.30	0.43	5	4	2	1.3	11.4	7.22	0.15	0.020
6 C1	M.II	4.40E-02	0.25	1.52E-03	3.80E-04	1886	0.25	8.80E-05	0.52	1.58	37.80	0.47	10	4	2	1.3	12.6	11.25	0.25	0.024
7 C1	M.II	4.40E-02	0.252	1.52E-03	3.83E-04	1845	0.3	7.41E-05	1.00	3.03	72.77	0.91	10	4	1.04	1.43	12.6	9.92	0.25	0.137
7 C2	M.II	4.40E-02	0.25	1.52E-03	3.80E-04	1838	0.37	8.58E-05		1.25	29.95	0.37			0.95	0.54	4.8	1.81	0.125	0.030
8 C1	M.II	4.40E-02	0.245	1.52E-03	3.73E-04	1860	0.29	8.78E-05	1.00	3.03	72.77	0.91	5	4	2.07	2.87	25.2	15.84	0.25	0.202
8 C2	M.II	4.40E-02	0.247	1.52E-03	3.76E-04	1873	0.33	1.05E-04		1.25	29.95	0.37			1.91	1.09	9.5	0.22	0.1	0.017
9 C1	M.II	4.40E-02	0.245	1.52E-03	3.73E-04	1998	0.31	1.52E-05	1.00	3.03	72.77	0.91	10	6	1.04	1.43	12.6	8.67	0.25	0.297
9 C2	M.II	4.40E-02	0.251	1.52E-03	3.82E-04	1878	0.31	1.11E-05		1.25	29.95	0.37			0.95	0.54	4.8	2.4	0.24	0.079



Set No/ Column No	Porous media	r [m]	L [m]	A [m <sup>2</sup> ]	V <sub>b</sub> [m <sup>2</sup> ]	δ <sub>b</sub> [kg/m <sup>3</sup> ]	n [-]	K [m/s]	Q [m <sup>3</sup> /h]	v [m/h]	v [m/d]	q [m/h]	C <sub>particle</sub> [g/L]	C <sub>CMC</sub> [g/L]	Δt [h]	ΔV [L]	PV <sub>inj</sub> [-]	Δm [g]	Δx [m]	Δp [bar]
10 C1	M.II	4.40E-02	0.25	1.52E-03	3.80E-04	1689	0.35	1.73E-04	1.00	3.03	72.77	0.91	10	8	1.04	1.43	12.6	10.56	0.25	1.125
10 C2	M.II	4.40E-02	0.253	1.52E-03	3.85E-04	1868	0.32	1.60E-04	1.00	1.25	29.95	0.37			0.95	0.54	4.8	2.2	0.25	0.005
11 C1	M.II	4.40E-02	0.25	1.52E-03	3.80E-04	1954	0.28	1.10E-04	1.00	3.03	72.77	0.91	10	10	1.04	1.43	12.6	7.13	0.25	0.805
11 C2	M.II	4.40E-02	0.25	1.52E-03	3.80E-04	1885	0.2	1.24E-04		1.25	29.95	0.37			0.95	0.54	4.8	n.m.	0.25	0.130
11 C3	M.II	4.40E-02	0.5	1.52E-03	7.60E-04	1867	0.32	1.70E-04		0.66	15.91	0.20			0.75	0.23	1	n.m.	0.08	0.370
12 C1	M.II	4.40E-02	0.25	1.52E-03	3.80E-04	1868	0.28	1.55E-05	1.00	3.03	72.77	0.91	10	12	1.04	1.43	12.6	8.85	0.25	0.032
12 C2	M.II	4.40E-02	0.25	1.52E-03	3.80E-04	1832	0.34	1.50E-04		1.25	29.95	0.37			0.95	0.54	4.8	0.96	0.25	0.149
12 C3	M.II	4.40E-02	0.5	1.52E-03	7.60E-04	1856	0.27	1.18E-04		0.66	15.91	0.20			0.75	0.23	1	0.41	0.06	0.031
13 C1	M.II	4.40E-02	0.246	1.52E-03	3.74E-04	1898	0.31	1.22E-04	1.00	3.03	72.77	0.91	10	12	1.04	1.43	12.6	7.44	0.25	0.851
13 C2	M.II	4.40E-02	0.248	1.52E-03	3.77E-04	1877	0.3	1.37E-04		1.25	29.95	0.37			0.95	0.54	4.8	1.84	0.25	0.231
13 C3	M.II	4.40E-02	0.497	1.52E-03	7.56E-04	1856	0.29	1.39E-04		0.66	15.91	0.20			0.75	0.23	1	0.03	0.07	0.165
14 C1	M.II	4.40E-02	0.245	1.52E-03	3.73E-04	1882	0.31	1.12E-04	1.00	3.03	72.77	0.91	10	10	1.04	1.43	12.6	n.m.	0.25	0.586
14 C2	M.II	4.40E-02	0.252	1.52E-03	3.83E-04	1877	0.29	1.14E-04		1.25	29.95	0.37			0.95	0.54	4.8	n.m.	0.25	0.230
15 C1	M.II	4.40E-02	0.25	1.52E-03	3.80E-04	1868	0.35	1.16E-04	1.00	3.03	72.77	0.91	10	10	1.04	1.43	12.6	5.51	0.25	0.712
15 C2	M.II	4.40E-02	0.25	1.52E-03	3.80E-04	1894	0.26	9.06E-05		1.25	29.95	0.37			0.95	0.54	4.8	0.78	0.25	0.180
15 C3	M.II	4.40E-02	0.5	1.52E-03	7.60E-04	1837	0.28	9.03E-05		0.66	15.91	0.20			0.75	0.23	1	0.04	0.04	0.020

**Table A 2:** Experimental setup for cascading column experiments with CMC-modified NANO FER STAR particles. r: radius of the column; L: length of the column; A: cross section area of the column;  $V_b$ : bulk volume of the column;  $\delta_b$ : bulk density of porous medium; n: porosity; K: hydraulic conductivity, Q: injection rate; v: seepage velocity; q: Darcy velocity;  $c_{particle}$ : particle concentration;  $c_{CMC}$ : CMC concentration;  $\Delta t$ : duration of the injection;  $\Delta V$ : injected volume;  $PV_{inj}$ : number of injected pore volumes;  $\Delta m$ : particle load onto the column;  $\Delta x$ : particle traveled distance;  $\Delta p$ : max pressure difference between column inflow and outflow.

Set No/ Column No	Porous media	r	L	A	$V_b$	$\delta_b$	n	K	Q	v	v	q	$c_{particle}$	$c_{CMC}$	$\Delta t$	$\Delta V$	$PV_{inj}$	$\Delta m$	$\Delta x$
		[m]	[m]	[m <sup>2</sup> ]	[m <sup>3</sup> ]	[kg/m <sup>3</sup> ]	[-]	[m/s]	[m <sup>3</sup> /h]	[m/h]	[m/d]	[m/h]	[g/L]	[g/L]	[h]	[L]	[-]	[g]	[m]
1 C1	M.II	4.40E-02	0.25	1.52E-03	3.80E-04	1896	0.33	6.90E-05	0.75	2.27	54.58	0.68	10	5	1.22	1.26	10.15	8.58	0.25
1 C2	M.II	4.40E-02	0.25	1.52E-03	3.80E-04	1898	0.33	1.29E-04		0.94	22.46	0.28			1.03	0.44	3.54	1.01	0.10
2 C1	M.II	4.40E-02	0.25	1.52E-03	3.80E-04	1861	0.35	1.49E-04	0.75	2.27	54.58	0.68	10	8	1.22	1.26	10.15	3.44	0.25
2 C2	M.II	4.40E-02	0.25	1.52E-03	3.80E-04	1879	0.35	1.39E-04		0.94	22.46	0.28			1.03	0.44	3.82	0.70	0.25
3 C1	M.II	4.40E-02	0.25	1.52E-03	3.80E-04	1900	0.38	1.89E-04	1.00	3.03	72.77	0.91	10	10	0.93	1.29	8.90	8.05	0.25
3 C2	M.II	4.40E-02	0.25	1.52E-03	3.80E-04	1875	0.39	1.64E-04		1.25	29.95	0.37			0.88	0.50	3.40	0.36	0.20
7 C1	M.II	4.40E-02	0.25	1.52E-03	3.80E-04	1791	0.38	2.19E-04	1.54	3.68	88.32	1.40	5	0	1.12	2.38	15.81	n.m.	n.m.
8 C1	M.II	4.40E-02	0.25	1.52E-03	3.80E-04	1791	0.38	2.19E-04	0.50	38.58	925.92	11.57	5	0	0.11	1.97	19.91	7.87	0.25
8 C2	M.II	4.40E-02	0.25	1.52E-03	3.80E-04	1885	0.35	1.28E-04		6.84	164.16	2.05			0.11	0.33	2.36	0.55	0.05
9 C1	M.II	4.40E-02	0.25	1.52E-03	3.80E-04	1876	0.41	1.61E-04	1.00	3.03	72.77	0.91	10	10	0.98	1.36	11.47	11.36	0.25
9 C2	M.II	4.40E-02	0.25	1.52E-03	3.80E-04	1911	0.33	1.03E-04		1.25	29.95	0.37			0.95	0.54	3.89	2.04	0.25
10 C1	M.II	4.40E-02	0.25	1.52E-03	3.80E-04	1891	0.40	1.39E-04	1.38	4.17	100.03	1.25	10	8	0.75	1.43	9.26	7.56	0.25
10 C2	M.II	4.40E-02	0.25	1.52E-03	3.80E-04	1854	0.37	1.03E-04		1.72	41.18	0.52			0.68	0.54	3.79	1.03	0.20

Set No/ Column No	Porous media	r	L	A	V <sub>b</sub>	δ <sub>b</sub>	n	K	Q	v	v	q	C <sub>particle</sub>	C <sub>CMC</sub>	Δt	ΔV	PV <sub>inj</sub>	Δm	Δx
		[m]	[m]	[m <sup>2</sup> ]	[m <sup>3</sup> ]	[kg/m <sup>3</sup> ]	[-]	[m/s]	[m <sup>3</sup> /h]	[m/h]	[m/d]	[m/h]	[g/L]	[g/L]	[h]	[L]	[-]	[g]	[m]
11 C1	M.II	4.40E-02	0.25	1.52E-03	3.80E-04	1902	0.34	8.52E-05	1.00	3.03	72.77	0.91	10	10	1.03	4.13	10.50	8.75	0.25
11 C2	M.II	4.40E-02	0.25	1.52E-03	3.80E-04	1854	0.36	1.49E-04		1.25	29.95	0.37			0.95	0.54	3.44	n.m.	0.25
11 C3	M.II	4.40E-02	0.50	1.52E-03	7.60E-04	1860	0.37	1.87E-04		0.633	15.192	0.199			0.75	0.23	0.89	1.2	0.04